CLASSICAL AND QUANTUM CHAOS IN THE WEDGE BILLIARD

By

TOMAS SZEREDI, MSc.

A Thesis

Submitted to the School of Graduate Studies

in Partial Fulfillment of the Requirements for the Degree

Doctor of Philosophy, Physics

McMaster University

CLASSICAL AND QUANTUM CHAOS IN THE WEDGE BILLIARD

Doctor of Philosophy, Physics (1992)

Department of Physics and Astronomy

McMaster University

Hamilton, Ontario

TITLE: Classical and Quantum Chaos in the Wedge Billiard.

AUTHOR: Tomas Szeredi MSc. (McMaster University)

SUPERVISOR: Professor David A. Goodings

NUMBER OF PAGES: viii, 185

Abstract

We examine the relationship between the classical mechanics and the quantum eigenvalues of the wedge billiard. Special emphasis is placed on applications of the periodic orbit theory developed by Gutzwiller (1971) and recently modified by others. Evidence is presented suggesting that words formed from a two letter alphabet, consisting of T and V, uniquely label all periodic orbits. The periodic orbits are found (for several different wedge angles) using a two–dimensional Newton method and their actions, periods, stability exponents, and Maslov indices calculated. It is found that the periodic orbits are heavily pruned at all wedge angles. Families of non–isolated periodic orbits and their implications for the Gutzwiller trace formula are discussed. The scaling properties of the classical periodic orbits are also examined. A large matrix diagonalization was used to accurately calculate the first 200 and 300 quantum eigenvalues for the 60° and 49° wedges respectively. A theory is developed which allows one to use the quantum eigenvalues to obtain information about the classical periodic orbits. This theory is tested on the 49° and 60° wedges and shows that the quantum eigenvalues 'know' about the classical periodic orbits. Several quantization schemes derived from the Gutzwiller periodic orbit theory are presented and then tested for the 49° and 60° wedges. Eigenvalues computed using the classical periodic orbits as input are compared to the 'exact' eigenvalues from the matrix diagonaliza-

tion. A functional relation which uses the dynamical zeta function expressed as a product gives the best results.

Acknowledgements

This work was supported by the Department of Physics and Astronomy at McMaster University and the Natural Sciences and Engineering Research Council of Canada. Thanks and appreciation are extended to D.A. Goodings and J. Lefebvre for their many helpful comments and suggestions, support and enjoyable discussions.

Contents

Chapter 1

Introduction

Many physicists (including myself) have much of their intuition based in classical concepts. Well defined positions and well defined trajectories are ideas which are used everyday. Classical mechanics (Goldstein 1980, Rasband 1991, Marion 1970, Pars 1965) is the elaborate physical theory which has been constructed to formalize this classical intuition and allow predictions based on these ideas. Classically integrable systems, such as the harmonic oscillator and central force problem, are shown to exhibit a beautiful universal simplicity when expressed in the language of action–angle variables. With the advent of classical chaos (Henon and Heiles 1964, Lorenz 1963) classical mechanics is going through somewhat of a renaissance and its full richness is still being explored. Self similar structures and incredibly complex behaviour on arbitrarily small scales in phase space are the hallmarks of classical chaos.

However, quantum mechanics, the most fundamental theory we have to explain the physical world, does not see detail on arbitrarily fine scales. Plancks' constant, h, sets a limit on the resolution with which we can view phase space. Positions

and trajectories are defined by expectation values. Particles are no longer points but are waves. Energy cannot be added or removed from a quantum system unless it is in just the right quantal amounts.

What is the relationship between a classical system and its analogous quantum system? What is the relation between classical and quantum mechanics? Formal connections, such as Ehrenfest's theorem (Schiff 1960), and Poisson bracket–commutator algebra similarities (Schiff 1960, Goldstein 1980) may be established in the strict limit of $\hbar = 0$. What about in the limit of $\hbar$ small but non–zero, the so called semiclassical limit? Can we use our classical intuition in this periphery of quantum mechanics?

For classically integrable systems the marriage of classical and quantum ideas (in the semiclassical limit) gives us the methods of Einstein-Brillioun-Keller (or EBK) quantization (Geldart and Kiang 1986, Knudson and Noid 1989, Noid and Marcus 1975, Knudson et. al. 1986, Delos 1986, Goodings and Szeredi 1991). Action–angle variables are blended with a wave–like view of particles to produce an intuitive and computationally powerful tool which connects the classical and quantum systems. The phase space tori formed by the actions are used to construct the semiclassical energies and wavefunctions in the EBK quantization scheme.

No such tool exists at present for classically chaotic systems. The action–angle formalism, such a powerful tool in classically integrable systems, cannot be applied. However, progress is being made. Gutzwiller (Gutzwiller 1967, 1969, 1970,

1971) derived a remarkable formula which connects classical phase space structures with semiclassical energies. Rather than relating phase space tori to semiclassical energies (as in the EBK quantization scheme), Gutzwiller's method relates the classical periodic orbits and their properties to the semiclassical energies. Indeed, in classically chaotic systems (with hard chaos) no phase space tori exist to form a rigid skeleton of phase space. However, an infinity of periodic orbits do exist, and they take the place of the tori to form the rigid skeleton. In this sense it is natural that the periodic orbits should emerge as the elements of a quantization scheme for chaotic systems.

Gutzwiller's formula, and various extensions of it, will be used as the main tool of analysis in this thesis as we examine the connection between the classical and quantum mechanics of the wedge billiard.

In the over twenty years since the original appearance of the Gutzwiller formula only a few systems have been studied in detail. The anisotropic Kepler problem (Gutzwiller 1979, Tanner et. al. 1991, Tanner and Wintgen 1992), the hydrogen atom in a magnetic field (Wintgen 1987), and the hyperbola billiard (Sieber 1991) are the only physical systems studied to date. Only a handful of unphysical systems, mathematical in nature, (known as billiards on surfaces of constant negative curvature) have been studied (Aurich and Steiner 1992, Aurich et. al. 1992). This study of the wedge billiard is a significant addition to the short list of physical systems studied to date using the Gutzwiller formalism. This thesis is a test of the Gutzwiller formalism. Where the Gutzwiller formalism is successful we use it to illustrate the

connection between the classical wedge billiard and the quantum wedge billiard via the formalism.

The wedge billiard consists of a particle subjected to a constant downwards force (negative y direction) and confined to the region between the y axis and the line $y = x\cot\phi$, $x > 0$. This region forms a 'wedge' of angle ϕ, hence the name 'wedge billiard'. Classically, the system is Hamiltonian, the particle bounces elastically off the 'walls' (the y axis and the line $y = x\cot\phi$). Quantum mechanically, the wavefunction of the particle must vanish along the walls and also as $y \to \infty$.

Depending on the wedge angle ϕ, there are three types of classical behaviour possible in the wedge billiard. For $0° < \phi < 45°$ the wedge billiard shows Kolmogorov–Arnold–Moser (KAM) type behaviour (Arnold 1989). That is, the classical phase space shows islands of KAM tori (similar to action tori in integrable systems) surrounded by seas of chaos. The celebrated KAM theorem for nearly integrable systems describes the classical mechanics in this regime. For $\phi = 45°$ the wedge billiard is integrable. For $45° < \phi < 90°$ the wedge billiard shows 'hard chaos', all orbits are unstable and the sea of chaos fills the entire energy surface in phase space. We study the wedge billiard for $\phi > 45°$, the case of 'hard chaos', since this case is the most straightforward to deal with in the Gutzwiller formalism.

In chapter 2, we study the integrable case of $\phi = 45°$. With the 45° wedge we may illustrate the various quantization methods available for integrable systems. Also the numerical solutions to the wedge billiard which we undertake later may be

checked against the exact solutions developed in this chapter as a test of numerical accuracy. Finally, the path integral method, from which the Gutzwiller formalism is derived, is introduced.

In chapter 3 we outline a derivation of the Gutzwiller trace formula. We also derive the various extensions of the trace formula such as the dynamical zeta functions, the staircase function, and the functional relations. The Gutzwiller trace formula is also manipulated into a form whereby the classical mechanics may be obtained from the quantum eigenvalues. We will collectively call the formulas derived in this chapter as 'the Gutzwiller formalism'.

To test the Gutzwiller formalism one must know the classical periodic orbits (and their characteristic properties) and the quantum energy eigenvalues. In general, numerical methods are used to find these periodic orbits and eigenvalues. Chapter 4 details the numerical methods used to this end in the wedge billiard.

Chapter 5 details the results of the numerical calculations in the classical wedge billiard. The periodic orbits and their actions, periods, stability exponents, and Maslov indices are presented. The families of non–isolated periodic orbits, which have important consequences in the application of the Gutzwiller formalism, are discussed. The scaling properties of the periodic orbits is also discussed. Surfaces of section are presented which show the periodic orbits as the skeleton of the phase space.

In chapter 6 we come to the main results of the thesis. We present the results of the numerical calculation of the quantum eigenvalues and eigenvectors. We use the

eigenvalues and the Gutzwiller formalism to obtain information about the classical periodic orbits. We then use the Gutzwiller formalism in the opposite direction, with the classical periodic orbits as input we obtain the quantum eigenvalues. Several quantization schemes (which are presented in chapter 3) are tested, and the results between the different schemes are compared.

A concluding chapter, Chap. (7), gives an overview of the the thesis and a perspective on the results.

Finally, two appendices are included. The first deals with the derivation of the classical mappings which are used to evolve a trajectory forward in the wedge billiard. The second deals with the derivation of a smooth approximation to the exact quantum density of states.

It is hoped that the reader will feel free to 'look ahead' to the results sections of this thesis (chapters 5 & 6) when reading the theory sections (chapters 3 & 4). Often times the theory is much more understandable (and interesting) this way.

Chapter 2

The Integrable Case

The problem of a particle confined in a 45° wedge in a gravitational field is one which is classically and quantum mechanically integrable. It is a fruitful place to start our exploration of the wedge problem for several reasons.

The first reason the integrable case is interesting is because it allows us to develop some intuition for the correspondence between the classical motion and the quantum mechanical wavefunctions and energies. In using the established tools of separation of variables and Einstein-Brillioun-Keller (EBK) quantization we will see the strengths of these methods as applied to integrable systems and their shortcomings when applied to chaotic systems.

The integrable case is also an important starting point for the checking of numerical solutions. Since the answers for the 45° wedge are known exactly we may compare the solutions obtained by numerical means to the exact solutions and obtain estimates of the range of validity of the numerical methods.

2.1 The Classical Case

The classical Hamiltonian for a particle of mass m confined in a wedge of half angle ϕ in a gravitational field of strength g is given by

$$H = \frac{p_x^2}{2m} + \frac{p_y^2}{2m} + mgy = E \tag{2.1}$$

where $x > 0$ and $y \geq x\cot(\phi)$. We introduce the scaled variables (Whelan et. al. 1990, Eckhardt and Aurell 1989)

$$\begin{aligned} p_x' &= \sqrt{\frac{E'}{mE}}\, p_x & p_y' &= \sqrt{\frac{E'}{mE}}\, p_y \\ x' &= \left(\frac{mgE'}{E}\right) x & y' &= \left(\frac{mgE'}{E}\right) y \end{aligned} \tag{2.2}$$

$$t' = \sqrt{\frac{mE'}{E}}\, gt$$

and find that the Hamiltonian expressed in the scaled variables is given by

$$H' = \frac{(p_x')^2}{2} + \frac{(p_y')^2}{2} + y' = E'. \tag{2.3}$$

This means that the trajectories for any value of m,g and E are in one-to-one correspondence with trajectories at an energy E'. Thus, each trajectory of the unscaled system Eq. (2.1) is topologically equivalent to a trajectory in the scaled system Eq.

(2.3) and we need only find the solutions for a specific E' (which may be set equal to 1 or any other convenient number) to be able to infer the type of behavior at any energy. Because of this scaling property we will work with the Hamiltonian Eq. (2.3) with $E' = 1$, knowing that we may relate the trajectories found in this specific case to the general case of arbitrary m, g, E, via Eq. (2.2). Dropping the primes we get as our Hamiltonian

$$H = \frac{p_x^2}{2} + \frac{p_y^2}{2} + y = 1. \tag{2.4}$$

To solve the classical case of a wedge with half angle $\phi = 45°$ it is perhaps easiest to start by looking at the full wedge problem which consists of reflecting the half wedge in the y-axis as in Fig. (2.1). In the full wedge problem (which has full wedge angle 90°) we introduce a canonical transformation (Goldstein, 1980) to variables which run parallel to the sides of the full wedge (I.P. Cornfield et. al., 1982), X and Y via (see Fig (2.1))

$$X = \frac{x+y}{\sqrt{2}} \qquad\qquad Y = \frac{-x+y}{\sqrt{2}}. \tag{2.5}$$

Then the Hamiltonian in the new variables H_{new} becomes

$$H_{new} = \frac{p_X^2}{2} + \frac{X}{\sqrt{2}} + \frac{p_Y^2}{2} + \frac{Y}{\sqrt{2}}. \tag{2.6}$$

Since the full wedge angle is 90° a collision of the particle with one or the other

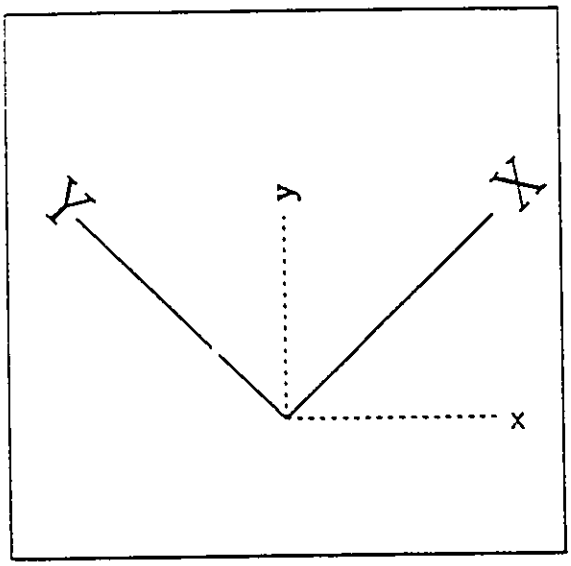

Figure 2.1: The relationship between the (x, y) variables and the (X, Y) variables

sides of the wedge merely reverses the momentum in the X or Y direction, depending on which wedge side the particle collides with. This immediately implies that the energies in the X and Y motions E_X and E_Y are *separately* conserved. The problem has separated into two one-dimensional problems, each of which is easily solveable. We may write

$$E_X = \frac{p_X^2}{2} + \frac{X}{\sqrt{2}} \tag{2.7}$$

$$E_Y = \frac{p_Y^2}{2} + \frac{Y}{\sqrt{2}} \tag{2.8}$$

where $E_X + E_Y = 1$ and $X \geq 0$ and $Y \geq 0$. The trajectory in time is determined by solving Hamilton's equations derived from Eq. (2.7) or (2.8). This trajectory is given

by

$$p_X(t) = p_X(0) - \frac{1}{\sqrt{2}}t \tag{2.9}$$

$$X(t) = X(0) + p_X(0)t - \frac{1}{2\sqrt{2}}t^2 \tag{2.10}$$

with similar equations for Y. The trajectory in each direction is bounded by energy conservation in the X and Y directions by

$$0 \leq X \leq \sqrt{2}E_X \qquad \text{and} \qquad 0 \leq Y \leq \sqrt{2}E_Y. \tag{2.11}$$

For given E_X and E_Y this trajectory fills a rectangle in the co-ordinate space of the full wedge since, in general, the periods of the X and Y motions are not commensurate. The rectangle is bounded by Eq. (2.11).

The case of the half wedge of angle $\phi = 45°$ is only a step away. The introduction of a vertical wall (i.e. along the line $X = Y$) in the full wedge simply causes the rectangle drawn in the full wedge to be reflected back on itself as if a mirror were placed along this line. This is because with each collision of the particle with this vertical wall the momenta P_X and P_Y switch places. A typical trajectory is shown in Fig. (2.2).

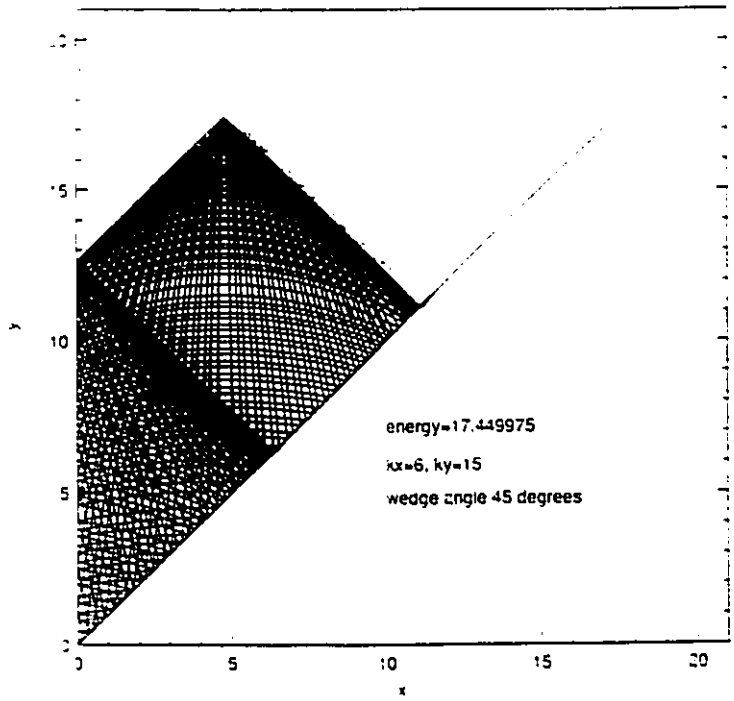

Figure 2.2: A typical trajectory in the 45° wedge

2.2 The Quantum 45° Wedge

It happens that to obtain the quantum solutions to the 45° wedge (a 2-dimensional problem) we need the solution to the 1-dimensional problem of a particle bouncing above a perfectly reflecting barrier while subjected to a constant force directed towards the barrier. This problem, called the 'quantum bouncer' by Gibbs (Gibbs 1975) will be done in three ways; exactly, using traditional EBK, and using the path integral method in the semiclassical approximation (see Goodings and Szeredi 1991). This system has been the subject of earlier papers (Gibbs 1975, Langhoff 1971, Desko and Bord 1983) and was treated in the textbook on quantum mechanics by Flügge (Flügge, 1974).

2.2.1 The 1-dimensional Quantum Bouncer: Exact Solution

Let us assume that a quantum mechanical particle of mass m exists in the region $x \geq 0$ where it is acted on by a constant force of magnitude F pointing in the negative x-direction. Its motion is described by the time independent Schrödinger equation,

$$-\frac{\hbar^2}{2m}\frac{d^2\psi}{dx^2} + Fx\psi = E\psi, \tag{2.12}$$

with the boundary conditions that $|\psi(x)|$ is finite everywhere for $x \geq 0$ and $\psi(x) = 0$ for $x \leq 0$. If the constant force is due to a uniform electric field of strength ε, $F = |q|\varepsilon$ where q is the charge of the particle. On the other hand if the force is gravitational, $F = mg$ where g is the magnitude of the acceleration due to gravity.

Following Landau and Lifshitz (Landau and Lifshitz 1958) we introduce the dimensionless variable

$$z = \left(\frac{2mF}{\hbar^2}\right)^{1/3}\frac{(E - Fx)}{F}. \tag{2.13}$$

Note that z is positive for the classically accessible region $0 \leq x \leq E/F$. Writing Eq. (2.12) in terms of z we get

$$\frac{d^2A}{dz^2} + zA = 0. \tag{2.14}$$

The boundary conditions are

$$|A(z)| \quad \text{finite} \quad \text{for} \quad -\infty \leq z \leq z_0 \tag{2.15}$$

$$A(z) = 0 \quad \text{for} \quad z \geq z_0 \tag{2.16}$$

where

$$z_0 = \left(\frac{2mF}{\hbar^2}\right)^{1/3} \frac{E}{F}. \tag{2.17}$$

The solution to Eq. (2.14) which satisfies the boundary condition Eq. (2.15) is given by the Airy function (Landau and Lifshitz 1958, Abramowitz and Stegun 1965, Gordon 1969) and has the form

$$A(z) = C\, Ai(-z)\ , \tag{2.18}$$

where C is a normalizing constant and $Ai(-z)$ is the Airy function. The allowed energy of the system is obtained by imposing the boundary condition Eq. (2.16). Writing Eq. (2.16) explicitly we obtain

$$Ai\left(-\left[\frac{2mF}{\hbar^2}\right]^{1/3} \frac{E}{F}\right) = 0, \tag{2.19}$$

We see that the exact quantum energies are related to the zeroes of the Airy function a_n by

$$-\left(\frac{2mF}{\hbar^2}\right)^{1/3} \frac{E_n}{F} = a_n$$

or

$$E_n = -a_n F \left(\frac{\hbar^2}{2mF}\right)^{1/3}. \tag{2.20}$$

Then the exact quantum wavefunction is given by

$$A_n(x) = C\, Ai_n\left(-\left[\frac{2mF}{\hbar^2}\right]^{1/3}\frac{(E_n - Fx)}{F}\right). \tag{2.21}$$

Using this exact quantum wavefunction it is possible (Goodings and Szeredi 1991) to find the approximate wavefunctions and energies in the limit of $\hbar \to 0$. Making use of the asymptotic form

$$\mathrm{Ai}(-z) = \frac{1}{3}z^{1/2}[\mathrm{J}_{1/3}(\zeta) + \mathrm{J}_{-1/3}(\zeta)], \tag{2.22}$$

where,

$$\zeta = \frac{2}{3}z^{3/2} \tag{2.23}$$

and J_ν and $J_{-\nu}$ are Bessel functions (see, for example, Shulman 1981, p.122 or Abramowitz and Stegun p.447) it is found that the approximate energy eigenvalues are given by

$$E_n = \left[\frac{3F\pi\hbar}{2\sqrt{2m}}(n + 3/4)\right]^{2/3}. \tag{2.24}$$

They are expected to be good approximations to the exact energies Eq. (2.20) as

long as $E_n >> \hbar$. The approximate eigenfunctions are

$$\psi_n(x) = \text{const}\,(E_n - Fx)^{-1/4} \sin\Big(\frac{2(2m)^{1/2}}{3F\hbar}[E_n^{3/2} - (E_n - Fx)^{3/2}]\Big) \qquad (2.25)$$

and are expected to be good approximations to the exact eigenfunctions over the range $0 < x < E_n/F$, except near the classical turning point $x_n = E_n/F$.

Eqs. (2.24) and (2.25) may be regarded as the leading order terms in the expansion of the exact quantum solutions, Eqs. (2.20) and (2.21), in powers of $\hbar$.

2.2.2 EBK Quantization

Next we turn to a the Einstein-Brillioun-Keller or EBK quantization of this problem. EBK quantization is expected to give good results in the limit of the quantities of interest being much greater than $\hbar$. Mathematically, such a limit is imposed by letting $\hbar \to 0$. Practically, this means that the high energy eigenvalues and eigenfunctions should be well predicted by the EBK quantization scheme. Several excellent articles on EBK quantization exist and the reader is referred to them for details of the method (Geldart and Kiang 1986, Knudson and Noid 1989, Noid and Marcus 1975, Knudson et. al. 1986, Delos 1986, Goodings and Szeredi 1991).

Van Vleck (Van Vleck 1928) first introduced the semiclassical (or EBK) wave-

function, which, apart from the phase $v\pi/2$ he gave as

$$\psi(X) \approx c\left(\left|\frac{\partial^2 S(x,E)}{\partial x \partial E}\right|\right)^{1/2} e^{\frac{i}{\hbar}S(x,E)-i\frac{v\pi}{2}}. \tag{2.26}$$

The quantities appearing in this equation will be defined in the following example, where we construct the wavefunction for a specific problem.

The classical Hamiltonian in our problem is given by

$$H(x,p_x) = E = \frac{p_x^2}{2m} + Fx \tag{2.27}$$

In the EBK method we write the canonical momentum p_x in terms of its conjugate variable x and the constant of the motion E as

$$p_x = \pm\sqrt{2m(E-Fx)}. \tag{2.28}$$

Eq. (2.28) defines a manifold or surface in phase space as pictured in Fig. (2.3). Starting from an arbitrary reference point x_0 (see Fig. (2.3)) and proceeding along a classical trajectory to a final point x, we define $S(x,x_0,E)$, the classical action, as

$$S(x,x_0,E) = \int_{x_0}^{x} p(E,x')dx' \tag{2.29}$$

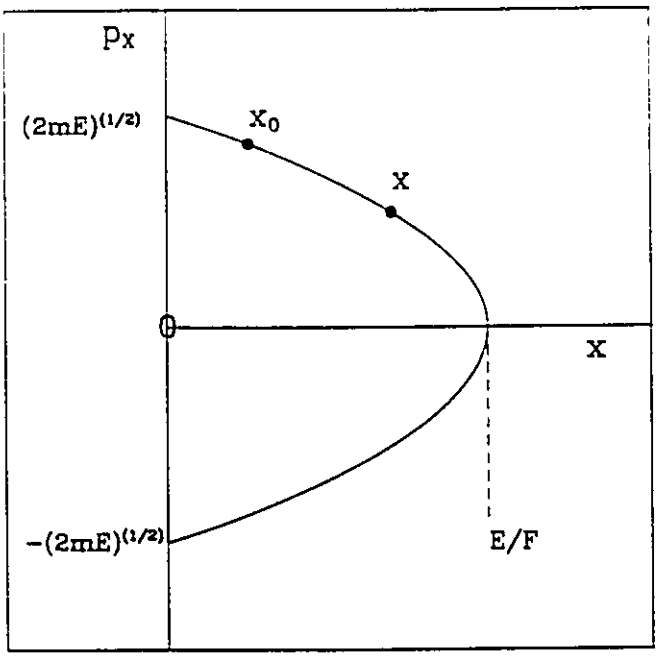

Figure 2.3: The phase space manifold for the one dimensional Hamiltonian

For this manifold we find from Eq. (1.29) that

$$\frac{\partial^2 S(x, x_0, E)}{\partial x \partial E} = \sqrt{\frac{m}{2(E - Fx)}} \tag{2.30}$$

Since this term becomes infinite at the turning point of the classical motion (the tip of the parabola, $E = Fx$) the EBK wavefunction becomes infinite at a turning point. We know that the exact quantum mechanical wavefunction is finite. Thus, we recognize that the EBK wavefunction given by Eq. (2.26) is not a good approximation to the real wavefunction near the turning points of the classical motion. Nonetheless, it may be shown (Maslov and Fedoriuk 1981) that the approximate wavefunction still gives a good representation sufficiently far from such a turning point as long as it is

is given a phase change upon passing through such an infinity. This phase change is taken care of by the Maslov index, v, appearing in the semiclassical wavefunction (Maslov and Fedoriuk 1981, Delos 1968, Schulman 1981, Creagh et. al. 1990) and is a property of the classical trajectory from x_0 to x. It is incremented by 1 if the trajectory from x_0 to x along the E manifold passes through $p_x = 0$ (the tip of the parabola in Fig. (2.3)) and incremented by 2 if there is an encounter with an infinite potential (such as at $x = 0$ in Fig (2.3)).

The EBK quantization condition arises when we force the wavefunction to be single valued around multiple circuits of the manifold in phase space. Consider the trajectory which starts and ends at x_0 and goes in a clockwise manner around the manifold.

$$\begin{aligned} S(E) &= \int_{x_0}^{E/F} p_x(E,x) + \int_{E/F}^{0} -p_x(E,x)dx + \int_{0}^{x_0} p_x(E,x)dx \\ &= \oint p_x(E,x)dx \\ &= \frac{4\sqrt{2m}}{3F}E^{3/2} \end{aligned} \tag{2.31}$$

For one circuit $v = 3$ since we add 1 for the turning point at $x = E/F$ and 2 for the momentum reversing collision at $(x = 0, p_x = -\sqrt{2mE})$. This means that the wavefunction Eq. (2.26) loses a total phase of $3\pi/2$ in one circuit of the manifold. The wavefunction starts out at $x = x_0$ with a phase of 0. For the wavefunction to have the same phase upon return we must have $S(E)/\hbar - 3\pi/2 = 2\pi n$. $S(E)$ is

a positive function so the previous equality demands that n must also be positive. Hence we choose n as $n = 0, 1, 2.....$ Using Eq. (2.31) we find that

$$\frac{4\sqrt{2m}}{3F}E^{3/2} = 2\pi\hbar(n + 3/4)$$

or

$$E_n = \left[\frac{3F\pi\hbar}{2\sqrt{2m}}(n + 3/4)\right]^{2/3} \tag{2.32}$$

exactly as before in Eq. (2.24).

In the general case of motion in one dimension one has

$$S(E) = \oint \vec{p} \cdot d\vec{q} = 2\pi\hbar(n + v/4). \tag{2.33}$$

Geometrically, the left hand side of this equation is the area bounded by the phase space manifold. Hence Eq. (2.33) says that the phase space areas defined by the manifolds corresponding to constants of the motion are quantized.

The EBK quantization condition given by Eq. (2.33) is quite general (Knudson and Noid 1989, Noid and Marcus 1975) and can be applied in cases even where it is difficult to write the phase space manifold corresponding to a specific constant of the motion in explicit form. This can occur in higher dimensional phase spaces where the manifolds corresponding to conserved quantities exist in some regions of phase space but are difficult to write down analytically. The areas in the surfaces

of section (such as x and p_x, y and p_y for a 2-dimensional system) corresponding to a constant of the motion are quantized for each surface of section according to Eq. (2.33) by varying the classical energy until the condition expressed by Eq. (2.33) is fulfilled. These are then the EBK quantum energies.

Using the energies calculated from Eq. (2.32) and using Eqs. (2.26) and (2.30) we may write the semi-classical wavefunction as

$$\psi_n(x) = c\left(\frac{m}{2(E_n - Fx)}\right)^{(1/4)} \exp(iS(x, E_n)/\hbar). \tag{2.34}$$

Taking our initial reference position as $x_0 = 0$ and using Eq. (2.29) we get

$$\psi_n(x) = c\left(\frac{m}{2(E - Fx)}\right)^{(1/4)} \exp\left(i\frac{2\sqrt{2m}}{3F\hbar}\left[E_n^{3/2} - (E_n - Fx)^{(3/2)}\right]\right). \tag{2.35}$$

To force this wavefunction to be zero at $x = 0$ we choose only the sine part of the expression and get as our EBK wavefunction

$$\psi_n(x) = c\left(\frac{m}{2(E - Fx)}\right)^{(1/4)} \sin\left(\frac{2\sqrt{2m}}{3F\hbar}\left[E_n^{3/2} - (E_n - Fx)^{(3/2)}\right]\right) \tag{2.36}$$

which is exactly the same as Eq. (2.25) calculated earlier.

2.2.3 The Path Integral Method - Introduction

Finally, we apply the path integral method in the limit of $\hbar \to 0$ to find the solution to the quantum bouncer (Goodings and Szeredi 1991).

The purpose of this section is to outline the path integral method rather than go into the quite complicated details of the algebra. Once the ideas are known the algebra is straightforward. Most equations we present are given with very little derivation, detailed justification may be found in (Goodings and Szeredi 1991, Feynman 1948) and the excellent books by Feynman and Hibbs (Feynman and Hibbs 1965) and Schulman (Schulman 1981).

The object of central interest in the path integral approach is the propagator, $G(\vec{x}_b, t; \vec{x}_a)$, which gives the probability amplitude that the particle starting from position $\vec{x}_a$ at $t = 0$ arrives at position $\vec{x}_b$ at time t. If $\vec{x}_0 = \vec{x}_a$ and $\vec{x}_N = \vec{x}_b$ and if $\vec{x}_1$, $\vec{x}_2, \ldots \vec{x}_{N-1}$ are positions of the particle at times $t_n = n\varepsilon$ $(n = 1, 2, \ldots N-1)$, where $\varepsilon = t/n$, then (see (Feynman and Hibbs 1965, p.42 or Schulman 1981 p.7),

$$G(\vec{x}_b, \vec{x}_a; t) = \lim_{N\to\infty} \int d\vec{x}_1 \ldots d\vec{x}_{N-1} \Big(\frac{m}{2\pi i\hbar\varepsilon}\Big)^{N/2}$$

$$\times \exp\Big[\frac{i\varepsilon}{\hbar} \sum_{j=0}^{N-1} \Big\{\frac{m}{2}\Big(\frac{\vec{x}_{j+1} - \vec{x}_j}{\varepsilon}\Big)^2 - V(\vec{x}_j)\Big\}\Big]. \qquad (2.37)$$

The integrations over all possible positions $\vec{x}_1, \vec{x}_2, \ldots \vec{x}_{N-1}$ are equivalent to summing over all possible broken-line paths starting at $\vec{x}_a$ and ending at $\vec{x}_b$. The factor

$[m/(2\pi i\hbar\varepsilon)]^{N/2}$ is a suitably chosen normalizing factor. It is not hard to see that in the limit as $N \to \infty$ (or $\varepsilon \to 0$), the summation in the exponential becomes,

$$\int_0^t [\frac{m}{2}(dx/dt)^2 - V(x)]dt = \int_0^t L(t)dt = W(\vec{x}_b, t; \vec{x}_a) \tag{2.38}$$

where $W(\vec{x}_b, t; \vec{x}_a)$ is Hamilton's principal function (Goldstein 1980) for a particular path from $\vec{x}_a$ to $\vec{x}_b$. It is also often called the classical action but to avoid confusing it with Eq. (2.29) (which we have already called the action) we will consistently call it Hamilton's principal function.

The Fourier transform of the propagator, defined by

$$G(\vec{x}_b, \vec{x}_a; E) = \frac{1}{i\hbar}\int_{-\infty}^{\infty} G(\vec{x}_b, \vec{x}_a; t)\exp(iEt/\hbar)dt \tag{2.39}$$

may be shown to have the form (Schiff, 1960)

$$G(\vec{x}_b, \vec{x}_a, E) = -\lim_{\epsilon\to 0}\sum_n \frac{\psi_n(\vec{x}_b)\psi_n^*(\vec{x}_a)}{(E - E_n) + i\epsilon}. \tag{2.40}$$

$G(\vec{x}_b, \vec{x}_a, E)$ is often called the energy dependent Greens function. An alternate form of $G(\vec{x}_b, \vec{x}_a, E)$ may be arrived at by a direct Fourier transform of Eq. (2.37) in the semiclassical limit. It may be shown (Schulman 1981) that in the semiclassical

approximation the Fourier transform of Eq. (2.37) is given by

$$G_{SC}(\vec{x}_b, \vec{x}_a, E) = \sum_j \left(\frac{i}{2\pi\hbar}\right)^{1/2} \left(\frac{1}{i\hbar}\right) |\tilde{D}_j|^{1/2} \exp(iS_j(E)/\hbar - iv_j\pi/2), \qquad (2.41)$$

where,

$$\tilde{D}_j = \det \begin{vmatrix} \frac{\partial^2 S_j}{\partial \vec{x}_b \partial \vec{x}_a} & \frac{\partial^2 S_j}{\partial \vec{x}_b \partial E} \\ \frac{\partial^2 S_j}{\partial \vec{x}_a \partial E} & \frac{\partial^2 S_j}{\partial E^2} \end{vmatrix} \qquad (2.42)$$

and j labels the path from $\vec{x}_a$ to $\vec{x}_b$. The function $S_j(E)$ is properly called Hamilton's characteristic function (Goldstein 1981) and what we have been calling the action. It is the same function as has appeared earlier in Eq (2.29). The integer v_j is also, as before the Maslov index encountered in Eq. (2.29).

Since Eq. (2.41) is just an alternate form of Eq. (2.40) (in the semiclassical limit) we equate them and obtain the expression

$$-\lim_{\epsilon \to 0} \sum_n \frac{\psi_n(\vec{x}_b)\psi_n^*(\vec{x}_a)}{(E - E_n) + i\epsilon} \approx \sum_{\alpha,\beta} \left(\frac{i}{2\pi\hbar}\right)^{1/2} \left(\frac{1}{i\hbar}\right) |\tilde{D}_j|^{1/2} \exp(iS_j/\hbar - iv_j\pi/2) \qquad (2.43)$$

The 'approximate' equality arises because the LHS was derived from the *exact* propagator whereas the RHS involves the *semiclassical* propagator. From the LHS we see that the product $\psi_n(\vec{x}_b)\psi_n^*(\vec{x}_a)$ involving the nth energy eigenfunction is given by the residue of the LHS at the pole E_n. This means that the poles and the residues of the RHS also determine the semiclassical energies and eigenfunctions in exactly the same way.

The goal of the path integral solution to the quantum bouncer is to calculate the RHS and find it's poles and residues. What is required in the calculation of the RHS is to identify all possible classical paths from $\vec{x}_a$ to $\vec{x}_b$ at energy E, and calculate all the quantities appearing in Eqs. (2.41 & 2.42). In complicated problems, such as those studied in quantum chaos, it is the identification of all these paths which poses the major problem in applying the path integral method.

Without going into the details of the calculation we find that the poles occur at exactly the semiclassical energies determined earlier in Eqs. (2.24) and (2.32) and the residues give the same semiclassical eigenfunctions as determined in Eqs. (2.25) and (2.36). Hence the path integral techniques, when applied to an integrable problem such as the quantum bouncer, give the same results as those obtained by EBK quantization or the $\hbar \to 0$ limit of the exact solution.

2.2.4 The 2-dimensional exact quantum solution

With all these preliminaries we are now ready to compute the solution to the 2-dimensional problem of the 45° wedge. Again, as in the classical case of the 45° wedge we look at the full 90° symmetric wedge first. In terms of the co-ordinates given in Eq. (2.5) the Schrödinger equation becomes:

$$\left(-\frac{\hbar^2}{2m}\frac{\partial^2}{\partial X^2} + \frac{mgX}{\sqrt{2}} - \frac{\hbar^2}{2m}\frac{\partial^2}{\partial Y^2} + \frac{mgY}{\sqrt{2}}\right)\psi(X,Y) = E\psi(X,Y) \qquad (2.44)$$

We may use separation of variables and set $\psi(X,Y) = A(X)B(Y)$ in Eq. (2.44) to get

$$\frac{\left(-\frac{\hbar^2}{2m}\frac{\partial^2}{\partial X^2} + \frac{mgX}{\sqrt{2}}\right)A(X)}{A(X)} + \frac{\left(-\frac{\hbar^2}{2m}\frac{\partial^2}{\partial Y^2} + \frac{mgY}{\sqrt{2}}\right)B(Y)}{B(Y)} = E. \tag{2.45}$$

This is just two one-dimensional eigenvalue problems given by

$$\left(-\frac{\hbar^2}{2m}\frac{d^2}{dX^2} + \frac{mgX}{\sqrt{2}}\right)A(X) = E_X A(X) \tag{2.46}$$

$$\left(-\frac{\hbar^2}{2m}\frac{d^2}{dY^2} + \frac{mgY}{\sqrt{2}}\right)B(Y) = E_Y B(Y) \tag{2.47}$$

where $E = E_X + E_Y$. The boundary conditions are $A(X=0) = B(Y=0) = 0$ and $A(X), B(Y)$ finite for all $X \geq 0$ and $Y \geq 0$. Eqs. (2.46) and (2.47) are just two separate one dimensional problems of the same form as Eq. (2.12), with $F = mg/\sqrt{2}$. Thus we can immediately write down the answer. Using Eq. (2.21) and $\psi(X,Y) = A(X)B(Y)$ we get as the exact wavefunction for the full wedge

$$\begin{aligned}\psi(X,Y) &= A_{n_1}(X)B_{n_2}(Y) \\ &= C_{n_1,n_2}\, Ai_{n_1}\left(-\left[\frac{2mF}{\hbar^2}\right]^{1/3}\frac{(E_X^{n_1} - FX)}{F}\right) Ai_{n_2}\left(-\left[\frac{2mF}{\hbar^2}\right]^{1/3}\frac{(E_Y^{n_2} - FY)}{F}\right)\end{aligned} \tag{2.48}$$

where C_{n_1,n_2} is a normalization constant and n_1, n_2 are the two quantum numbers labelling the wavefunction. The exact energies are (using Eq. (2.20))

$$\begin{aligned} E_{n_1,n_2} &= E_X^{n_1} + E_Y^{n_2} \\ &= -(a_{n_1} + a_{n_2})F\left(\frac{\hbar^2}{2mF}\right)^{1/3} \end{aligned} \tag{2.49}$$

where a_{n_1} and a_{n_2} are the ${n_1}^{th}$ and ${n_2}^{th}$ zeroes of the Airy functions in the X and Y directions respectively.

The half wedge solution is just a step away. For the half wedge we demand that the wavefunction vanish along the line $X = Y$ (this is the boundary condition that the wavefunction vanish along $x = 0$). Thus we choose the linear combination of primitive wavefunctions Eq. (2.48) which is the anti-symmetric with respect to reflection in the line $X = Y$ (described by interchanging X and Y) and get

$$\psi_{n_1,n_2}(X,Y) = C'\left[A_{n_1}(X)B_{n_2}(Y) - A_{n_2}(X)B_{n_1}(Y)\right] \tag{2.50}$$

Clearly, this vanishes when $X = Y$. Furthermore, it is nonzero in general only when $n_1 \neq n_2$. The energies are given by Eq. (2.49) again with the added constraint $n_1 \neq n_2$.

The entire method of solution we have just followed hinges on the fact that the wave equation Eq. (2.44) was separable in the special co-ordinate system adopted via

Eq. (2.5). This allowed us to write the wavefunction as a product of two functions $A(X)$ and $B(Y)$ and the wave equation as two one-dimensional problems. If the wave equation is non-linear or the boundary conditions are less forgiving then it is highly unlikely that the solution can be separated in this fashion. Hence, for most Hamiltonians and boundary conditions the method of separation of variables does not work. In particular, in the case of any (half) wedge angle other than 45° or 90° this method fails.

2.2.5 The 2-dimensional EBK solution

The phase space manifold in the case of the 90° full wedge is defined by the Hamiltonian Eq. (2.6). Since the energy in the X and Y directions is separately conserved we may schematically draw these manifolds as pictured in Fig. (2.4) (corresponding to a separate manifold for each constant of the motion as in Eq. (1.7) and (1.8)).

These manifolds are just the constant energy surfaces in the X and Y directions respectively. Again, since the energies in the X and Y directions are separately conserved we can quantize each manifold (defined by Eqs. (2.7) and (2.8)) on its own. We can write the full wedge solution in the EBK approximation (in analogy with Eq. (2.48)) as

$$\psi(X,Y) = A_{n_1}^{EBK}(X) B_{n_2}^{EBK}(Y)$$

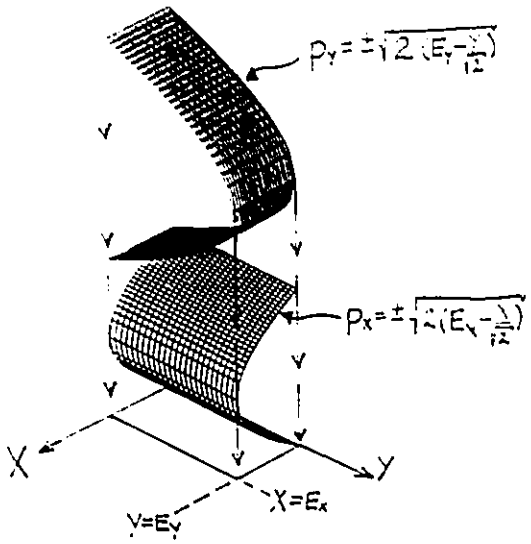

Figure 2.4: A schematic representation of the energy manifolds for the 2-dimensional case

where from Eq. (2.36)

$$A_{n_1}^{EBK}(X) = C_{n_1} \frac{\sin\left(\frac{2(2m)^{1/2}}{3F\hbar}\left[E_{n_1}^{3/2} - (E_{n_1} - FX)^{3/2}\right]\right)}{(E_{n_1} - FX)^{1/4}} \tag{2.51}$$

and C_{n_1} is an appropriate normalization constant. The Y direction EBK wavefunction $B_{n_2}^{EBK}(Y)$ is defined in exactly the same way except with X replaced by Y and n_1 replaced by n_2. The energies are given by the sum of the EBK energies in the X and Y directions respectively. From Eq. (2.32) this is (with $F = mg/\sqrt{2}$ and $m = g = 1$);

$$E_{n_1,n_2} = \left(\frac{4\pi\hbar}{3}(n_1 + 3/4)\right)^{2/3} + \left(\frac{4\pi\hbar}{3}(n_2 + 3/4)\right)^{2/3} \tag{2.52}$$

for the particle in a full wedge. Again, the half wedge problem is a step away, and by requiring the half wedge wavefunction vanish along the line $X = Y$ we arrive at

$$\psi^{EBK}_{n_1,n_2}(X,Y) = G\left[A^{EBK}_{n_1}(X)B^{EBK}_{n_2}(Y) - A^{EBK}_{n_2}(X)B^{EBK}_{n_1}(Y)\right] \tag{2.53}$$

where $n_1 > n_2$ and the $A^{EBK}_{n_1}$ and B^{EBK}_{n} are given by Eq. (2.51). The EBK energies are given by Eq. (2.52) again with the constraint $n_1 > n_2$ to make the EBK wavefunction vanish along $X = Y$. Since the EBK wavefunction only involves a sin function (see Eq. (2.51) and Eq. (2.53)) it is relatively easy to compute, as opposed to the exact wavefunction given by Eq. (2.21) and Eq. (2.50) which involves Airy functions $Ai(z)$. The EBK energy Eq. (2.52) is also very simple and does not require us knowing the zeroes of the Airy functions.

The exact solution and EBK solution to the half wedge problem for $\phi = 45°$ are shown in Fig. (2.5) and (2.6). The qualitative agreement is excellent. Also, the difference between the exact energy and the EBK energy is 0.004%. Even for the ground state ($n_1 = 1, n_2 = 0$) the difference is less than 1%. Thus, the EBK procedure does a good job at giving us approximate solutions to the separable problem.

2.3 Summary

We have found the exact wavefunction for the 45° wedge by using a change of variables to make the Schrödinger equation separable. That is, through a fortunate change of

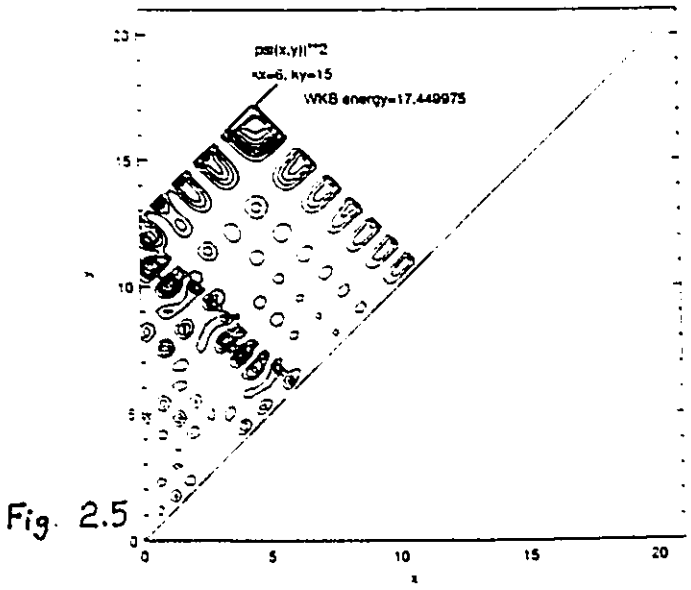

Fig. 2.5

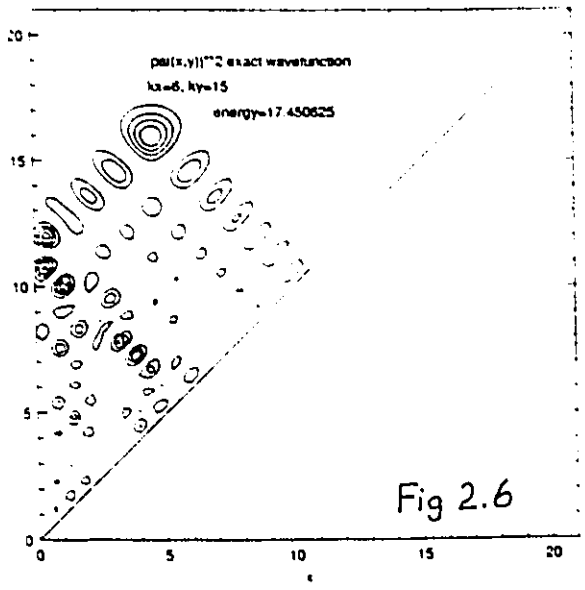

Fig 2.6

Figure 2.5: Contour plot of the EBK solution for the half wedge at $\phi = 45°$. (Compare with Fig. 2.2)

Figure 2.6: Contour plot of the exact solution for the half wedge at $\phi = 45°$. (Compare with Fig. 2.2)

variables we have turned our 2-dimensional problem into two 1-dimensional problems, which we can always solve. This was a great stroke of luck. In general, we must realize that we will not be able to find a coordinate system where the Schrödinger equation will separate neatly (along with the boundary conditions) and we will not be able to use separation of variables.

The same change of coordinates allowed us to separate the classical 2-dimensional problem into two 1-dimensional problems, each of which could be easily solved, and to separately quantize the two phase space manifolds given by the classical problem using EBK quantization. Again, without separation of variables we would have been in trouble.

We have seen that the exact and EBK solutions agree very well with each other. The energy is predicted to better than 1% for the ground state by the EBK method and the predictions get better for higher energies. Thus, we have faith that the EBK method works well in integrable systems.

Also, we note again that the EBK method may also be used in some cases where separation of variables is not possible, all that is required is the existence of separate phase space manifolds corresponding to each pair of canonically conjugate variables. This occurs in a 2N dimensional phase space if there are N separate constants of the motion relating the phase space variables. It also occurs in restricted regions of phase space where KAM tori exist (the stable islands seen is the sea of chaos in Poincare surfaces of section). Thus, even for chaotic systems, as long as

KAM tori exist there is the possibility of using EBK quantization.

Finally, the path integral approach in the semiclassical approximation gives the same results as those given by the EBK method in the case of integrable problems. This gives us faith in the path integral approach and confidence in extending it into areas where the EBK approach cannot be applied, such as in chaotic systems.

Chapter 3

The Gutzwiller Trace Formula

3.1 Introduction

The previous chapter dealt with quantizing a system when:

1. separation of variables could be used to solve the Schrödinger equation exactly,
2. one could use the 2 independent constants of the motion in the 2-dimensional problem and apply the EBK quantization procedure,
3. one could use the semiclassical propagator to approximately quantize the system.

Such methods work well if one can find a set of coordinates in which the Schrödinger equation separates or if N independent constants of the motion exist for a system with a $2N$-dimensional phase space. However, such is almost never the case.

Most Hamiltonians we deal with are not treatable in the above sense. The special cases we see presented in most textbooks on classical and quantum mechanics

(Goldstein 1980, Rasband 1991, Marion 1970, Schiff 1968, Merzbacher 1970) the simple harmonic oscillator, the hydrogen atom, particles subjected to a constant force, particles in a central force field, are rare. Real Hamiltonians are nonlinear and nonseparable, and the standard approach in physics is to make some approximations to turn the real Hamiltonian into one of the linear ones mentioned above and hope that the approximation didn't neglect anything important. Many times such an approach works, but many times it does not. Problems such as the three body problem, the N-body problem, the hydrogen atom in a magnetic field, the free particle in an enclosure of arbitrary shape, have interested people for many years and cannot be approximated by problems we already know the answer to. The Schrödinger equations are nonseparable, and too few constants of the motion exist to apply EBK quantization.

In a remarkable series of papers Gutzwiller (Gutzwiller 1967, 1969, 1970, 1971) derived a formula which has the promise of providing an EBK kind of quantization for classically chaotic systems in the semiclassical limit. This formula is known as the Gutzwiller trace formula or Gutzwiller periodic orbit sum rule. Instead of using the phase space manifolds as the classical structures around which the quantization proceeds (as in EBK), the Gutzwiller trace formula uses the 'skeleton' of the phase space in the chaotic system, the periodic orbits, as its starting point. It connects the relevant quantities in a classically chaotic system, namely the classical periodic orbits, their actions, stability exponents, Maslov indices, and periods, with the relevant quantities in the quantum system, namely the eigenfunctions and eigenvalues.

3.2 Derivation of the Trace Formula

We now turn to a sketch of the derivation of the Gutzwiller trace formula. Much detail is left out for the sake of clarity and brevity; a detailed derivation would be beyond the scope of this thesis. The interested reader may find the details in (Gutzwiller, 1971, Gutzwiller 1990, and Creagh et. al. 1991).

We start with the expression given in Eq. (2.43), which we reproduce here

$$\begin{aligned} \sum_j \left(\frac{i}{2\pi\hbar}\right)^{1/2} \left(\frac{1}{i\hbar}\right) \left(|\tilde{D}_j|\right)^{1/2} \exp(iS_j(E)/\hbar - iv_j\pi/2) &\approx -\lim_{\epsilon\to 0}\sum_n \frac{\psi_n(\vec{x}_b)\psi_n^*(\vec{x}_a)}{(E-E_n)+i\epsilon} \\ G_{SC}(\vec{x}_a,\vec{x}_b;E) &\approx -\lim_{\epsilon\to 0}\sum_n \frac{\psi_n(\vec{x}_b)\psi_n^*(\vec{x}_a)}{(E-E_n)+i\epsilon} \end{aligned} \tag{3.1}$$

It would be very nice if we could find all the paths (labelled by j) which go from $\vec{x}_a$ to $\vec{x}_b$ in a chaotic system, as is done in the path integral solution for separable systems, and obtain the energy eigenvalues and eigenfunctions just as in section (2.2.3). However, this turns out to be a very difficult task. Even for integrable systems (in more than one dimension) the enumeration of all the possible paths and the calculation of the quantities occurring in Eq. (3.1) is very difficult (Gutzwiller 1967, 1969, 1970).

Perhaps we can set our sights lower and just obtain the energy eigenvalues. This is done as follows. Set $\vec{x}_a \to \vec{x}_b = \vec{x}$ in Eq. (3.1) and integrate over all of

coordinate space (which is 2–dimensional in our case) to get

$$g(E) = \int G_{SC}(\vec{x}_a, \vec{x}_b; E)|_{\vec{x}_a \to \vec{x}_b = \vec{x}} d^2x = \lim_{\epsilon \to 0} -\sum_n \frac{1}{(E - E_n) + i\epsilon} \tag{3.2}$$

where we've used the fact that $\int \psi_n^*(\vec{x})\psi_n(\vec{x})d^2x = 1$. Then

$$\begin{aligned} \frac{g(E) - g^*(E)}{2i} &= -\frac{1}{2i}\sum_n \lim_{\epsilon \to 0}\left[\frac{1}{(E - E_n) + i\epsilon} - \frac{1}{(E - E_n) - i\epsilon}\right] \\ &= \sum_n \lim_{\epsilon \to 0} \frac{\epsilon}{(E - E_n)^2 + \epsilon^2} \end{aligned}$$

but (Arfken, 1985, Eq 8.110)

$$\lim_{\epsilon \to 0} \frac{\epsilon}{(E - E_n)^2 + \epsilon^2} = \pi\delta(E - E_n)$$

so that

$$\frac{1}{\pi}\frac{g(E) - g^*(E)}{2i} = \frac{\mathrm{Im}\{g(E)\}}{\pi} = \sum_n \delta(E - E_n). \tag{3.3}$$

Thus we see that the imaginary part of the function $g(E)/\pi$ gives us the quantum mechanical density of states. Eqs. (3.2, 3.3) are fundamental to the Gutzwiller trace formula and this thesis.

The difficult part in the derivation of the trace formula is evaluating the integral given in Eq. (3.2). To evaluate this integral we must have the semiclassical propagator which appears in this expression. The semiclassical propagator involves

all the paths that go from $\vec{x}_a$ to $\vec{x}_b$ when $\vec{x}_a \to \vec{x}_b = \vec{x}$. There are two types of paths for which this happens. The first are the paths which in the limit of $\vec{x}_a = \vec{x}_b = \vec{x}$ have very small length. The other type of path is the one which loops out into coordinate space but eventually comes back and closes on itself after a finite length. For the very small length paths $S/\hbar << 1$ as $\vec{x}_b \to \vec{x}_a$ and special methods must be used for them (Sieber 1991, Kac 1966). They give the Thomas-Fermi or Weyl contribution to the density of states and we will deal with them in Appendix B. The other paths, for which $S/\hbar >> 1$ as $\vec{x}_b \to \vec{x}_a$ are our main concern here and give an oscillatory contribution to the density of states, as we shall see. Note that these paths are not necessarily periodic, they can come back to $\vec{x}_a$ with a different momentum than they had when they left.

Thus in the limit $\vec{x}_b \to \vec{x}_a$ the propagator splits into two parts

$$G_{SC}(\vec{x}_a, \vec{x}_b; E)|_{\vec{x}_b \to \vec{x}_a = \vec{x}} = G_{S/\hbar << 1}(\vec{x}_a, \vec{x}_b; E)|_{\vec{x}_b \to \vec{x}_a = \vec{x}} + G_{S/\hbar >> 1}(\vec{x}_a, \vec{x}_b; E)|_{\vec{x}_b \to \vec{x}_a = \vec{x}} \tag{3.4}$$

Thus

$$\begin{aligned} g(E) &\approx \int G_{S/\hbar << 1}(\vec{x}_a, \vec{x}_b; E)|_{\vec{x}_b \to \vec{x}_a = \vec{x}} d^2x + \int G_{S/\hbar >> 1}(\vec{x}_a, \vec{x}_b; E)|_{\vec{x}_b \to \vec{x}_a = \vec{x}} d^2x \\ &\approx g_{TF}(E) + g_{OSC}(E) \end{aligned} \tag{3.5}$$

where

$$g_{TF}(E) = \int G_{S/\hbar<<1}(\vec{x}_a, \vec{x}_b; E)|_{\vec{x}_b \to \vec{x}_a = \vec{x}} d^2x \tag{3.6}$$

$$g_{OSC}(E) = \int G_{S/\hbar>>1}(\vec{x}_a, \vec{x}_b; E)|_{\vec{x}_b \to \vec{x}_a = \vec{x}} d^2x. \tag{3.7}$$

Using Eq. (3.1) in Eq. (3.7) gives us explicitly

$$g_{OSC}(E) = \int \left(\frac{i}{2\pi\hbar}\right)^{1/2} \left(\frac{1}{i\hbar}\right) \sum_j \sqrt{|D_j|} \exp\left(\frac{iS_j(\vec{x}_a, \vec{x}_b; E)|_{\vec{x}_b \to \vec{x}_a = \vec{x}}}{\hbar} - i\frac{\upsilon_j \pi}{2}\right) d^2x. \tag{3.8}$$

The evaluation of this integral is long and technically involved. We only outline the steps in words.

First, it is shown by appealing to arguments of stationary phase that only trajectories which are *periodic* contribute in an appreciable way to this integral. Trajectories which are *closed but non-periodic* do not contribute.

Once it has been established that only periodic orbits contribute, the 2–dimensional integral is done by integrating thin strips centered on the periodic orbits. Since the periodic orbits are dense in coordinate space (Gutzwiller, 1990) they will cover all the accessible area. If the periodic orbits are isolated in phase space then the action occurring in the exponential of Eq. (3.8) may be expanded about the periodic orbit. (A periodic orbit γ is isolated if we can find a small phase space neighbourhood of the orbit γ in which there do not exist any other periodic orbits with the same action). A further stationary phase integral is done and the resulting expression is

related to the stability properties of the neighbourhood of the periodic orbit via the stability exponents ν_γ of the 2×2 surface of section mapping matrix.

As a small aside we describe what the 2×2 surface of section mapping matrix is. If we define coordinates parallel to the periodic orbit by q_1 and in a direction perpendicular to the periodic orbit by q_2 then we may write small deviations away from the periodic orbit by $(\delta q_2, \delta p_2)$. The 2×2 surface of section mapping matrix M is defined by traversing the periodic orbit once and relating the deviations at the beginning $(\delta q_2, \delta p_2)$ and the end $(\delta q_2', \delta p_2')$ via

$$\begin{pmatrix} \delta q_2' \\ \\ \delta p_2' \end{pmatrix} = \begin{pmatrix} m_{11} & m_{12} \\ \\ m_{21} & m_{22} \end{pmatrix} \begin{pmatrix} \delta q_2 \\ \\ \delta p_2 \end{pmatrix} \tag{3.9}$$

where m_{ij} are the elements of M. It can be shown (Pars 1965) that the eigenvalues of this matrix come in pairs λ and $1/\lambda$. For the wedge billiard with wedge angle $45° < \phi < 90°$ all periodic orbits are unstable (Chernov 1991, Wojtkowski 1990) which means that λ is real and $|\lambda| > 1$. The stability exponent is defined by $\nu_\gamma = \ln|\lambda|$. The orbit is hyperbolic if $\lambda > 0$ and inverse hyperbolic if $\lambda < 0$.

The final result of the integrations and the algebraic manipulations of Eq. (3.6) is the expression

$$g(E) \approx g_{TF}(E) + g_{osc}(E)$$

$$g_{osc}(E) = \sum_{\gamma=P.P.O} \sum_{k=1}^{\infty} \frac{T_\gamma(E)}{i\hbar} \frac{\exp\left\{k\left[\frac{i}{\hbar}S_\gamma(E) - i\frac{u_\gamma \pi}{2}\right]\right\}}{\left(e^{k\nu_\gamma/2} - \sigma_\gamma^k e^{-k\nu_\gamma/2}\right)} \tag{3.10}$$

where γ labels a primitive periodic orbit, k labels its multiple traversals, $S_\gamma(E)$ is the action of the periodic orbit over one traversal, $T_\gamma(E)$ is the period, σ_γ is the sign of λ_γ and ν_γ is the stability exponent. The Maslov index u_γ counts the number of times the stable and unstable manifolds rotate about the periodic orbit along with the number of collisions with the walls and number of times the particle comes to rest over one traversal of the periodic orbit (Creagh et. al. 1990, Gutzwiller 1990, Sieber 1990). It should be noted that the label γ labels forward and backward traversals of the periodic orbits as the same orbit. Using Eq. (3.3) and Eq. (3.10) we may write the density of states, $d(E)$, as

$$\begin{aligned} d(E) &\approx d_{TF}(E) + d_{OSC}(E) \\ \sum_n \delta(E - E_n) &\approx d_{TF}(E) + d_{OSC}(E) \end{aligned}$$

$$d_{OSC}(E) = \sum_{\gamma=P.P.O} \sum_{k=1}^{\infty} \frac{T_\gamma(E)}{\pi\hbar} \frac{\cos\left(k\frac{S_\gamma(E)}{\hbar} - k\frac{u_\gamma\pi}{2}\right)}{\left(e^{k\nu_\gamma/2} - \sigma_\gamma^k e^{-k\nu_\gamma/2}\right)}. \tag{3.11}$$

Eq. (3.11) is the Gutzwiller trace formula, and as advertised at the beginning of this chapter, relates the quantities of interest in quantum mechanics (the density of states) on the LHS to the quantities of interest in classical mechanics (the periodic orbits and their properties) on the RHS.

The interpretation of the Gutzwiller trace formula is relatively straightforward. The left hand side of Eq. (3.11) is the exact quantum density of states. The

Thomas–Fermi term on the right hand side $d_{TF}(E)$ provides a smooth approximation to the density of states and the second (oscillatory term) $D_{OSC}(E)$ coming from the periodic orbits gives an oscillatory refinement to the smooth Thomas–Fermi approximation to the density of states.

If the classical mechanics of a system is 'known', that is, the periodic orbits and their actions, Maslov indices, stability exponents and periods have been calculated for a classical system at energy E then they may be inserted into the right hand side of Eq. (3.11) and the sum evaluated for that energy. Evaluating the right hand side (as a function of energy) should give one peak at the energy eigenvalues. In this sense the classical mechanics is giving us information about the quantum mechanics.

If the periodic orbits bifurcate and coalesce, or are born and disappear as the energy is changed then computing the sum on the right hand side becomes complicated. First, all the periodic orbits have to be identified at each energy E and then the relevant classical quantities calculated and then these are inserted into the sum on the right hand side. This process must be repeated for every energy E at which the sum is to be evaluated. Things become considerably simpler for systems which 'scale' with energy (Whelan et. al. 1990, Eckhardt and Aurell 1989) like the wedge billiard. For scaleable systems the periodic orbits must only be found once at an arbitrary energy E'. The periodic orbits at any other energy E have the same shape and topology and are simply related by a scale transformation (Eq. (2.2)). This means that the action also scales simply with energy. Using Eqs. (2.2, 2.29) we

find that the classical action and period scale with energy as ($m = g = 1$)

$$S'_\gamma(E') = \left(\frac{E'}{E}\right)^{3/2} S_\gamma(E), \qquad T'_\gamma(E') = \left(\frac{E'}{E}\right)^{1/2} T_\gamma(E). \tag{3.12}$$

We choose to do all our classical calculations at $E' = 1$ so

$$S_\gamma(E) = S_\gamma(1)E^{3/2} \tag{3.13}$$

Also, we can relate the classical period and action by (Pars 1965, Goldstein 1980)

$$T_\gamma(E) = \frac{\partial S_\gamma(E)}{\partial E}. \tag{3.14}$$

Using Eqs. (3.14, 3.12) we get

$$T_\gamma(E) = \frac{3}{2} S_\gamma(1)E^{1/2} \tag{3.15}$$

The Maslov index and stability exponents only depend on the topology of the periodic orbit and are both independent of energy. Using Eqs. (3.15,3.13) we may write the oscillatory part of the density of states in the Gutzwiller trace formula for the wedge billiard as

$$d_{OSC}(E) = \sum_{\gamma=P.P.O} \sum_{k=1}^{\infty} \frac{3S_\gamma(1)E^{1/2}}{2\pi\hbar} \frac{\cos\left(k\frac{S_\gamma(1)E^{3/2}}{\hbar} - k\frac{u_\gamma\pi}{2}\right)}{\left(e^{k\nu_\gamma/2} - \sigma_\gamma^k e^{-k\nu_\gamma/2}\right)} \tag{3.16}$$

Notice that if we write Eq. (3.11) as

$$\sum_n \delta(E - E_n) \approx \sum_{\gamma=P.P.O} \sum_{k=1}^{\infty} A_\gamma \cos\left(k\frac{S_\gamma(E)}{\hbar} - k\frac{u_\gamma \pi}{2}\right) \tag{3.17}$$

then the RHS looks like a kind of Fourier cosine sum over waves which have wavelengths given by the actions of the periodic orbits of the system. This Fourier sum over the periodic orbits conspires to produce delta function peaks at the energy eigenvalues of the quantum system.

What is the minimum eigenvalue difference which may be resolved using a finite number of classical periodic orbits up to action S_{max} (or T_{max})? We see (Berry 1981) that the oscillations in energy in Eq. (3.11) have a wavelength ΔE given by

$$\begin{aligned} \frac{S_\gamma(E+\Delta E)}{\hbar} - \frac{S_\gamma(E)}{\hbar} &= 2\pi \\ \left(\frac{S_\gamma(E+\Delta E) - S_\gamma(E)}{\Delta E}\right)\Delta E &= 2\pi\hbar \\ \frac{\partial S_\gamma(E)}{\partial E}\Delta E &= 2\pi\hbar \end{aligned}$$

and using $T_\gamma(E) = \partial S_\gamma(E)/\partial E$

$$\Delta E = \frac{2\pi\hbar}{T_\gamma(E)} \tag{3.18}$$

For the wedge billiard we use Eqs. (3.15,3.13) in Eq. (3.18) to find that

minimum energy difference we can resolve between two eigenvalues is

$$\Delta E_{min} = \frac{4\pi\hbar}{3S_{max}(1)E^{1/2}} \tag{3.19}$$

We expect that energy eigenvalues closer together than ΔE_{min} will not be resolved by the Gutzwiller trace formula. Since the distance between energy eigenvalues ΔE is approximately $\Delta E \approx 1/d_{TF}(E)$ and from Eq. (B.20) $d_{TF}(E) \approx E^2/4\pi\cot\phi$ we will not be able to resolve eigenstates beyond energy

$$E = (3S_{max}\cot\phi)^{2/3} \tag{3.20}$$

using periodic orbits of $S_\gamma \leq S_{max}$. Eq. (3.20) sets a limit on our ability to resolve individual eigenvalues. Also, the number of periodic orbits below action S_{max} is expected to increase exponentially with increasing S_{max}. It has been pointed out (Voros 1988, Eckhardt and Aurell 1989) that even though the contributions of the periodic orbits to the Gutzwiller trace formula are being damped exponentially by their stability exponents the number of periodic orbits may be growing at a faster rate and the Gutzwiller trace formula may not converge or may only be conditionally convergent. These details will be kept in mind when doing our numerical work.

3.2.1 Classical Mechanics from Quantum Mechanics

Can the classical mechanics of a chaotic system tell us about the quantum mechanics of the analogous quantum system? From the Gutzwiller trace formula in the form of Eq. (3.11) the energy eigenvalues may be computed from the classical periodic orbits and their properties and hence we may answer this question 'yes'. A related question which naturally arises is 'Can the classical periodic orbits (and their properties) be computed from the quantum energy eigenvalues?'. We have found that the answer to the second question is again 'yes'. Other authors (Aurich and Steiner 1992, Sieber and Steiner 1990c, Wintgen 1987, Biswas et. al. 1991) have also found that much classical information can be obtained from the quantum eigenvalues alone. In some sense it has been argued (Kleppner, 1991) that this second question is the more fundamental since quantum mechanics is the more fundamental theory and it should be able to explain the limiting case of classical chaos.

This section details the manipulations required to put the Gutzwiller trace formula for the wedge billiard into a form where it is transparent that the quantum eigenvalues 'know' about the classical periodic orbits. We essentially do a damped Fourier sine or cosine transform of the Gutzwiller trace formula to make this clear. This method is similar to that used by Sieber and Steiner 1990c, where they use a function called the 'cosine modulated heat kernel'. However, in the case of the wedge billiard we must choose different functional forms in order to allow us to analytically

do the resulting integrals. Insert Eq. (3.16) in Eq. (3.11), multiply both sides by a function (arbitrary for now) $h(E^{3/2})$, and integrate over energy $\int_0^\infty dE$ to get

$$\sum_n h(E_n^{3/2}) = \int_0^\infty d_{TF}(E)h(E^{3/2})dE + \sum_{\gamma=P.P.O}\sum_{k=1}^{\infty}\frac{3S_\gamma(1)}{2\pi\hbar}\frac{\int_0^\infty E^{1/2}\cos\left(k\frac{S_\gamma(1)E^{3/2}}{\hbar}-k\frac{u_\gamma\pi}{2}\right)h(E^{3/2})dE}{\left(e^{k\nu_\gamma/2}-\sigma_\gamma^k e^{-k\nu_\gamma/2}\right)} \tag{3.21}$$

Since, as explained in the last section, the right hand side may only be conditionally convergent we want to cut off the contributions of long periodic orbits. Also, the right hand side of the Gutzwiller sum Eq. (3.11) makes it clear that the energy spectrum is made up of distinct 'frequencies' of waves whose wavelengths (and hence frequencies) are determined by the actions of the classical periodic orbits. Doing a Fourier transform will reveal these frequencies and hence the actions of the classical periodic orbits. With this motivation we choose as our function

$$h(E^{3/2}) = e^{-\alpha E^{3/2}}\sin(\omega E^{3/2}). \tag{3.22}$$

The integrals given in Eq. (3.21) are evaluated and the result is

$$\sum_n e^{-\alpha E_n^{3/2}} \sin(\omega E_n^{3/2}) = \frac{\tan(\phi)}{3\pi\hbar^2}\frac{\omega\alpha}{(\alpha^2+\omega^2)^2} - \frac{(1+\sec(\phi))}{3\pi\hbar\sqrt{2}}\frac{\omega}{\alpha^2+\omega^2} + \sum_\gamma \sum_{k=1}^{\infty} \frac{S_\gamma(1)}{4\pi\hbar} \frac{[\sin(ku_\gamma\pi/2)\,P(\omega) + \cos(ku_\gamma\pi/2)\,C(\omega)]}{e^{k\nu_\gamma/2} - \sigma_\gamma^k e^{-k\nu_\gamma/2}} \tag{3.23}$$

where $C(\omega)$ and $P(\omega)$ are the so called crossing and peak functions respectively given by

$$C(\omega) = \frac{\omega - k\frac{S_\gamma(1)}{\hbar}}{\left(\omega - k\frac{S_\gamma(1)}{\hbar}\right)^2 + \alpha^2} \tag{3.24}$$

and

$$P(\omega) = \frac{\alpha}{\left(\omega - k\frac{S_\gamma(1)}{\hbar}\right)^2 + \alpha^2}. \tag{3.25}$$

Both sides of Eq. (3.23) must now be viewed as functions of the variable ω (E and ω are conjugate variables in this transform). The first two terms on the right hand side result from the Thomas–Fermi term in the Gutzwiller trace formula and are only significant at small ω. Our main interest lies in the third term.

If the energy eigenvalues are known they may be inserted into the left hand side of Eq. (3.23). The parameter α may be chosen to cut off the contributions from eigenvalues past some point. The (quantum) curve which results from plotting the left hand side has some kind of structure as a function of ω. How do we interpret this

structure?

The third term on the right hand side, plotted as a function of ω, says that there should be peaks and crossings occurring at integral multiples of the actions of the periodic orbits (in units of $\hbar$) $S_\gamma(1)$. It should be noted that the Maslov index u_γ is always an integer and this means that, for a certain value of k, one of $\cos(ku_\gamma\pi/2)$ or $\sin(ku_\gamma\pi/2)$ is zero while the other is non–zero. Hence the contribution to the function from a particular periodic orbit is seen as a series of peaks and crossings as a function of ω. The width of the peaks and crossings is determined by the parameter α. If we know many eigenvalues accurately then we may choose α to be small and the corresponding peaks and crossings will be sharply defined. If only a few eigenvalues are known accurately then we may cut off the contribution from the higher eigenvalues by choosing α large on the left hand side. Of course, this has the effect of broadening the peaks and crossings. The amplitude of the crossings and peaks is determined by the action of the periodic orbit and its stability exponent. For large ω the contribution is damped exponentially at a rate determined by the stability exponent.

Hence, if we know the energy eigenvalues then plotting the left hand side of Eq. (3.23) tells us a great deal about the classical orbits. We shall undertake just such a study later in this thesis.

Another choice of function for $h(E^{3/2})$ is

$$h(E^{3/2}) = e^{-\alpha E^{3/2}}\cos(\omega E^{3/2}) \tag{3.26}$$

The integrals given in Eq. (3.21) are again evaluated and we arrive at

$$\sum_n e^{-\alpha E_n^{3/2}} \cos(\omega E_n^{3/2}) = \frac{\tan\phi}{4\pi\hbar^2}\frac{1}{\alpha^2+\omega^2} - \frac{2\omega^2}{\hbar^2(\alpha^2+\omega^2)^2} - \frac{(1+\sec(\phi))}{3\pi\hbar\sqrt{2}}\frac{\alpha}{\alpha^2+\omega^2} + \frac{1}{6} + \sum_\gamma \sum_{k=1}^{\infty} \frac{S_\gamma(1)}{4\pi\hbar} \frac{[\cos(ku_\gamma\pi/2)\,P(\omega) - \sin(ku_\gamma\pi/2)\,C(\omega)]}{e^{k\nu_\gamma/2} - \sigma_\gamma^k e^{-k\nu_\gamma/2}}. \tag{3.27}$$

Eq. (3.23) and Eq. (3.27) provide similar information and both will be used later in this thesis.

3.2.2 The quantum staircase $N(E)$

The left hand side of the Gutzwiller trace formula Eq. (3.11) is just the exact quantum density of states. The Thomas–Fermi term on the right hand side provides a smooth approximation to the density of states and the second (oscillatory term) coming from the periodic orbits gives an oscillatory refinement to the smooth Thomas–Fermi approximation to the density of states.

If both sides of the Gutzwiller trace formula are integrated with respect to energy from 0 to E (using Eq. (3.11)) we find

$$N(E) = \sum_n \theta(E - E_n) \approx N_{TF}(E) + \sum_\gamma \sum_{k=1}^{\infty} \frac{1}{\pi k} \frac{\left[\sin\left(k\frac{S_\gamma(E)}{\hbar} - k\frac{u_\gamma\pi}{2}\right) + \sin\left(k\frac{u_\gamma\pi}{2}\right)\right]}{\left(e^{k\nu_\gamma/2} - \sigma_\gamma^k e^{-k\nu_\gamma/2}\right)} \tag{3.28}$$

where

$$N_{TF}(E) = \int_0^E d_{TF}(E')dE' \tag{3.29}$$

and θ is the step function

$$\theta(x) = \begin{cases} 0 & x < 0 \\ 1 & x \geq 0 \end{cases}. \tag{3.30}$$

The left hand side of Eq. (3.28) is the exact quantum staircase. Each time the energy E increases past an energy eigenstate E_n the quantum staircase discontinuously increases by one. The Thomas–Fermi term on the right hand side is the smooth approximation to the exact quantum staircase, and the second term on the right hand side is the oscillatory correction to the smooth Thomas–Fermi term.

For the wedge billiard we find, using Eqs. (3.11,3.16)

$$\begin{aligned} N(E) &= \sum_n \theta(E - E_n) \approx N_{TF}(E) + N_{OSC}(E) \\ &\approx N_{TF}(E) + \sum_\gamma \sum_{k=1}^{\infty} \frac{1}{\pi k} \frac{\left[\sin\left(k\frac{S_\gamma(1)E^{3/2}}{\hbar} - k\frac{u_\gamma \pi}{2}\right) + \sin\left(k\frac{u_\gamma \pi}{2}\right)\right]}{\left(e^{k\nu_\gamma/2} - \sigma_\gamma^k e^{-k\nu_\gamma/2}\right)} \end{aligned} \tag{3.31}$$

where, from Eq. (B.20)

$$N_{TF}(E) = \frac{1}{12\pi\hbar^2 \cot\phi} E^3 - \frac{1}{6\pi\hbar}\sqrt{\frac{2}{m}}(1 + \sec\phi)E^{3/2} + 1/6 \tag{3.32}$$

As an example of how the staircase function is used we look at a simple and novel quantization procedure recently proposed by Aurich et. al. (Aurich and

Steiner 1992, Aurich et. al. 1992) based on the staircase function. Their quantization condition reads

$$\cos\left(\pi\left\{N_{TF}(E)+N_{OSC}(E)\right\}\right)=0. \tag{3.33}$$

This quantization condition takes advantage of the information contained in the Thomas–Fermi term as well as the periodic orbits, as we shall see in Sec. (6.6).

3.2.3 The dynamical zeta function

The dynamical zeta function is essentially just the oscillatory term coming from the periodic orbits in the Gutzwiller trace formula re–written as an infinite product rather than an infinite sum (Gutzwiller 1979, Voros 1988, Sieber 1991). Its usefulness lies in the possibility that the infinite product may converge faster than the conditionally convergent Gutzwiller trace formula.

The derivation of the zeta function as a product is straightforward. Starting with Eq. (3.10) we do the following manipulations

$$\begin{aligned}
g(E) &\approx g_{TF}(E)+\sum_{\gamma=P.P.O}\sum_{k=1}^{\infty}\frac{T_\gamma(E)}{i\hbar}\frac{\exp\left\{k\left[\frac{i}{\hbar}S_\gamma(E)-i\frac{u_\gamma\pi}{2}\right]\right\}}{\left(e^{k\nu_\gamma/2}-\sigma_\gamma^k e^{-k\nu_\gamma/2}\right)}\\
&\approx g_{TF}(E)+\sum_{n=0}^{\infty}\sum_{\gamma}\sum_{k=1}^{\infty}\frac{T_\gamma(E)\left(\sigma_\gamma^k\right)^n}{i\hbar}\exp\left\{k\frac{i}{\hbar}S_\gamma(E)-ik\frac{u_\gamma\pi}{2}-k\frac{\nu_\gamma}{2}-nk\nu_\gamma\right\}\\
&\approx g_{TF}(E)+\sum_{n=0}^{\infty}\sum_{\gamma}\frac{T_\gamma(E)\sigma_\gamma^n}{i\hbar}\frac{\exp\left\{\frac{i}{\hbar}S_\gamma(E)-i\frac{u_\gamma\pi}{2}-\frac{\nu_\gamma}{2}-n\nu_\gamma\right\}}{1-\sigma_\gamma^n\exp\left\{\frac{i}{\hbar}S_\gamma(E)-i\frac{u_\gamma\pi}{2}-\frac{\nu_\gamma}{2}-n\nu_\gamma\right\}}\\
&\approx g_{TF}(E)+\sum_{\gamma}\sum_{n=0}^{\infty}\frac{d}{dE}\ln\left(1-\sigma_\gamma^n\exp\left\{\frac{i}{\hbar}S_\gamma(E)-i\frac{u_\gamma\pi}{2}-\frac{\nu_\gamma}{2}-n\nu_\gamma\right\}\right)
\end{aligned}$$

$$g(E) \approx g_{TF}(E) + \frac{d \ln Z(E)}{dE} \tag{3.34}$$

$$g(E) \approx g_{TF}(E) + \frac{1}{Z(E)} \frac{dZ(E)}{dE} \tag{3.35}$$

where

$$Z(E) = \prod_{\gamma} \prod_{k=0}^{\infty} \left(1 - \sigma_{\gamma}^{k} \exp\left\{\frac{i}{\hbar} S_{\gamma}(E) - i\frac{u_{\gamma}\pi}{2} - \frac{\nu_{\gamma}}{2} - k\nu_{\gamma}\right\}\right) \tag{3.36}$$

and we have used the fact that $T_{\gamma}(E) = dS_{\gamma}(E)/dE$.

$Z(E)$ is the dynamical zeta function. Since $g(E)$ has poles at the energy eigenvalues E_n it can be seen from Eq. (3.35) that the dynamical zeta function will have zeroes at the energy eigenvalues (in general $dZ(E)/d(E) \neq 0$ when $Z(E) = 0$). Hence the energy eigenvalues are given by the zeroes of the dynamical zeta function and our quantization condition becomes

$$Z(E_n) = 0. \tag{3.37}$$

One disadvantage of the dynamical zeta function is that it is a complex function and in general only complex E_n will solve Eq. (3.37). Of course the exact quantum energy eigenvalues must be real, and any complex part to them must be attributable to a using a finite number of periodic orbits in the product Eq. (3.36), the truncation of the product over k in Eq. (3.36), the semiclassical approximations used in deriving the Gutzwiller trace formula, or the non–convergence of the Gutzwiller

trace formula for the particular case being studied. One simple remedy is to plot the magnitude of $Z(E)$ as a function of real energy E. Then the zeroes close to the real energy axis will produce pronounced minima and the (unphysical) zeroes far away in the complex plane will be less likely to produce minima along the real axis.

Alternatively, if only real E are used and the function $Z(E)$ is plotted in the complex plane then in general it will describe a curve which winds around the origin, coming close (but not necessarily touching) the origin at the energy eigenvalues E_n.

The dynamical zeta function may be re–written in yet another form known as a Dirichlet series (Berry and Keating 1990, Sieber and Steiner 1992). From Sieber and Steiner 1992 we arrive at (after some detailed manipulations)

$$Z(E) = 1 + \sum_{n=1}^{\infty} A_n \exp\left\{\frac{i}{\hbar} S_n(E)\right\} \tag{3.38}$$

where

$$S_n(E) = \sum_{i=1}^{k} m_i S_{\gamma_i}(E) \tag{3.39}$$

and

$$A_n = \prod_{i=1}^{k} \frac{(-1)^{m_i} \exp\left\{\frac{-i m_i u_{\gamma_i} \pi}{2} - \frac{\nu_{\gamma_i} m_i (m_i - 1)}{4}\right\} \sigma_{\gamma_i}^{m_i(m_i-1)/2}}{\prod_{j=1}^{m_i} \left(\exp\left(\frac{j\nu_{\gamma_i}}{2}\right) - \sigma_{\gamma_i}^{j} \exp\left(-\frac{j\nu_{\gamma_i}}{2}\right)\right)}. \tag{3.40}$$

The label n refers to *psuedo orbits* (Berry and Keating 1990), where the pseudo orbits are linear combinations of the periodic orbits γ_i, with all γ_i different and the m_i being arbitrary positive integers.. The $S_n(E)$ are called *pseudo actions.*

Hence, we have found two ways of rewriting the Gutzwiller sum as a zeta function. The first, infinite product form is given in Eq. (3.36). The second, Dirichlet series form, is given in Eqs. (3.38,3.39,3.40). For both of these zeta functions the quantization condition for the semiclassical energies is that Eq. (3.37) hold.

3.2.4 Cycle expansions

Cycle expansions (Cvitanović 1988,1991, Cvitanović and Eckhardt 1989, Artuso et. al. 1991a,b) have been proposed as a way of writing the dynamical zeta function in a more convergent form. The idea is to expand the product over the periodic orbits given in Eq. (3.36) as follows (setting $k = 0$)

$$\begin{aligned} Z_o(E) &= \prod_\gamma \left(1 - \exp\left\{\frac{i}{\hbar}S_\gamma(E) - i\frac{u_\gamma \pi}{2} - \frac{\nu_\gamma}{2}\right\}\right) \\ &= \prod_\gamma (1 - t_\gamma) \\ &= 1 - \sum_f t_f - \sum_c t_c \end{aligned} \tag{3.41}$$

where

$$t_\gamma = \exp\left\{\frac{i}{\hbar}S_\gamma(E) - i\frac{u_\gamma \pi}{2} - \frac{\nu_\gamma}{2}\right\}. \tag{3.42}$$

t_f are the so–called *fundamental* terms and t_c are the so–called *curvature* corrections. For more details and very instructive examples the reader is referred to the excellent papers by Artuso et. al. 1991a,b.

A short example is given here for clarity. Suppose we have no pruning of the dynamics (see Secs. (4.3, 5.2)) and all possible orbits labelled by words up to length 4 are included in the zeta product. Then,

$$\begin{aligned} Z_o(E) &= (1-t_V)(1-t_T)(1-t_{TV})(1-t_{TTV}) \\ &\quad \times(1-t_{TVV})(1-t_{TTTV})(1-t_{TTVV})(1-t_{TVVV}) \\ &= 1 - \overbrace{t_V - t_T}^{\text{fundamental terms}} \\ &\quad -(t_{TV}-t_Tt_V)-(t_{TTV}-t_Tt_{TV})-(t_{TVV}-t_{TV}t_V) \\ &\quad -(t_{TTTV}-t_Tt_{TTV})-(t_{TTVV}-t_{TTV}t_V)-(t_{TVVV}-t_{TVV}t_V)+\ldots \end{aligned}$$

The fundamental terms are supposed to give the dominant contributions to the zeta product. The second line and third lines contain the curvature corrections which (may) cancel in pairs, giving exponentially small corrections. If one has complete dynamics with no pruning then this may indeed be the case.

A prerequisite for the effective use of the cycle expansions is that the pruning rules must be known. If the pruning rules are not known then the cycle expansions are expected to converge no better than the Gutzwiller trace formula (Artuso et. al. 1991a,b).

As we shall see, in the wedge billiard the pruning rules are not known. Nonetheless, we proceed optimistically with the following cycle expansion based on

our above example. Define

$$Z(E) = \prod_k Z_k(E) \tag{3.43}$$

where

$$Z_k(E) = 1 - \sum_f t_f - \sum_c t_c. \tag{3.44}$$

and

$$t_f = \sigma_f^k exp\left\{\frac{i}{\hbar} S_\gamma(E) - i\frac{u_\gamma \pi}{2} - \left(k + \frac{1}{2}\right)\nu_\gamma\right\}. \tag{3.45}$$

and the curvature terms are given by

$$t_c = t_j - t_k t_l. \tag{3.46}$$

The word corresponding to the orbit j must be a cyclic permutation of the word formed from appending the word for the orbit k to the word for the orbit l (i.e. in the above example $TTVV = TTV + V$).

3.2.5 Functional Relations

'Functional relations' (Tanner et. al. 1991, Tanner and Wintgen 1992, Berry and Keating 1990, Keating 1992a,b, Sieber and Steiner 1992) forms of the Gutzwiller trace formula are yet another rearrangement of terms in the Gutzwiller sum. They also take advantage of the information contained in the Thomas–Fermi term and have the added benefit that they have zeroes at real energies E, as opposed to the complex

zeroes encountered with the zeta functions.

The derivation of the functional relation begins with the expression for the quantum staircase Eq. (3.28).

$$\begin{aligned} N(E) &\approx N_{TF}(E) + \sum_{\gamma}\sum_{k=1}^{\infty}\frac{1}{\pi k}\frac{\left[\sin\left(k\frac{S_\gamma(E)}{\hbar} - k\frac{u_\gamma\pi}{2}\right) + \sin\left(k\frac{u_\gamma\pi}{2}\right)\right]}{\left(e^{k\nu_\gamma/2} - \sigma_\gamma^k e^{-k\nu_\gamma/2}\right)} \\ &\approx N_{TF}(E) + \mathrm{Im}\sum_{\gamma}\sum_{k=1}^{\infty}\frac{1}{\pi k}\frac{\exp\left(ik\frac{S_\gamma(E)}{\hbar} - ik\frac{u_\gamma\pi}{2}\right)}{\left(e^{k\nu_\gamma/2} - \sigma_\gamma^k e^{-k\nu_\gamma/2}\right)} \\ &\quad \mathrm{Im}\sum_{\gamma}\sum_{k=1}^{\infty}\frac{1}{\pi k}\frac{\exp\left(ik\frac{u_\gamma\pi}{2}\right)}{\left(e^{k\nu_\gamma/2} - \sigma_\gamma^k e^{-k\nu_\gamma/2}\right)} \end{aligned} \tag{3.47}$$

From here the next line is obtained by doing exactly the same steps as in the derivation of the dynamical zeta function Eq. (3.36).

$$\pi N(E) \approx \pi N_{TF}(E) - \mathrm{Im}\left\{\ln Z(E)\right\} - \mathrm{Im}\left\{\ln Z^*(0)\right\} \tag{3.48}$$

where $Z(E)$ is the dynamical zeta function defined before in Eq. (3.36). Writing $Z(E)$ in polar form

$$Z(E) = r(E)e^{i\xi(E)} \tag{3.49}$$

where $r(E)$ and $\xi(E)$ are real functions we find upon substituting into Eq. (3.48) that

$$\xi(E) = \pi N_{TF}(E) - \pi N_{TF}(E) + \xi(0). \tag{3.50}$$

Using this in Eq. (3.49) gives

$$e^{-i\pi N_{TF}(E)} Z(E) e^{-i\pi\xi(0)} = r(E) e^{-i\pi N(E)}. \tag{3.51}$$

Now, $N(E)$ is the exact quantum staircase function and it is always equal to some positive integer or zero. Thus $e^{-i\pi N(E)}$ is real. Multiplying both sides of Eq. (3.51) by $r(0)$ we get

$$Z^*(0) Z(E) e^{-i\pi N_{TF}(E)} = r(0) r(E) e^{-i\pi N(E)} \tag{3.52}$$

The right hand side of this equation is purely real, so the left hand side must also be real. Also, since $Z(E)$ has zeroes at the energy eigenvalues then so should the real function

$$f(E) = Z^*(0) Z(E) e^{-i\pi N_{TF}(E)} \tag{3.53}$$

We can define a new, purely real function $F(E)$, by

$$F(E) = \frac{Z^*(E) e^{i\pi N_{TF}(E)} + Z(E) e^{-i\pi N_{TF}(E)}}{2}$$

and using Eq. (3.38), if the A_n are real, we find

$$F(E) = \cos[\pi N_{TF}(E)] + \sum_{n=1}^{\infty} A_n \cos[\pi N_{TF}(E) - S_n(E)/\hbar] \tag{3.54}$$

where the $S_n(E)$ are actions of linear combinations of orbits as detailed in Eqs. (3.38,3.39,3.40). When written in this form it is apparent that already, on aver-

age, the zeroes of $F(E)$ lie at the correct eigenenergies because of the first cosine term in Eq. (3.54). The second term gives oscillatory corrections to the locations of these zeroes.

The resummation achieved in Eq. (3.54), it has been argued (Berry and Keating 1990), will optimize the use of the information contained in the periodic orbits and lead to efficient evaluation of the energy eigenvalues. Unfortunately, the A_n in the wedge billiard are not real, as we shall see in later chapters and so we cannot use Eq. (3.54).

Nonetheless, Eq. (3.53) may be used with Z(E) in its product form (Eq. (3.36)), Dirichlet series form (Eq. (3.38), and cycle expansion form Eqs. (3.43-3.46), to evaluate energy eigenvalues. We shall undertake such an evaluation later Sec. (6.7).

Chapter 4

Numerical Methods

4.1 Introduction

In the previous chapter we derived the Gutzwiller trace formula Eq. (3.11) and its related re–arrangements. They will serve as our main tool of analysis in studying the connection between classical and quantum chaos. The Gutzwiller trace formula relates a sum over the eigen–energies of the quantum system to a sum over the classical periodic orbits, their actions, stability exponents, periods and Maslov indices. If we want to use the Gutzwiller trace formula, or check the approximate equality between the quantum and classical sides then we must know all the quantities entering into the formula. It is to this task we now turn our attention.

4.2 Numerical calculation of quantum wavefunctions and energies

The Schrödinger wave equation for the particle in the wedge is given in circular cylindrical co–ordinates by

$$\left[-\frac{\hbar^2}{2m}\left(\frac{1}{\rho}\frac{\partial}{\partial\rho}\left(\rho\frac{\partial}{\partial\rho}\right)+\frac{1}{\rho^2}\frac{\partial^2}{\partial\phi^2}\right)+mg\rho\cos\phi\right]\psi(\rho,\phi)=E\psi(\rho,\phi) \qquad (4.1)$$

with boundary conditions

$$\psi(\rho,0)=0 \quad (4.1b) \qquad \psi(\rho,\phi_\circ)=0 \quad (4.1c) \qquad \psi(\rho\to\infty,\phi)=0 \quad (4.1d)$$

where $\phi_\circ$ is the wedge angle and the angle ϕ is measured in a clockwise direction from the y–axis. We make this equation dimensionless by introducing the variable

$$\tilde{\rho}=\left(\frac{m^2g}{\hbar^2}\right)^{1/3}\rho. \qquad (4.2)$$

Then Eq. (4.1) becomes

$$\left[-\frac{1}{2\tilde{\rho}}\frac{\partial}{\partial\tilde{\rho}}\left(\tilde{\rho}\frac{\partial}{\partial\tilde{\rho}}\right)-\frac{1}{2\tilde{\rho}^2}\frac{\partial^2}{\partial\phi^2}+\tilde{\rho}\cos\phi\right]\psi(\tilde{\rho},\phi)=\tilde{E}\psi(\tilde{\rho},\phi) \qquad (4.3)$$

where

$$\tilde{E} = \frac{E}{(\hbar m^{1/2} g)^{2/3}} \tag{4.4}$$

From now on we will measure energy in the units given in Eq. (4.4) and length in the units given in Eq. (4.2). With these conventions we will drop the ˜ on $\tilde{\rho}$ and $\tilde{E}$.

We choose to write $\psi(\rho, \phi)$ as a sum of product of functions

$$\psi(\rho, \phi) = \sum_{lm} C_{lm} P_l(\rho) \Phi_m(\phi) \tag{4.5}$$

with

$$\Phi_m(\phi) = \sqrt{\frac{2}{\phi_o}} \sin\left(\frac{m\pi\phi}{\phi_o}\right) \quad m = 1, 2, 3, \ldots m_{max} \tag{4.6}$$

where ϕ_o is the wedge angle, and

$$P_l(\rho) = \sqrt{\frac{2}{\rho\rho_o}} \sin\left(\frac{l\pi\rho}{\rho_o}\right) \qquad l = 1, 2, 3 \ldots l_{max} \tag{4.7}$$

where ρ_o is some arbitrary length. The Φ_m and P_l satisfy the orthogonality conditions $\int_0^{\phi_o} \Phi_m(\phi)\Phi_p(\phi)d\phi = \delta_{m,p}$ and $\int_0^{\rho_o} P_l(\rho)P_q(\rho)\rho d\rho = \delta_{l,q}$ respectively. With Eq. (4.6) as the angular function we see that the wavefunction already satisfies the boundary condition given in Eq. (4.1b,c). Using Eq. (4.5) we find Eq. (4.3) becomes

$$\sum_{lm} C_{lm} \left[-\frac{\hbar^2}{2m} \left(\frac{1}{\rho} \frac{\partial}{\partial \rho} \left(\rho \frac{\partial}{\partial \rho} \right) - \frac{1}{\rho^2} \left(\frac{m\pi}{\phi_o} \right)^2 \right) + mg\rho\cos\phi \right] P_l(\rho)\Phi_m(\phi) = E P_l(\rho)\Phi_m(\phi) \tag{4.8}$$

We now multiply both sides of Eq. (4.8) by $P_q(\rho)\Phi_p(\phi)$ and integrate over all of space $\int_0^{\rho_\circ} \rho d\rho \int_0^{\phi_\circ} d\phi$ to get

$$\sum_{lm} \left\{ \left\{ \frac{1}{2} \left(\frac{l\pi}{\rho_\circ} \right)^2 \delta_{ql} + \left[\frac{1}{2} \left(\frac{m\pi}{\phi_\circ} \right)^2 - \frac{1}{8} \right] A_{ql} \right\} \delta_{pm} + B_{ql,mp} \right\} C_{lm} = \sum_{lm} C_{lm} E \delta_{ql} \delta_{pm} \tag{4.9}$$

or

$$\sum_{lm} K_{lm,qp} C_{lm} = E C_{qp} \tag{4.10}$$

where

$$K_{lm,qp} = \left\{ \frac{1}{2} \left(\frac{l\pi}{\rho_\circ} \right)^2 \delta_{ql} + \left[\frac{1}{2} \left(\frac{m\pi}{\phi_\circ} \right)^2 - \frac{1}{8} \right] A_{ql} \right\} \delta_{pm} + B_{ql,mp} \tag{4.11}$$

and

$$\begin{aligned} A_{ql} &= \int_0^{\rho_\circ} \frac{P_q(\rho) P_l(\rho)}{\rho} d\rho \\ &= -\frac{1}{4\rho_\circ} \int_0^{\rho_\circ} \frac{1}{\rho^2} \sin\left(\frac{q\pi\rho}{\rho_\circ} \right) \sin\left(\frac{l\pi\rho}{\rho_\circ} \right) d\rho \end{aligned} \tag{4.12}$$

and

$$B_{ql,mp} = \int_0^{\rho_\circ} P_q(\rho) P_l(\rho) \rho^2 d\rho \int_0^{\phi_\circ} \Phi_m(\phi) \Phi_p(\phi) \cos\phi d\phi \tag{4.13}$$

$$= \frac{-16(q-l)^{-2}(q+l)^{-2}\rho_\circ q l (-1)^{m+p} m p \phi_\circ \sin\phi_\circ \left((-1)^{q+l} - 1 \right)}{[-(m-p)\pi + \phi_\circ][(m+p)\pi + \phi_\circ][-(m+p)\pi + \phi_\circ][(m-p)\pi + \phi_\circ]} \qquad q \neq l \tag{4.14}$$

$$= \frac{-2\rho_\circ (-1)^{m+p} m p \pi^2 \sin\phi_\circ}{[-(m-p)\pi + \phi_\circ][(m+p)\pi + \phi_\circ][-(m+p)\pi + \phi_\circ][(m-p)\pi + \phi_\circ]} \qquad q = l$$

(4.15)

Eq. (4.10) is exactly the form of an eigenvalue–eigenvector equation

$$K \cdot \vec{C} = E\vec{C}$$

with matrix elements for the matrix K given by Eq. (4.10). Such equations are straightforward to solve numerically on a computer. The results are a set of energies E_n labelled by an index n. Corresponding to each allowed E_n there is an eigenvector $\vec{C}_n$. The wavefunctions for each E_n are then easily constructed from Eq. (4.5).

The dimension of the matrix K is $(m_{max}l_{max}) \times (m_{max}l_{max})$ where l_{max} and m_{max} are defined in Eqs. (4.6, 4.7). The larger we choose l_{max} and m_{max} the smaller detail we will be able to reproduce accurately in the wavefunction Eq. (4.5). However, this increases the dimensions of the matrix we must diagonalize. Also, the parameter ρ_o, which enters the definition of the radial basis functions, Eq. (4.7), also sets a detail scale in the problem.

We can estimate the values of some of these parameters as follows. Since the radial basis functions we have chosen force the wavefunction to go to zero at $\rho = \rho_o$ none of the wavefunctions we are interested in may extend to ρ_o or beyond, otherwise they will be artificially cut off. For a wedge angle of ϕ_o a classical particle of energy $E = \rho_o \cos\phi$ could just slide up the tilted wall and reach ρ_o. If the quantum

wavefunctions are to accurately describe such motion and not reach past ρ_o this means that the quantum energies must also be $E = \rho_o \cos\phi$ or less. Re-arranging gives $\rho_o = E/\cos\phi$. From Eq. (3.29) we know that the energy below which there are N quantum eigenstates is approximately given by $E \approx (12\pi \cot\phi\, N)^{1/3}$. Thus, using this equation in the previous one gives

$$\rho_o = \frac{(12\pi \cot\phi\, N)^{1/3}}{\cos\phi}$$

The expectation value for the radial kinetic energy when $C_{l_{max}m_{max}} = 1$, $C_{lm} = 0, \quad l \neq l_{max}, \quad m \neq m_{max}$ is given from the first term in Eq. (4.11) as

$$E = \frac{1}{2}\left(\frac{l_{max}\pi}{\rho_o}\right)^2.$$

Using $\rho_o = E/\cos\phi$ we get

$$l_{max} \approx \frac{\sqrt{2}}{\pi\cos\phi} E^{3/2}$$

Also, assuming that the detail we wish to resolve in the angular direction is about the same as in the radial direction we choose $m_{max} = l_{max}$.

As an example, if we want to have 300 eigenvalues accurately calculated for a 49° wedge then from the above arguments $E_{300} \approx 21.43$ and $\rho_o \approx 32.65$. For $E_{300} \approx 21.43$ we find $l_{max} \approx 68$.

Similarly, for a 60° wedge we find that if we want about 200 eigenvalues then

$N \approx 200$, $E_{200} \approx 18.5$, $\rho_o \approx 37$ and $l_{max} \approx 72$.

4.3 Numerical Calculation of the Classical Mechanics: Periodic orbits

For the classical mechanics we need to know the periodic orbits, their actions, periods, stability exponents, Maslov indices, and the sign of the eigenvalues of the monodromy matrix σ.

A first step in finding the periodic orbits lies in developing an effective and unique labelling scheme corresponding to the label γ in Eq. (3.11). Any trajectory may be labelled by the sequence of collisions the particle makes with the walls of the wedge. If we start off with the particle on the tilted wall (the line $y = (\cot\phi)x$) then the particle may do one of three things before returning to the tilted wall (see Fig. (4.1)). First, it can return directly to the tilted wall with no intervening collisions with the vertical wall or wedge vertex. Such a bounce will be labelled a T bounce. Second, it can undergo a collision with the vertical wall between successive collisions with the tilted wall. Such a bounce will be labelled a V bounce. Finally, the particle may go directly into the wedge vertex. Such a bounce is labelled a B bounce. The three letters, T V and B are referred to as an *alphabet* (Artuso et. al. 1990a,b). The label γ corresponds to *words* formed by these three letters. The sequence of letters describes the sequence of collisions the trajectory has undergone and hence its

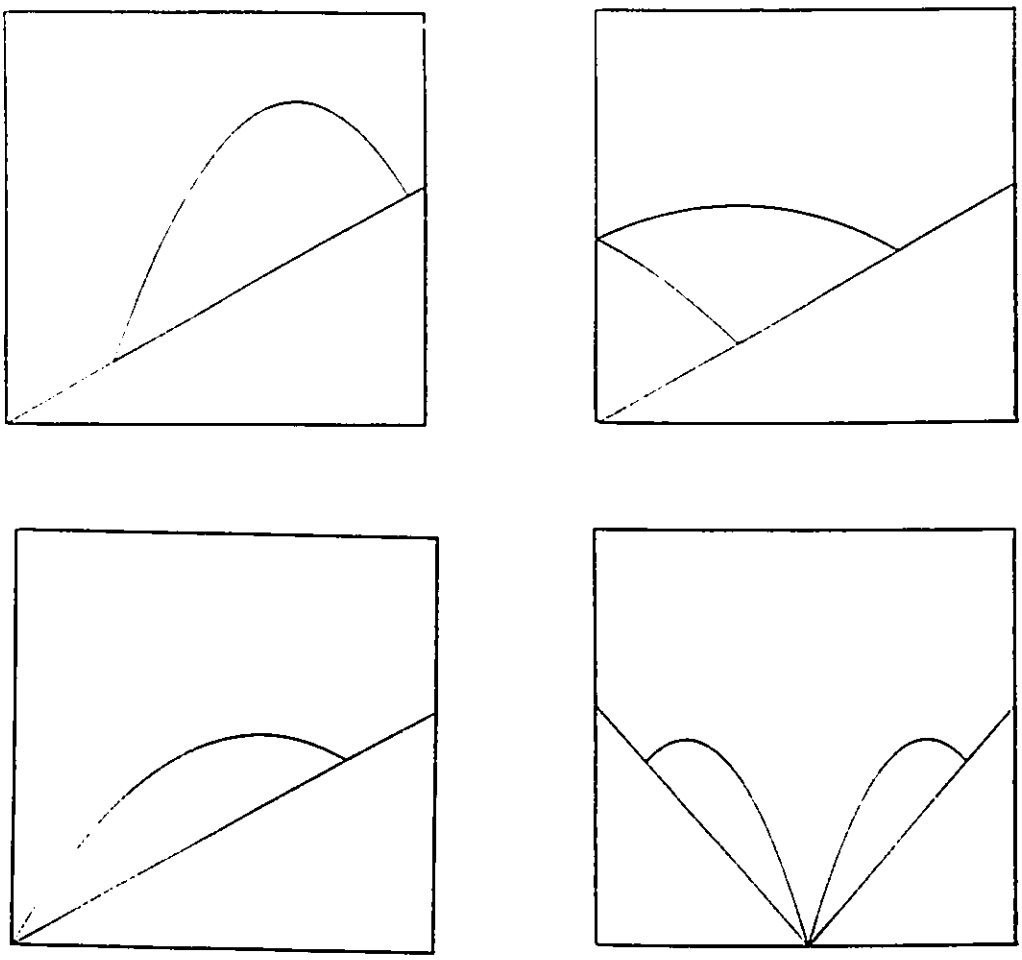

Figure 4.1: The three types of bounces possible in the wedge. The top left figure shows a T bounce. The top right figure shows a V bounce. The bottom left figure shows a B bounce. The bottom right figure shows a B bounce in the symmetric wedge

history. A typical non-periodic trajectory may have a label consisting of an infinity of non-repeating letters $\gamma = ...TVVTTTVVVTVTTVTTVVVVVTVTVTVVTV...$.

If the trajectory goes directly into the wedge vertex it reverses on itself. This may be understood by considering the symmetric wedge and looking at what happens to a particle falling directly into its vertex (see Fig. (4.1)). Because of symmetry the particle must leave the vertex with the same x momentum as it had when it entered, while the y momentum reverses sign. It is as if there was just a flat floor on which the particle bounced. In the case we are considering, the asymmetric wedge, this means that the particle must retrace its path after a collision with the wedge vertex (labelled by a B bounce). Typically, such trajectories are labelled by sequences such as $\gamma = ...TVVTVBVTVVT...$ where the sequence is symmetric with respect to reflection about the letter B. Lehtihet and Miller (Lehtihet and Miller 1986) discuss these B bounces at some length and show that much of the phase space structure for $\phi < 45°$ may be explained in terms of them.

Typical *periodic trajectories* are labelled by sequences of letters which eventually repeat, such as $\gamma = ...TTTVTTTVTTTVTTTV....$ *Primitive periodic orbits* are labelled by the shortest segment which is repeated in such an orbit, such as $\gamma = TTTV$ in the previous example.

We have conjectured that at all wedge angles, $45° < \phi < 90°$, each primitive periodic orbit may be uniquely labelled by a word consisting of the binary alphabet T,V. Numerical evidence supporting this conjecture will be presented later.

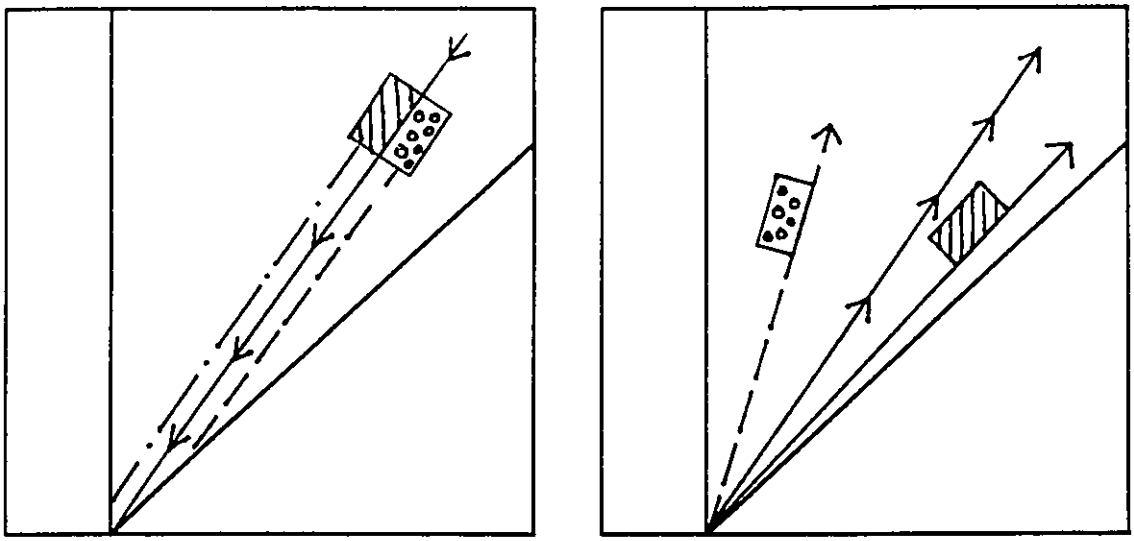

Figure 4.2: The coordinate space neighbourhood of an orbit entering the wedge at wedge angle $45° < \phi < 90°$. The central orbit is shown as a solid line entering the wedge vertex in the left figure. The neighbourhood of the central orbit is drawn as two rectangles, one hatched and the other spotted. Before the collision the coordinate space around the central orbit is connected (left figure). After the collision the coordinate space (and phase space) becomes disconnected (see right figure).

The letter B does not occur in the label of any primitive periodic orbit we are interested in. The reason is that the phase space neighbourhood around orbits which enter the wedge vertex becomes disconnected and diverges macroscopically from the central orbit as the central orbit leaves the wedge vertex (see Fig (4.2)). This means that initially small deviations from the central orbit do not remain small and the eigenvalues of the monodromy matrix defined in Eq. (3.9) are effectively infinite. Thus the stability exponents ν_γ are infinite. The stability exponents enter the trace formula Eq. (3.11) in the denominator as $\exp(k\nu_\gamma/2) - \sigma_\gamma^k \exp(-k\nu_\gamma/2)$ and thus in the limit $\nu_\gamma \to \infty$ the contribution from all periodic orbits which enter the wedge

vertex is zero. Since we have in mind the application of the periodic orbits in the trace formula no periodic orbits with a B contribute. The only exception to this rule is one periodic orbit which was pointed out to us by U. Smilansky. This orbit occurs at wedge angle $\phi = 60°$, and we call it the *vertex orbit.* It turns out that for this particular primitive periodic orbit the coordinate space does not become disconnected and the vertex orbit enters with a finite stability exponent. We will discuss the vertex orbit in more detail later.

The possible n–letter words which describe primitive periodic orbits are given by all possible n–letter combinations of the binary alphabet T, V with the following restrictions. The n–letter word is not a multiple traversal of a shorter word, it is not a reversed sequence of another n–letter word, and that it is not a cyclic permutation of another n–letter word. A table of possible words up to length 8 is included in Table (4.1).

Note that although each primitive periodic orbit is uniquely labelled by a word not all words correspond to primitive periodic orbits. The dynamics is said to be *pruned* (Artuso et. al. 1990a,b).

Now that we have a unique labelling scheme for the periodic orbits (consisting of a word formed from Ts and Vs) we proceed as follows. Introduce the variables X and Y, defined along the tilted wall via (Lehtihet and Miller 1986)

$$X = \tan(\phi_o)p_x + p_y \tag{4.16}$$

n	word	n	word	n	word	n	word
1	V	6	TTTVVV	7	TTVVVVV	8	TTTVVVVV
2	TV	6	TTVTVV	7	TVTVTVV	8	TTVTTVTV
3	TTV	6	TTVVVV	7	TVTVVVV	8	TTVTTVVV
3	TVV	6	TVTVVV	7	TVVTVVV	8	TTVTVTVV
4	TTTV	6	TVVVVV	7	TVVVVVV	8	TTVTVVTV
4	TTVV	7	TTTTTTV	8	TTTTTTTV	8	TTVTVVVV
4	TVVV	7	TTTTTVV	8	TTTTTTVV	8	TTVVTVVV
5	TTTTV	7	TTTTVTV	8	TTTTTVTV	8	TTVVVVVV
5	TTTVV	7	TTTTVVV	8	TTTTTVVV	8	TVTVTVVV
5	TTVTV	7	TTTVTTV	8	TTTTVTTV	8	TVTVVTVV
5	TTVVV	7	TTTVTVV	8	TTTTVTVV	8	TVTVVVVV
5	TVTVV	7	TTTVVVV	8	TTTTVVVV	8	TVVTVVVV
5	TVVVV	7	TTVTTVV	8	TTTVTTVV	8	TVVVVVVV
6	TTTTTV	7	TTVTVTV	8	TTTVTVTV		
6	TTTTVV	7	TTVTVVV	8	TTTVTVVV		
6	TTTVTV	7	TTVVTVV	8	TTTVVTVV		

Table 4.1: All allowed n-letter combinations for the binary alphabet T and V up to word length 8.

$$Y = \cot(\phi_o)p_x - p_y \tag{4.17}$$

where p_x and p_y refer to the momentum of the particle just after a collision with the tilted wall. Note that this X and Y are not the same as the variables introduced earlier in Eq. (2.5). Then the conservation of energy along the tilted wall demanded by Eq. (2.4), written in the variables X and Y, becomes

$$\frac{1}{2}\left\{\cos^2\phi_o X^2 + \sin^2\phi_o Y^2\right\} + r\cos\phi_o = 1 \tag{4.18}$$

where, as usual

$$x = r\sin\phi_o \tag{4.19}$$

and since we are on the tilted wall

$$y = \cot(\phi_\circ)x. \tag{4.20}$$

From Eqs. (4.16 – 4.20) we see that if X and Y are known then we may solve uniquely for x, y, p_x, p_y. Thus, along the tilted wall there are only two free variables, X and Y.

We can find mappings which take us from initial conditions (X_i, Y_i) just after a collision with the tilted wall to just after the next collision with the tilted wall (X_f, Y_f). These mappings are derived in a straightforward way from the equations of motion. A derivation is given in Appendix A. We quote the results here. From Eqns. (A.19, A.20) the T bounce mapping is

$$\begin{aligned} X_f &= X_i + 2Y_i \\ Y_f &= Y_i \end{aligned} \tag{4.21}$$

and the V bounce the mapping is

$$\begin{aligned} X_f &= -X_i - Y_i + Y_f \\ Y_f &= -\sqrt{4 + 2\xi[X_i + Y_i]^2 - Y_i^2}. \end{aligned} \tag{4.22}$$

where

$$\xi = \cos(2\phi_\circ)\cos^2(\phi_\circ) \tag{4.23}$$

Given some initial condition (X_i, Y_i) the next bounce is either a T or a V. In practice we always map with a T map and check to see if the final point is still in the wedge. If it is not then the V map is used instead. In this way any initial condition is mapped forward to successive collisions with the tilted wall. No numerical integration of trajectories between collisions is required, and this results in being able to reliably follow orbits for longer periods of time. The final point (X_f, Y_f) is given by the composition of mappings describing the sequence of bounces. As an example, for the code $\gamma = TTVTV$ we have

$$\begin{pmatrix} X_f(X_i, Y_i) \\ \\ Y_f(X_i, Y_i) \end{pmatrix} = V \circ T \circ V \circ T \circ T \begin{pmatrix} X_i \\ \\ Y_i \end{pmatrix}$$

The periodic orbits occur when $(X_f, Y_f) = (X_i, Y_i)$. Hence we look for the zeroes of the 2–dimensional function

$$F(X_i, Y_i) = X_f(X_i, Y_i) - X_i \tag{4.24}$$

$$G(X_i, Y_i) = Y_f(X_i, Y_i) - Y_i \tag{4.25}$$

The zeroes of Eqns. (4.24, 4.25) are precisely the initial conditions for a periodic orbit.

The zeroes of such 2–dimensional functions may be found using a 2–dimensional Newton method (Bountis and Helleman 1978). If the initial guess is (X_0, Y_0) then

the next iteration (X_1, Y_1) is given by

$$X_1 = X_0 + \Delta X \qquad Y_1 = Y_0 + \Delta Y \tag{4.26}$$

where ΔX and ΔY are given by

$$\left.\begin{pmatrix} \frac{\partial F(X,Y)}{\partial X} & \frac{\partial F(X,Y)}{\partial Y} \\ \frac{\partial G(X,Y)}{\partial X} & \frac{\partial G(X,Y)}{\partial Y} \end{pmatrix}\right|_{(X_0,Y_0)} \begin{pmatrix} \Delta X \\ \Delta Y \end{pmatrix} = - \left.\begin{pmatrix} F(X,Y) \\ G(X,Y) \end{pmatrix}\right|_{(X_0,Y_0)} \tag{4.27}$$

Eqns. (4.26, 4.27) are iterated until a certain zero tolerance is achieved. Typically we choose the tolerance 1×10^{-12}. This actually gives us $X_f - X_i \approx 10^{-14}$, $Y_f - Y_i \approx 10^{-14}$.

How does one choose an initial (X, Y)? From the definition of Y, Eq. (4.17) we find that $Y \leq 0$ just after a collision with the tilted wall. Eq. (4.18) with $r = 0$ defines the extremities of the energy surface in (X, Y) space. Thus, all points inside the half ellipse

$$\frac{X^2}{(2/\cos^2\phi_o)} + \frac{Y^2}{(2/\sin^2\phi_o)} = 1 \qquad Y < 0 \tag{4.28}$$

are possible starting points for the Newton method. In practice a 100×100 mesh is set up on this ellipse and the mesh points are chosen as initial conditions for the Newton method. Typically only a small number of these points converge to the fixed point, the longer the word the less initial guesses actually converge. To make sure that we are always finding the same fixed point inside the ellipse (i.e. that our fixed point is unique) we keep track of the accumulated distance d between the fixed points

found from different starting guesses. If (X_i, Y_i) is the fixed point found on the i^{th} convergence and (X_{i+1}, Y_{i+1}) is the fixed point found on the $(i+1)^{th}$ convergence then we keep track of

$$d = \sum_{i=1}^{N-1} \sqrt{(X_{i+1} - X_i)^2 + (Y_{i+1} - Y_i)^2} \tag{4.29}$$

where N is the number of times the Newton method converges inside the half ellipse. Typically, for N convergences d scales as $d \approx N(1 \times 10^{-14})$. This is consistent with the Newton method always converging to the same fixed point and hence the fixed point being unique. We have checked that d is small for many orbits. In practice we do not compute d for all the orbits because of time constraints.

For longer word lengths, typically words of 12 letters or more, sometimes a 100×100 mesh is not fine enough to find an initial guess which converges. Then a $2^n00 \times 2^n00$ mesh is used where n is increased until we find a point of convergence.

The limit of this method is reached when the words are approximately 16 to 18 letters long. At this point the numerics becomes unstable and the zero tolerance cannot be reached. Subdividing the mesh further does not help, and increasing the zero tolerance moves you too far off the periodic orbit to be meaningful. However, some orbits which we are interested in remain stable to word lengths of 50 letters or more.

4.3.1 Calculation of the Action and Period

The classical action between successive collisions with a wall is straightforward to evaluate directly from its definition Eq. (2.29). If the orbit leaves one wall with phase space coordinates $(x_i, y_i, p_{xi}, p_{yi})$ and reaches another wall with phase space coordinates $(x_f, y_f, p_{xf}, p_{yf})$ then using Eq. (2.27) (with $E = m = F = 1$) we get

$$S(x_f, y_f, x_i, y_i; 1) = p_x(x_f - x_i) + \frac{1}{3}\left[\left(2(1-y_i) - p_x^2\right)^{3/2} - \left(2(1-y_f) - p_x^2\right)^{3/2}\right]. \tag{4.30}$$

The action for the entire periodic orbit is just the sum of the actions of each segment of the orbit between wall collisions.

The time between successive collisions with a wall is given by the equation of motion for the p_y variable

$$T = p_{yi} - p_{yf}. \tag{4.31}$$

The period of the orbit is the sum of the times along each segment of the orbit.

Another way of finding the period of the periodic orbit T_γ if the action S_γ is known is by using the relation given in Chap (2.3), Eq. (3.15) $T_\gamma(E) = (3(S_\gamma(1)/2)\sqrt{E}$. I have numerically verified that these two different methods of calculating the periods of periodic orbits give the same results.

4.3.2 Calculation of the Stability Exponents

The stability exponent ν for a periodic orbit may be calculated several different ways.

The first way is to explicitly calculate the 2×2 monodromy matrix Eq. (3.9) for the periodic orbit and diagonalize it to obtain its eigenvalues $\lambda, 1/\lambda$ where $\lambda > 1$. Then, $\nu = \ln|\lambda|$. This method also gives us the eigenvectors, which point along the unstable (for the eigenvalue λ) and stable (for the eigenvalue $1/\lambda$) directions in (q_2, p_2) space.

Typically what is done to calculate the 2×2 monodromy matrix numerically is the following. We choose a starting point on the periodic orbit and define a line perpendicular to the orbit at this point. This line is our surface of section. We make a small deviation in the q_2 direction (along the perpendicular line) (typically $\delta q_2 \approx 10^{-8}$) and no deviation in the perpendicular momentum $\delta p_2 = 0$. We follow this deviated trajectory around one traversal of the periodic orbit until it strikes the perpendicular line again. This final point is given by $(\delta q_2', \delta p_2')$. Then the first column of the monodromy matrix may be calculated from

$$m_{11} = \frac{\delta q_2'}{\delta q_2} \qquad m_{21} = \frac{\delta p_2'}{\delta q_2}$$

Repeating the procedure for $\delta q_2 = 0, \delta p_2 \neq 0$ gives the second column of the 2×2 monodromy matrix.

Another way of calculating the stability exponent is to diagonalize the 3×3

monodromy matrix defined in Appendix A. It turns out that the eigenvalues of the 3×3 monodromy matrix are $\lambda, 1/\lambda, 1$ where $\lambda, 1/\lambda$ are the same as the eigenvalues of the 2×2 monodromy matrix. All that is needed to calculate the 3×3 monodromy matrix is to know the word for an orbit and where the trajectory strikes the tilted wall at each collision. Then the eigenvalues of the 3×3 monodromy matrix give the stability exponents in a straightforward way.

The sign of the eigenvalues of the monodromy matrix, σ_γ is given by the sign of λ_γ. $\sigma_\gamma = 1$ for hyperbolic orbits and $\sigma_\gamma = -1$ for orbits which are hyperbolic with reflection.

In the computer programs the 3×3 monodromy matrix is used to find the stability exponents because it is numerically much more reliable than the 2×2 monodromy matrix method. This is because some orbits have stability exponents of ≈ 10 or more which means that initial deviations away from the periodic orbit grow by a factor of $22,000 \approx 10^4$ over one traversal of the orbit! An initial deviation of 10^{-8} used in calculating the 2×2 monodromy matrix may not stay close enough to the orbit after one traversal to give accurate results. Also, all deviated trajectories tend to line up with the unstable manifold since phase space is expanding so rapidly in that direction and hence the stable manifold is very difficult to calculate. It is this difficulty of calculating the stable manifold which poses the biggest problem to the 2×2 monodromy matrix method. On the other hand, the unstable manifold (its direction and expansion rate) is given very well by the 2×2 monodromy matrix method. As a

consequence of Liouville's theorem the product of the eigenvalues of either the 2×2 or 3×3 monodromy matrix must be 1 (Gutzwiller 1990). Once the stability exponent gets larger than about 6 the product of the eigenvalues of the 2×2 stability matrix deviates significantly from 1 (by about 10%). Invariably it is the $1/\lambda$ eigenvalue which is incorrect for the reasons stated above. The product of the eigenvalues of the 3×3 monodromy matrix is always 1 to 10 or more decimal places for all periodic orbits we have found. Hence we use it to calculate the stability exponents.

4.3.3 Calculation of the Maslov Index

The Maslov index u was calculated using a method based on that suggested by Creagh et. al. (Creagh et. al. 1990). Creagh et. al. show that the Maslov index for a system with a smooth potential (no hard wall collisions) is given by twice the number of times the unstable manifold rotates around the periodic orbit over one traversal. We define the angle of the unstable manifold, θ, in the (q_2, p_2) plane as being the angle between the chosen branch of the unstable manifold and the q_2 axis. Then the method of Creagh et. al. is equivalent to adding 1 to the Maslov index each time the chosen branch of the unstable manifold becomes vertical by passing through 90° or −90° while rotating in the clockwise direction (clockwise means θ is decreasing).

For systems with hard wall collisions it is also required to add 2 to the Maslov index each time a collision occurs (Shulman 1981, Sieber 1991). Finally, every time the particle comes to a stop, i.e. $(p_x = 0, p_y = 0)$, the Maslov index is incremented

by 1 (Creagh et. al. 1990, Sieber 1991).

This prescription for calculating the Maslov indices was carried out as follows. First, the 2×2 monodromy matrix was calculated as in the last section. The eigenvector corresponding to the λ eigenvalue locates a given branch of the unstable manifold (the other branch points in the opposite direction). A trajectory (the deviated trajectory) is then started out along the unstable manifold a small distance away from the periodic orbit (typically 10^{-8}). The deviated trajectory, as we follow it in time, will stay on the unstable manifold. We allow the central periodic trajectory to evolve in time and construct successive surfaces of section along the central orbit. We then see where the deviated trajectory strikes these surfaces of section and find the angle, $\theta(t)$, of the unstable manifold in the (q_2, p_2) plane as a function of time. Each time the unstable manifold becomes vertical by θ passing through $90°$ or $-90°$ rotating in the clockwise direction we add 1 to the Maslov index. The number of collisions with the walls is given by twice the number of V bounces plus the number of T bounces in the word describing the periodic orbit. Each collision adds 2 to the Maslov index. Finally, we check to see whenever the momentum is zero and add 1 to the Maslov index for each occurrence. Hence by following the central periodic trajectory and a deviated trajectory over one traversal we find the Maslov index for the orbit.

Chapter 5

Classical Mechanics: Results

5.1 Introduction

This chapter deals with the classical mechanics of the wedge billiard for $45° < \phi < 90°$. We will emphasize the classical mechanical results which are needed later on for our quantum work but include some aspects of the classical mechanics which are interesting in their own right.

5.2 Periodic orbits

The periodic orbits for several different wedge angles were found by the method described in Sec. (4.3). Several of these are illustrated in Fig. (5.1) for the wedge angle of $\phi = 60°$. The topology of the periodic orbits is of two types. The first type is the 'self–retracing' type which means that the orbit strikes either the tilted wall or the vertical wall at an angle of 90° and hence bounces directly back to retrace its

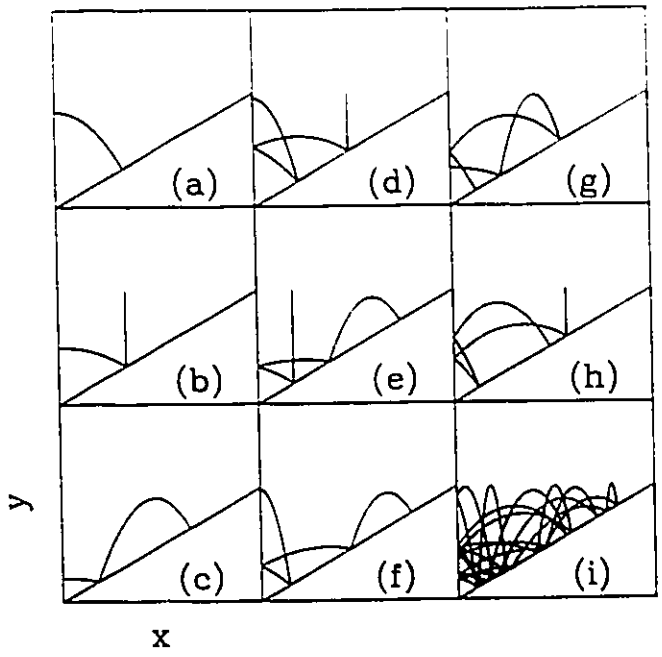

Figure 5.1: Some periodic orbits in the 60° wedge. All the periodic orbits up to word length 5 are shown in (a)-(h) and a typical long periodic orbit (of word length 15) is shown in (i). The words for the orbits are as follows: (a) V, (b) TV, (c) TTV, (d) TVVV, (e) TTVTV, (f) TTVVV, (g) TVVTV, (h) TVVVV, (i) TTTVTVTVVTVTTVVV.

path. Fig. (5.1a-h) are all illustrative of this type of orbit. The other type of orbit is the 'non-retracing' orbit. These orbits typically occur at longer word lengths and are distinguished by the fact that the orbit never reverses upon itself. Fig. (5.1i) is illustrative of a typical, rather long and complicated non-retracing orbit. As one can see, the periodic orbits can get quite involved.

The numerical procedure for finding the periodic orbits using the 2–dimensional Newton method outlined in Sec. (4.3) became unstable as the stability exponent of the periodic orbits increased. Generally this happened at word lengths of 16 or longer. Nonetheless, 1621 periodic orbits were found for the 60° wedge which corresponds to

word	S_γ	ν_γ	u_γ	σ_γ
V	1.33333	0.69315	5	-1
TV	2.30940	1.31696	8	-1
TTV	2.91043	1.84725	11	-1
TVV	3.26592	2.06344	13	1
TTTV	3.26605	2.29243	14	-1
TVVV	4.81335	2.70228	18	-1
TTVTV	5.11682	3.17631	19	1
TTVVV	5.17881	3.23281	21	-1
TTTVTV	5.33333	3.63689	22	1
TTTVVV	5.35747	3.67832	23	-1
TTTTVTV	5.44331	4.02503	25	1

Table 5.1: The word, S_γ, ν_γ, u_γ and σ_γ for the 10 shortest orbits (by action) in the wedge billiard for $\phi = 60°$. Note that the orbits TVV and $TTTV$ combine to form the vertex orbit (see the section on vertex orbits later on in this chapter). The data for TVV was calculated at $\phi = 59.999°$ and the data for $TTTV$ was calculated at $\phi = 60.001°$.

all periodic orbits with word length less than or equal to 15 and several hundred with word length of 16. Over 1048 periodic orbits were found for the 49° wedge, which corresponds to all periodic orbits with word length less than or equal to 19. In addition to these relatively short word length orbits many longer word length orbits were found corresponding to the non–isolated families we will discuss shortly.

Tables (5.3, 5.4) present the words of all the periodic orbits which actually exist in the 49° and 60° wedges respectively. Upon comparison with Tab. (4.1) one can see that many possible words are pruned. Furthermore, the pruning rules are not obvious. We suspect an infinity of pruning rules exist as the word length approaches infinity.

The stability exponents and actions for the periodic orbits were calculated

word	S_γ	ν_γ	u_γ	σ_γ
V	1.04323	0.48474	5	-1
TV	1.92931	0.94360	8	-1
TVV	2.59555	1.48123	13	1
TTVV	2.73807	1.96982	16	1
TVVV	3.91283	1.90729	18	-1
TTTVV	2.79379	2.39554	19	1
TVVVV	4.80835	2.42951	23	1
TTTTVV	2.82076	2.76202	22	1
TTTTTVV	2.83574	3.07970	25	1
TTTTTTVV	2.84489	3.35826	28	1

Table 5.2: The word, S_γ, ν_γ, u_γ and σ_γ for the 10 shortest orbits (by action) in the wedge billiard for $\phi = 49°$.

n	word	n	word	n	word	n	word
1	V	6	TTTTVV	7	TTVVTVV	8	TTTTVVVV
2	TV	6	TTVVVV	7	TTVVVVV	8	TTTVVTVV
3	TVV	6	TVTVVV	7	TVTVTVV	8	TTVVVVVV
4	TTVV	6	TVVVVV	7	TVVTVVV	8	TVTVTVVV
4	TVVV	7	TTTTTVV	7	TVVVVVV	8	TVVTVVVV
5	TTTVV	7	TTTVVVV	8	TTTTTTVV	8	TVVVVVVV
5	TVVVV						

Table 5.3: All periodic orbits found in the 49° wedge up to word length 8.

n	word	n	word	n	word	n	word
1	V	6	TTTVTV	7	TTVTVTV	8	TTTVTVTV
2	TV	6	TTTVVV	7	TTVTVVV	8	TTTVTVVV
3	TTV	6	TTVTVV	7	TTVVVVV	8	TTTVVVVV
3	TVV	6	TTVVVV	7	TVTVTVV	8	TTVTTVTV
4	TTTV	6	TVTVVV	7	TVTVVVV	8	TTVTTVVV
4	TVVV	6	TVVVVV	7	TVVTVVV	8	TTVTVTVV
5	TTVTV	7	TTTTVTV	7	TVVVVVV	8	TTVTVVTV
5	TTVVV	7	TTTTVVV	8	TTTTTVTV	8	TTVTVVVV
5	TVTVV	7	TTTVTTV	8	TTTTTVVV	8	TTVVVVVV
5	TVVVV	7	TTTVTVV	8	TTTTVTTV	8	TVTVTVVV
				8	TVTVVTVV	8	TVTVVVVV
				8	TVVTVVVV	8	TVVVVVVV

Table 5.4: All periodic orbits found in the 60° wedge up to word length 8. Note, the vertex orbit consists of the words TVV and $TTTV$.

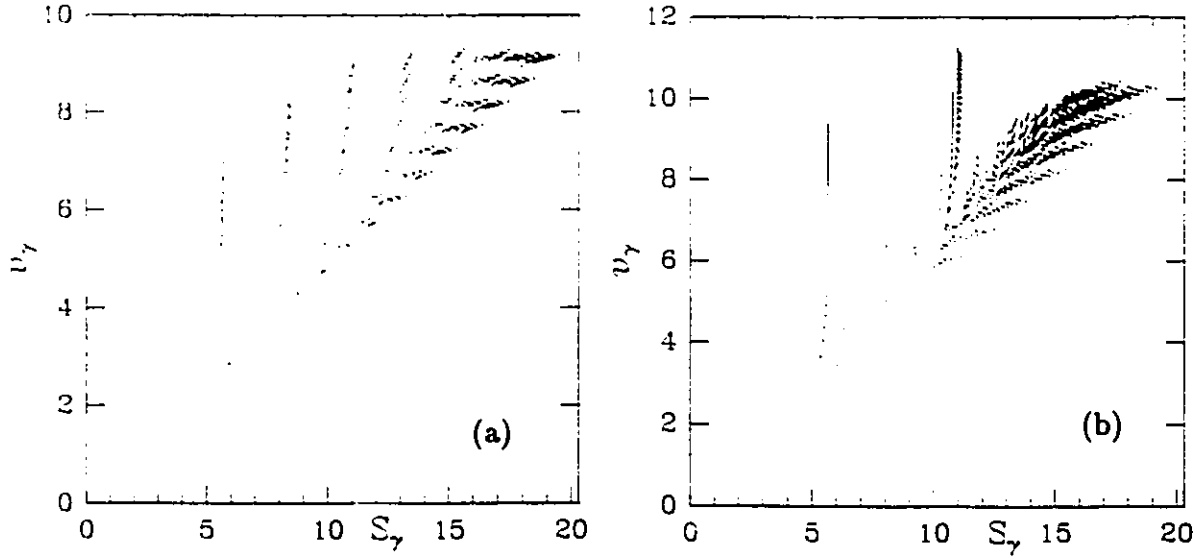

Figure 5.2: Plots of ν_γ vs. S_γ. In the left figure (a) 1048 periodic orbits for the 49° wedge are shown which corresponds to all periodic orbits with word lengths $\leq$ 19. In the right figure (b) 1920 periodic orbits for the 60° wedge are shown which corresponds to all periodic orbits with word lengths $\leq$ 15 and several hundred with longer word lengths.

according to the prescriptions given in Sec. (4.3.2) and Sec. (4.3.1). An interesting and informative display of this information is a plot of the stability exponent ν_γ vs. action S_γ. We show such plots in Figs. (5.2a,b) for the 49° and 60° wedges respectively. There is an interesting banded structure to these plots. The first set of bands corresponds to the orbits of same word length n. These bands are evident as horizontal clumps located along the main diagonal in Fig. (5.2a) and the slanted clumps located along the main diagonal in Fig. (5.2b).

5.2.1 Non–Isolated Periodic Orbits

Also evident are the vertical bands at $S_\gamma \approx 3, 5.5, 8.5, 11.5, 13, \ldots$ in Fig. (5.2a) and at $S_\gamma \approx 5.5, 11, \ldots$ in Fig. (5.2b). These vertical bands correspond to families of orbits which have successively longer word lengths and increasing stability exponents yet approach a finite limiting action (the accumulating action S_∞) as the word length tends to infinity. Similar families have been encountered in the 'stadium billiard' (R. Littlejohn, private communication) and in the 'Anisotropic Kepler Problem' (Gutzwiller 1990, Tanner and Wintgen 1992, Christiansen and Cvitanović 1992). The orbits are *non–isolated* (in the limit of word length approaching infinity) in the sense that in any phase space neighbourhood of S_∞ there are other periodic orbits with nearly the same action. The vertical band at $S_\gamma \approx 5.5$ in Fig (5.1b) corresponds the family characterized by words of the form $T^m VVV$, where m is a positive integer. This family is shown in Fig. (5.3). The $T^m VVV$ family corresponds to a series of bounces along the tilted wall followed by the velocity reversing sequence VVV. During the velocity reversing sequence the particle rises high up on the vertical wall in a very narrow parabolic arc. As more T bounces are added the bounces along the tilted wall become shallower and shallower, and the starting point for the orbit moves closer to the point $x = 1/cot(\phi), y = 1$. In the limit of $m \to \infty$ the particle slides down the tilted wall, rises vertically at $x = 0$ to $y = 1$, falls back down and slides back up the tilted wall. The limiting action for such an orbit is $S_{m\to\infty} = 2^{5/2}$. Listed in Table

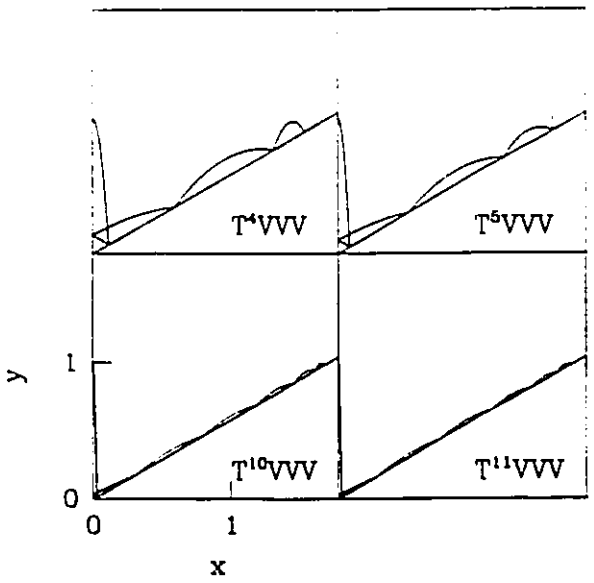

Figure 5.3: The family characterized by words of the form T^mVVV in the 60° wedge. In the left two figures (m even) the orbit ends its travels high upon the tilted wall in a parabolic bounce. In the right two figures (m odd) the orbit ends its travels high upon the tilted wall with a vertical bounce.

(5.5) are m, S_γ, ν_γ, u_γ, and σ_γ for the members of this family. Note that all members of this family have $\sigma_\gamma = -1$ and thus are hyperbolic with inversion. Also, on average, u_γ increases by 3 for each additional T bounce. A plot of $\ln(\nu_m)$ vs. $\ln m$ for this family reveals that $\nu(m) \approx m^{0.2215}$, and as such $\lim_{m\to\infty} \nu(m) = \infty$.

Another family, which is a component of the vertical band occurring at $S_\gamma \approx 5.5$ in the 49° wedge, is shown in Fig. (5.4). This family is characterized by words of the form $T^mVVTTVV$. This family approaches the limiting action $S_{m\to\infty} \approx 5.635$ and the stability exponent again scales as a power of m, $\nu(m) \approx m^{0.077}$, indicating that $\lim_{m\to\infty} \nu(m) = \infty$. Listed in Table (5.5) are m, S_γ, ν_γ, u_γ, and σ_γ for the members of this family. Note that all members of this family have $\sigma_\gamma = 1$ and. Also,

m	S_γ	ν_γ	u_γ	σ_γ
1	4.81335	2.70228	18	-1
2	5.17881	3.23281	21	-1
3	5.35747	3.67832	23	-1
4	5.45431	4.05543	26	-1
5	5.51162	4.37939	29	-1
6	5.54799	4.66194	32	-1
7	5.57239	4.91174	35	-1
8	5.58949	5.13521	38	-1
9	5.60192	5.33715	41	-1
10	5.61123	5.52119	44	-1
11	5.61837	5.69017	47	-1
12	5.62396	5.84630	50	-1
13	5.62843	5.99136	53	-1
14	5.63204	6.12679	57	-1
15	5.63501	6.25377	59	-1
16	5.63748	6.37327	62	-1
17	5.63955	6.48612	65	-1
18	5.64131	6.59301	69	-1
19	5.64282	6.69454	72	-1
20	5.64411	6.79120	74	-1
21	5.64524	6.88344	77	-1
22	5.64622	6.97165	80	-1
23	5.64708	7.05616	83	-1
24	5.64785	7.13727	86	-1
25	5.64852	7.21523	89	-1
26	5.64913	7.29028	92	-1
27	5.64967	7.36264	95	-1
28	5.65015	7.43248	98	-1
29	5.65059	7.49997	101	-1
30	5.65099	7.56527	104	-1
31	5.65135	7.62851	107	-1
∞	5.65685	∞	∞	-1

Table 5.5: The family T^mVVV in the 60° wedge.

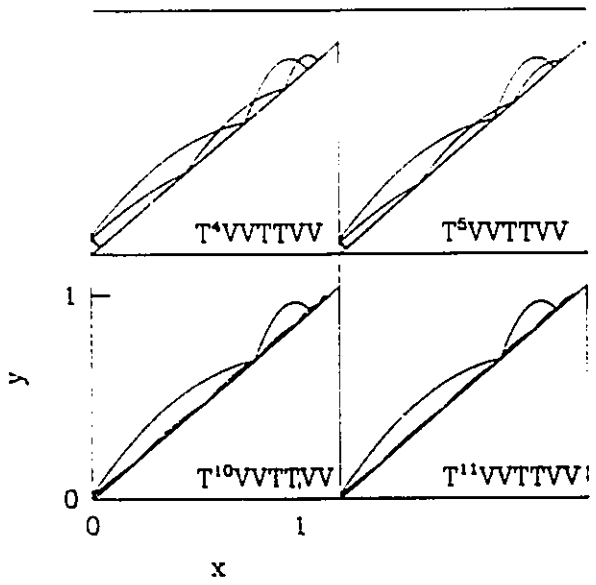

Figure 5.4: The family characterized by words of the form $T^mVVTTVV$ in the 49° wedge. In the left two figures (m even) the orbit ends its travels high upon the tilted wall in a parabolic bounce. In the right two figures (m odd) the orbit ends its travels high upon the tilted wall with a vertical bounce.

as before in the case of the T^mVVV family in the 60° wedge, on average u_γ increases by 3 for each additional T bounce.

5.3 Maslov Indices

The calculation of Maslov indices, as outlined in Sec. (4.3.3), is illustrated quite well by the periodic orbit TV shown in Fig. (5.5). The angle the chosen branch of the unstable manifold makes with the q_2 axis is labelled by θ. Hence $\theta = 0°$ in the figure corresponds to the chosen branch of the unstable manifold lying along the q_2 axis and $\theta = 90°$ corresponds to the chosen branch of the unstable manifold lying along the p_2 axis. I have chosen the fundamental domain of the angle of the unstable

m	S_γ	ν_γ	u_γ	σ_γ
3	5.53595	4.36452	35	1
4	5.56836	4.72983	38	1
5	5.58756	5.04659	41	1
6	5.59976	5.32448	44	1
7	5.60795	5.57112	47	1
8	5.61370	5.79235	50	1
9	5.61787	5.99265	53	1
10	5.62100	6.17546	56	1
11	5.62340	6.34349	59	1
12	5.62529	6.49887	62	1
13	5.62679	6.64334	65	1
14	5.62800	6.77829	68	1
15	5.62900	6.90487	71	1
16	5.62983	7.02404	74	1
17	5.63053	7.13661	77	1
18	5.63112	7.24327	80	1
19	5.63163	7.34459	83	1
20	5.63207	7.44108	86	1
21	5.63245	7.53317	89	1
22	5.63278	7.62125	92	1
23	5.63307	7.70564	95	1
24	5.63332	7.78664	98	1
25	5.63355	7.86452	101	1
26	5.63375	7.93949	104	1
27	5.63394	8.01177	107	1
28	5.63410	8.08154	110	1
29	5.63425	8.14898	113	1
30	5.63438	8.21422	116	1
31	5.63450	8.27742	119	1

Table 5.6: The family $T^m VVTTVV$ in the 49° wedge.

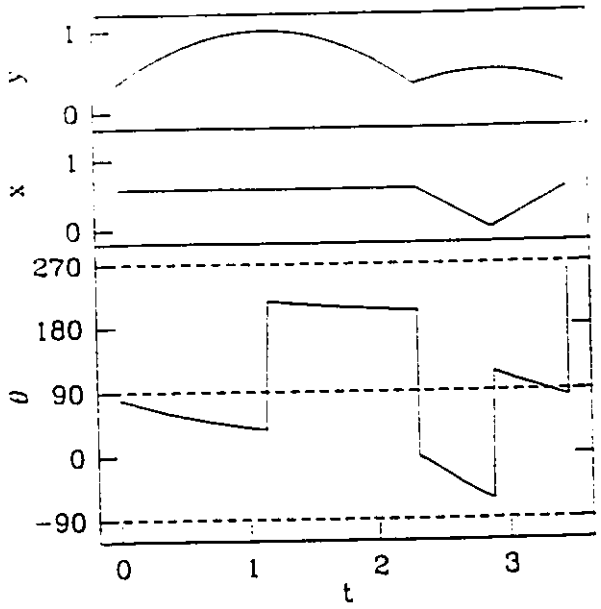

Figure 5.5: A plot of the TV orbit in the 60° wedge as a function of time t (see also Fig. (5.1b). In the upper two boxes the y and x positions of the particle are plotted as functions of time. The orientation of the unstable manifold, θ, as the orbit is traversed, is shown in the lower box as a solid line. The angles $\theta = -90, 90, 270$ are marked as horizontal dashed lines.

manifold as $-90 \leq \theta \leq 270$. The trajectory starts out moving directly upwards at $x \approx 0.55, y \approx 0.34$. The unstable manifold starts off at an angle of $\approx 80°$ and decreases as the trajectory climbs. As the trajectory reaches the top of its vertical climb at about $t = 1.1$ the trajectory 'falls' back upon itself and $(p_x = 0, p_y = 0)$. We add 1 to the Maslov index. Also, the unstable manifold 'flips' its orientation and we add 180° to its θ (we could have equally well subtracted 180°). The angle of the unstable manifold continues to decrease until the collision with the tilted wall at $t \approx 2.25$. We add 2 to the Maslov index due to this collision. Also the angle of the unstable manifold changes discontinuously with the collision and ends up at about $\theta = -20°$. The angle decreases again as the trajectory heads toward the

vertical wall and again changes discontinuously with the collision with the vertical wall (at $t \approx 2.9$) up to $\theta = 110°$. It then decreases again, finally passing through the vertical (at $\theta = 90°$) while rotating clockwise at $t \approx 3.33$. This adds 1 to the Maslov index. Finally, just before returning to the start of the trajectory the impact with the tilted wall at $t \approx 3.463$ causes another discontinuous change in the angle of the unstable manifold. It ends up 180° away from its original orientation. We add 2 to the Maslov index on account of this hard wall collision. Thus, the total Maslov index is $u_{TV} = 1+2+2+1+2 = 8$. Also, since the unstable manifold ends up 180° away from its original orientation this orbit is hyperbolic with reflection. This is also reflected in the eigenvalues of the monodromy matrices, which come out negative.

In a physical Hamiltonian system the angle θ must always *decrease* with time (Creagh et. al. 1990). This is confirmed by the constant clockwise rotations of the unstable manifold seen in our numerical investigations.

One thing to note about this trajectory is that the Maslov index u_{TV} is even and the orbit is hyperbolic with reflection. This situation is quite common in the wedge billiard if there are an odd number of collisions with the walls. This is a consequence of the discontinuous nature of the changes in orientation of the orbit upon collisions with the hard walls. The statement made by Creagh et. al. that '*Finally, we note that u is odd if and only if the orbit is hyperbolic with reflection.*' should perhaps be qualified with the phrase '*Finally, we note that, for smooth potentials, u is odd....*' since for billiard systems the original statement is not true.

Related to the Maslov index are the focussing properties of the periodic orbit. If a pencil of trajectories is started out at a certain point on the periodic orbit (in the jargon of chapter 3, q_1 =starting point, $(\delta q_2 = 0, \delta p_2 \neq 0)$) then in general this pencil of trajectories will spread out for a while (as q_1 increases) and we will end up with some $(\delta q_2', \delta p_2')$. However, later on the pencil of trajectories may refocus, either to a point focus or along a 'caustic surface' (Shulman 1981, Creagh et. al. 1990). This situation is signalled by

$$\frac{\partial q_2'}{\partial p_2} = 0 \tag{5.1}$$

which means that one can vary the initial perpendicular momentum and it makes no difference in the final perpendicular position. Since $p_2 = \partial S/\partial q_2$ Eq. (5.1) is equivalent to

$$\frac{\partial^2 S}{\partial q_2 \partial q_2'} = \pm\infty. \tag{5.2}$$

To find the Maslov index the number of these focal points and caustics is counted as the trajectory is traversed. The Maslov index is incremented by one for each focal point or caustic encountered as the orbit is traversed, by one for each time the particle stops ($p_x = p_y = 0$) and by two for each hard wall collision. Also the sign of

$$\delta^2 S = \frac{\partial^2 S}{\partial q_2 \partial q_2} + 2\frac{\partial^2 S}{\partial q_2 \partial q_2'} + \frac{\partial^2 S}{\partial q_2' \partial q_2'} \tag{5.3}$$

is noted at the end of the trajectory and the Maslov index is incremented by one if

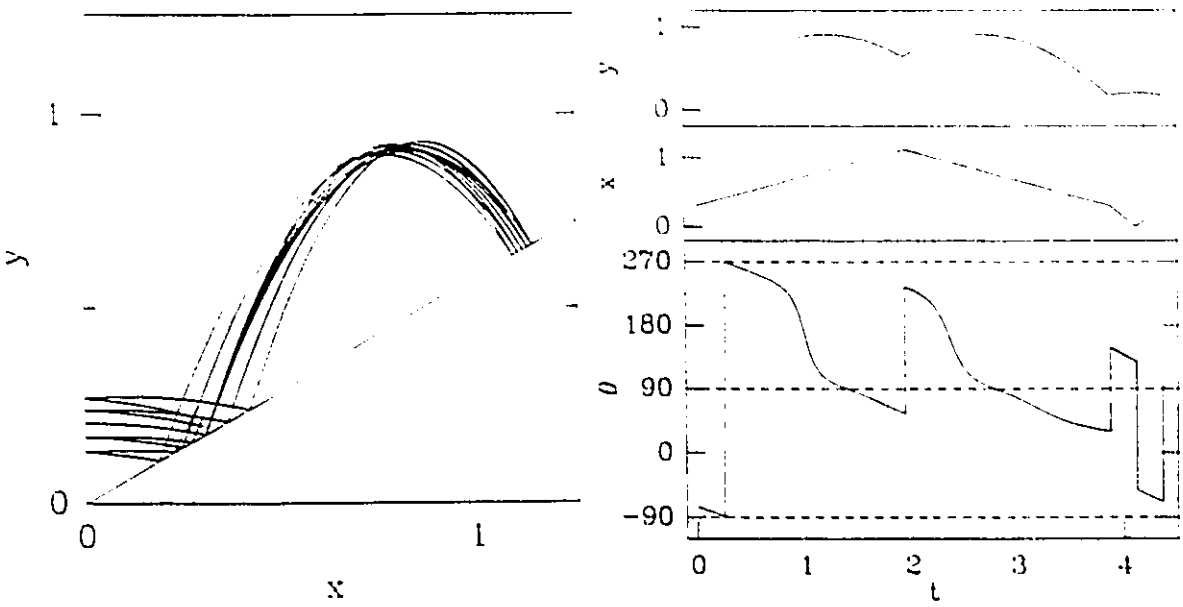

Figure 5.6: (left) The orbit TTV. A pencil of trajectories starting out low along the tilted wall and shot up at about an 80° angle from the horizontal. All trajectories shown are followed for the same length of time. (right) x, y, and the angle of the unstable manifold as a function of time.

$\delta^2 S < 0$. ($\delta^2 S$ arises in the derivation of the Gutzwiller trace formula (Gutzwiller 1971) and is also important in determining whether periodic orbits are isolated or not (Gutzwiller 1990)). This method of determining the Maslov index is very close in spirit to that originally proposed by Gutzwiller (1971).

We illustrate this method in Figs. (5.6,5.7). In Fig. (5.6) the initial pencil of trajectories spreads out as it rises but they refocus to a point focus just to the right of the maximum. The trajectories then bounce off the tilted wall and create a caustic surface as they pass the maximum travelling towards the left. They strike the tilted wall and the vertical wall and there are no more caustics or foci before they return to the starting point. Also, after one traversal of the orbit $\Delta^2 S = -4.3 < 0$.

In Fig. (5.7) the initial pencil of trajectories spreads out as it leaves the starting point travelling left high on the tilted wall. They then refocus to a point

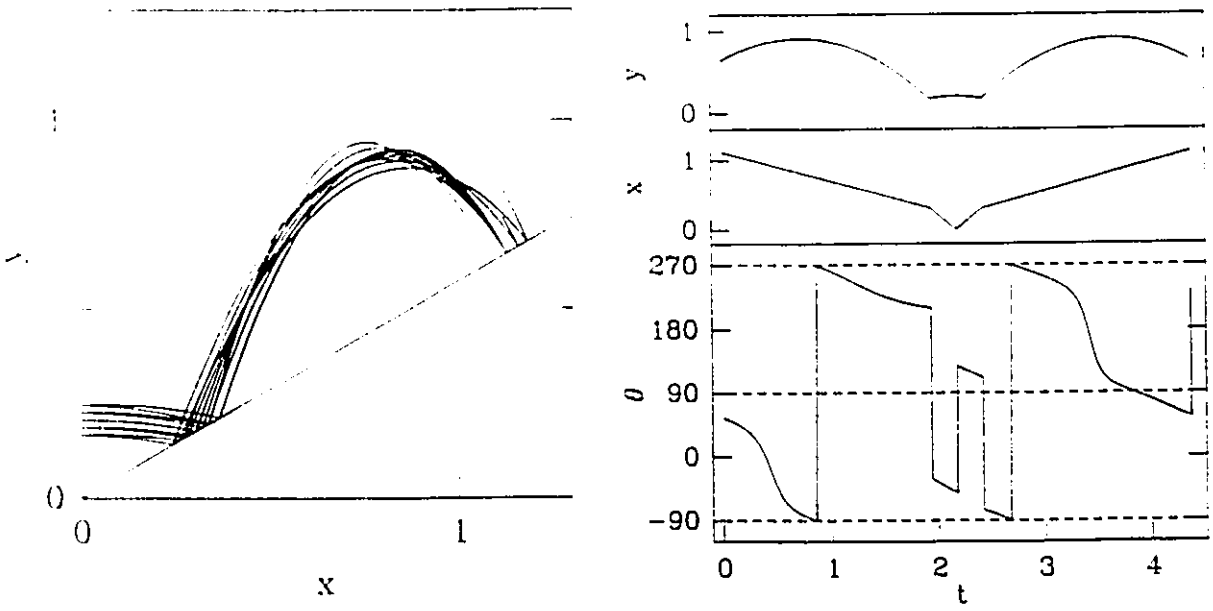

Figure 5.7: (left) The orbit TTV. A pencil of trajectories starting out high along the tilted wall and shot up at about a 120° angle from the horizontal. All trajectories shown are followed for the same length of time. (right) x, y, and the angle of the unstable manifold as a function of time.

focus just to the left of the maximum. The trajectories then diverge again and strike the tilted wall and the vertical wall. Just after striking the tilted wall for the second time there is another point focus and just to the right of the maximum, shortly before the orbit returns to its starting point, there is a caustic surface. After this final caustic there are no more foci or caustic surfaces. Also, after one traversal of the orbit $\Delta^2 S = 3.9 > 0$.

Using either figure we calculate that the Maslov index is 8 as we found before. It is interesting to note that depending on where one starts on the periodic orbit the number of caustics and foci encountered as the orbit is traversed can change. In Fig. (5.6) there is one caustic surface and one point focus. In Fig. (5.7) there is one caustic surface and two point foci. However, the sign of $\Delta^2 S$ is different for the two different starting points and so the total Maslov index is the same for both orbits. A

similar situation was found for periodic orbits in the stadium billiard by Creagh et. al. (1990).

5.4 Scaling properties

Keeping in mind the application of cycle expansions (see Sec. (3.2.4)) in the periodic orbit theory we examine the scaling properties of the periodic orbits. Also, the scaling properties will give us important information about the convergence of the Gutzwiller trace formula (and its re-arrangements) as we will see in chapter 6.

One pre–requisite for the cycle expansions to work is that the actions of orbits be 'additive', i.e. $S_{TTVV} \approx S_{TTV} + S_V$. Similarly the stability exponents and Maslov indices must be additive. We plot the average action $\bar{S}$, stability exponent $\bar{\nu}$ and Maslov index $\bar{u}$ is as a function of word length n in Figs. (5.8,5.9,5.10) respectively. Good linear relationships are seen in all the figures indicating that these quantities are indeed, on average, additive. We see from Fig. (5.9) that the 60° wedge is the most chaotic in the sense that the periodic orbits have, on average, larger stability exponents than at any other angle. (We have investigated the behaviour of $\bar{\nu}(n)$ vs. n for wedge angles $60° < \phi < 90°$ and have found that again, 60° is maximally chaotic). This is in agreement with Lehtihet and Miller (1986) and Whelan et. al. (1990) who found that 60° corresponded to the most chaotic behaviour.

Also of interest is the distribution of actions about the average for a constant

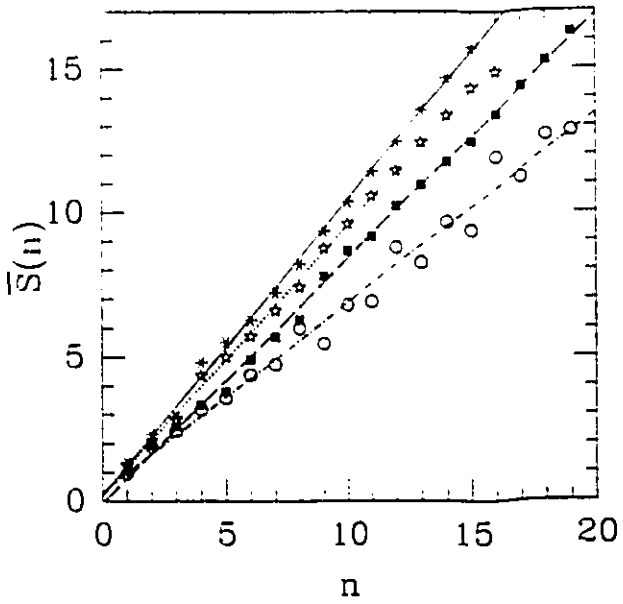

Figure 5.8: The average action $\bar{S}(n)$ plotted as a function of word length n for several different wedge angles. The solid line corresponds to $\phi = 60°$ (slope=1.026), the short dashed line corresponds to $\phi = 55°$ (slope=0.932), the long dashed line corresponds to $\phi = 49°$ (slope=0.847), and the alternating short dash, long dash line corresponds to $\phi = 46°$ (slope=0.657).

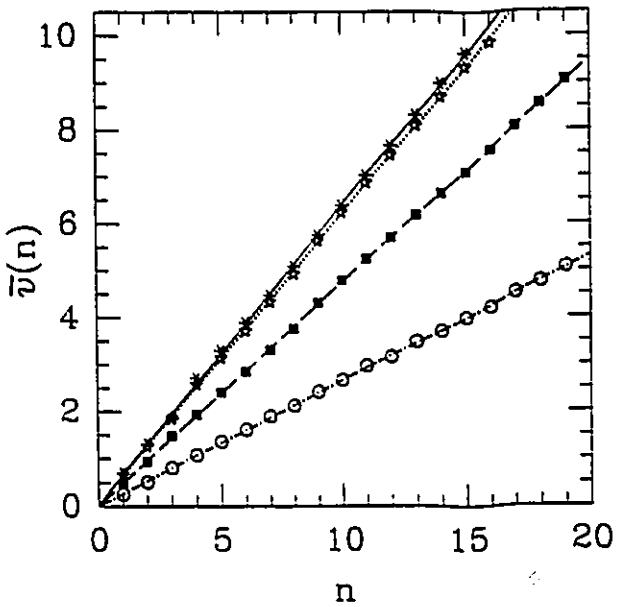

Figure 5.9: The average stability exponent $\bar{\nu}(n)$ as a function of word length n. The legend for the lines is the same as that used in Fig. (5.5). The slopes of the lines are 0.635, 0.618, 0.474, and 0.265 for the 60°, 55°, 49° and 46° lines respectively.

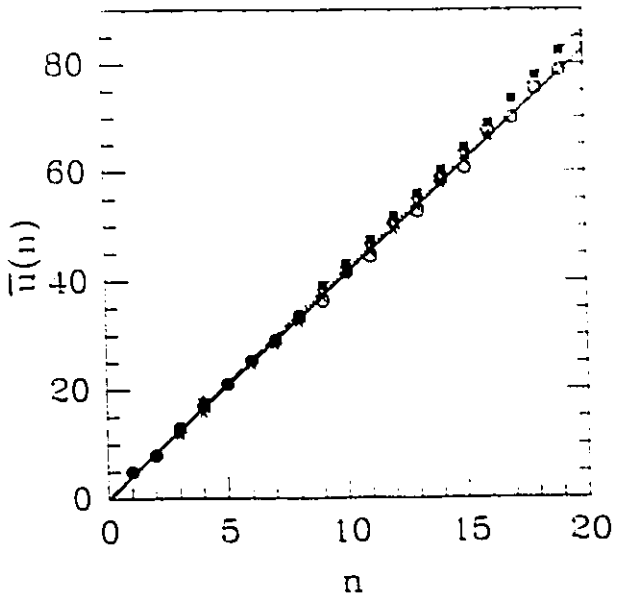

Figure 5.10: The average maslov index $\bar{u}(n)$ as a function of word length n. The legend for the lines is the same as that used in Fig. (5.8). The slopes of the lines are 4.129, 4.187, 4.333, and 4.123 for the 60°, 55°, 49° and 46° lines respectively.

word length n. Fig. (5.11) is a histogram plot of such a distribution. One can see that a gaussian gives a reasonable fit to the histogram, however some notable 'outliers' are evident, such as the orbits at $S \approx 5.5$ and $S \approx 10.5$. These outliers are evidence of the non–isolated families of periodic orbits mentioned earlier. It is also interesting that as the word length is varied the shape of the $N(S)$ vs. S plots remains the same. This means that the distribution of actions about the mean remains about the same for different word lengths. By appropriately scaling the actions and amplitudes of the plots we can see this very clearly. We define the scaled probability $P_n(S_n^{scaled})$ that an orbit of word length n will have scaled action $S_n^{scaled} = S_n/\bar{S}_n$ between S_n^{scaled} and $S_n^{scaled} + \delta S_n^{scaled}$ as

$$P_n(S_n^{scaled}) = \frac{N(S_n^{scaled})}{N_n^{Total}} \frac{1}{\delta S_n^{scaled}} \tag{5.4}$$

where N_n^{Total} are the total number of orbits at word length n. Fig. (5.12) shows a

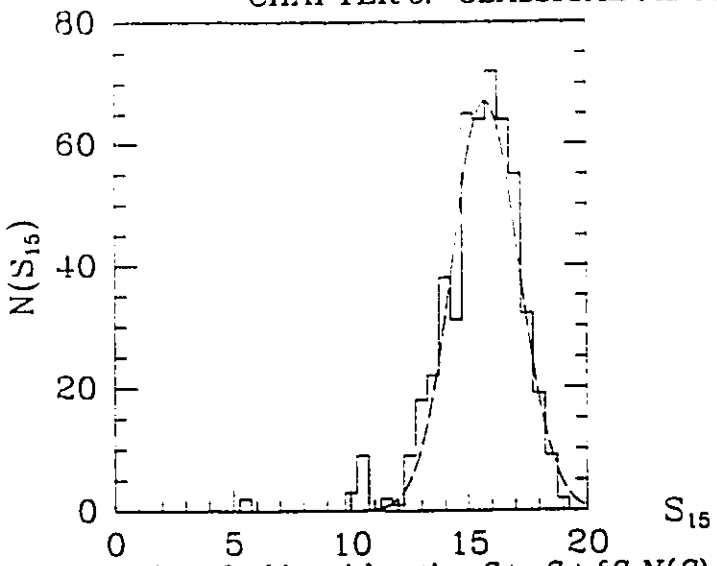

Figure 5.11: The number of orbits with action S to $S+\delta S$ $N(S)$ plotted as a function of S for word length 15 and $\phi = 60$. δS is the bin size (0.5 in this case). The 'best fit' gaussian (dashed line) is characterized by $N(S) = 67\exp(-0.25(S-\bar{S_{15}})^2)$ where $\bar{S_{15}} = 15.74$.

plot of $P_n(S_n^{scaled})$ vs. n for two different wedge angles, $\phi = 60°$ and $\phi = 49°$. Notice that although the shapes of the distributions is very different for the two different wedge angles the distributions at constant wedge angle show remarkable similiarities as the word length is changed.

Another scaling property which is of interest in chaotic systems is the topological entropy τ (Gutzwiller 1990, Aurich and Steiner 1988, Sieber and Steiner 1990b). In some chaotic systems the number of periodic orbits N which have action less than a certain action S is expected to grow asymptotically as

$$\lim_{S\to\infty} N(S) \approx \frac{\exp(\tau S)}{\tau S}. \tag{5.5}$$

However, because of the existence of families of non-isolated orbits discussed in Sec.

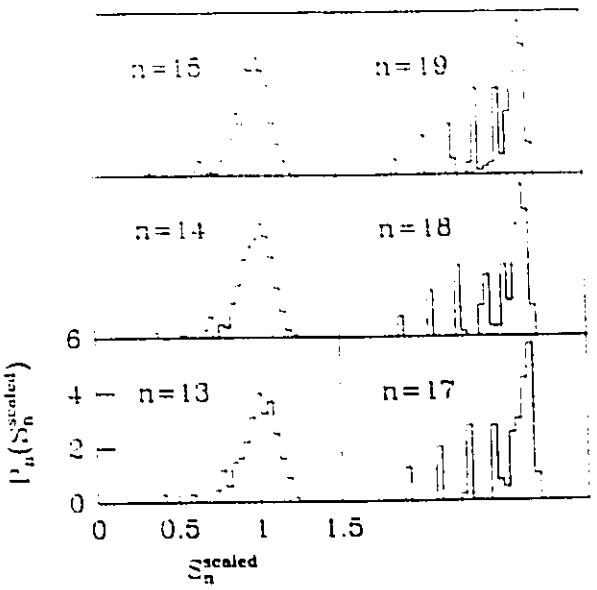

Figure 5.12: A histogram plot of $P_n(S_n^{scaled})$ vs. n for two different wedge angles. The left hand column contains histograms for $\phi = 60°$ and the right hand column contains histograms for $\phi = 49°$. The word length n is shown in the upper left hand corner of each plot.

(5.2) there are an infinity of orbits with action less than S if S is larger than the accumulating action for the first family of non–isolated orbits. Thus, the topological entropy is not a good quantity to use in the characterization of the periodic orbits appearing in this system.

We define a related concept, the *word length entropy*, τ_w. It is reasonable to expect, on the basis of Eq. (5.5), that the number of periodic orbits N with word length less than or equal to n grows as

$$N(n) \approx \exp \tau_w n. \tag{5.6}$$

In the absence of pruning we expect every possible n letter word to correspond to a periodic orbit. This is called *complete binary dynamics*. However, with pruning

not all words correspond to physical periodic orbits, and the number of actual orbits found is less than for complete binary dynamics. We show in Fig. (5.13) plots of $\ln N(n)$ vs. n for several different wedge angles and for complete binary dynamics. Excellent linear relationships are seen at each angle and for the complete binary dynamics, thus confirming the validity of Eq. (5.6). τ_c is given by the slopes of these lines. It is notable that for all wedge angles in Fig (5.13) τ_c is significantly less τ_c for complete binary dynamics. This indicates that the pruning of the dynamics in the wedge billiard is quite severe. The pruning increases as the wedge angle approaches 45° (and 90° although this case was not shown). That the pruning increases near the integrable cases of $\phi = 90°$ and $\phi = 45°$ is to be expected since in the case of integrable systems the number of periodic orbits with action less than S grows only as a power law (Gutzwiller 1990), instead of an exponential as in Eq. (5.5).

The Gutzwiller trace formula relies, in some sense, on the periodic orbits and their phase space neighbourhoods to give an accurate description of the entire phase space of the wedge billiard. The periodic orbits form the 'skeleton' of the phase space. Do the periodic orbits give an accurate description when only a finite number of them are used? How good is this description in the case of the wedge billiard? In an attempt to shed some light on these questions we have plotted a surface of section in Fig. (5.14) for the 1920 periodic orbits shown in Fig. (5.2b) for the 60° wedge. This surface of corresponds to the p_y vs. y plane, $p_x > 0$, just after a collision with the tilted wall. Plotted in Fig. (5.15) is a surface of section for a typical (non-

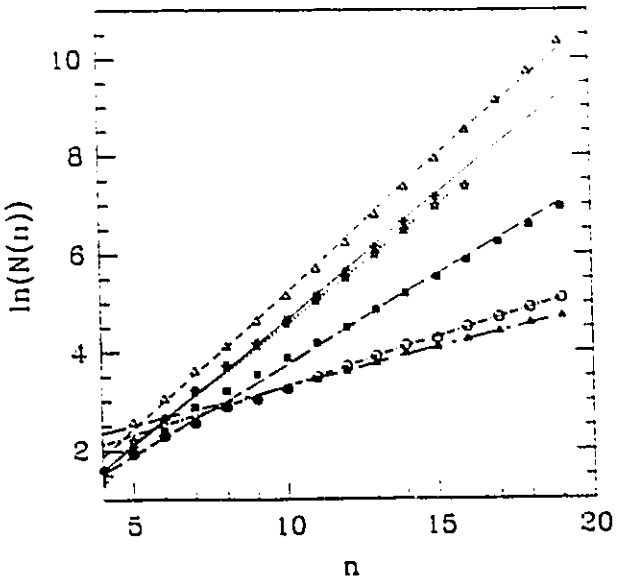

Figure 5.13: Plots of $\ln N(n)$ vs. n for several different wedge angles. The legend is the same as that for Fig. (5.8), except for the line which has the shallowest slope (which corresponds to $\phi = 45.5°$) and the line which has the steepest slope (which corresponds to complete binary dynamics). The slopes of the lines are 0.496, 0.471, 0.341, 0.211 and 0.180 for the 60°, 55°, 49°, 46° and 45.5° lines respectively.

periodic) trajectory, followed for the same number of intersections. It can be seen, upon comparing the figures, that the periodic orbits do form a sort of framework interleaved with the non–periodic trajectories in phase space. However there are some notable gaps where there are few periodic orbits. One such gap occurs at the bottom of Fig. (5.14) near the energy boundary. Orbits in this area correspond to orbits which glance along the tilted wall at a very shallow angle. Indeed, most points in this area belong to the non–isolated families of orbits discussed earlier, which have just this property. Presumably, as longer word lengths were investigated this region would fill in. Other gaps are harder to explain. Nonetheless, they too are expected to fill in as longer word lengths are investigated. Other structures, such as the almost

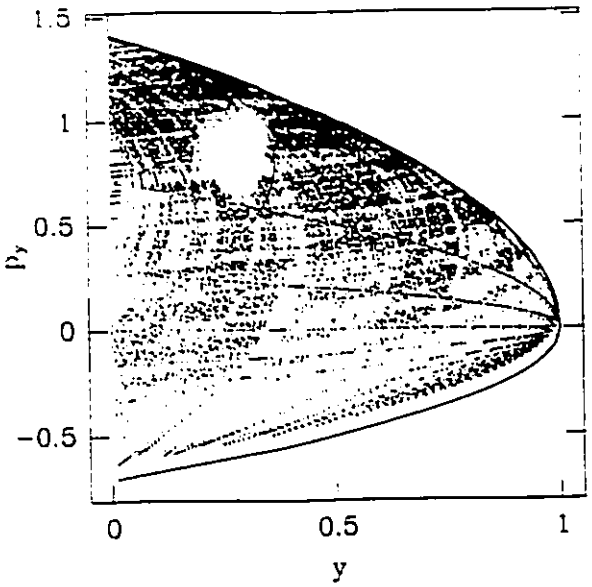

Figure 5.14: A p_y vs. y, $p_x > 0$, surface of section taken just after a collision with the tilted wall. 37903 intersections are shown, which corresponds to 1920 periodic orbits in the 60° wedge. The solid outer curve is the energy boundary given by energy conservation.

horizontal lines formed by the periodic orbits, can sometimes be attributed to orbits which retrace themselves and strike either the vertical or tilted wall at 90°.

A commonly used measure which characterizes the chaotic nature of the phase space is the Lyapunov exponent λ (Pars 1965, Green and Kim 1987, Lorenz 1984, Bennettin et. al. 1980). The Lyapunov exponent measures the average rate of spreading of trajectories in phase space, followed for long periods of time. We can define a mean Lyapunov exponent $\bar{\lambda}$ using the stability exponents calculated for the periodic orbits by

$$\bar{\lambda} = \frac{1}{N} \sum_{\gamma}^{N} \frac{\nu_\gamma}{T_\gamma(1)} \tag{5.7}$$

where N is the total number of periodic orbits summed over. Using 1621 periodic

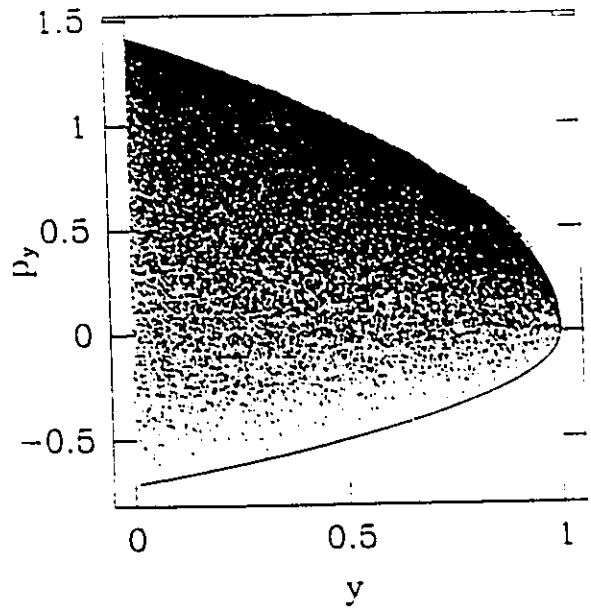

Figure 5.15: A p_y vs. y, $p_x > 0$, surface of section taken just after a collision with the tilted wall. This non-periodic trajectory is typical of ones which occur in the 60° wedge. The solid outer curve is the energy boundary given by energy conservation.

orbits we find $\bar{\lambda} = 0.425$. This is to be compared to $\lambda = 0.417$ calculated by following a typical non-periodic trajectory for a very long time. The agreement between these values is very good.

From Figs. (5.14,5.15) we see that the periodic orbits do form a 'skeleton' of the phase space for the wedge billiard, and from $\bar{\lambda}$ we see that they even describe average quanititative features of the phase space quite well. Hence we are reasonably confident that the finite number of periodic orbits we have found does give a reasonable characterization of the phase space of the wedge billiard.

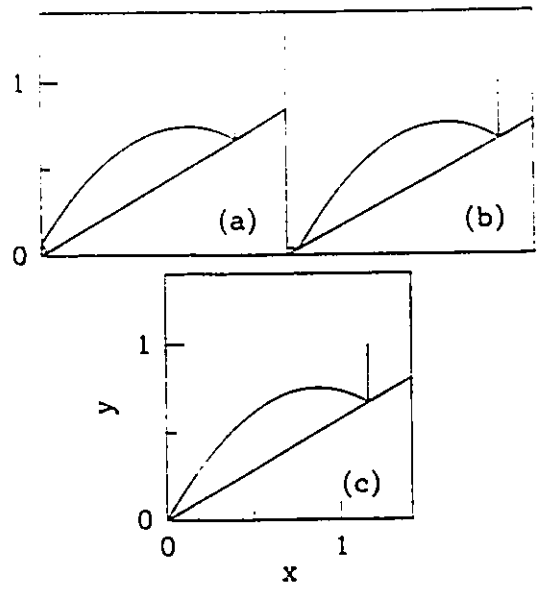

Figure 5.16: (a). The orbit TVV in the 59° wedge. (b) The orbit $TTTV$ in the 61° wedge. (c) The vertex orbit in the 60° wedge.

5.4.1 Vertex Orbits

We argued in Sec. (4.3) that periodic orbits which entered the wedge vertex (those whose word contained a B) had infinite stability exponents and did not contribute to the Gutzwiller trace formula. There is one known exception to this rule, pointed out to us by U. Smilansky. At wedge angle 60° the phase space of the orbit which goes directly into the wedge vertex at an angle of 30° to the vertical stays connected and neighbouring trajectories do not diverge macroscopically from the vertex trajectory. This orbit is the limiting case of the orbit TVV (which exists for $\phi < 60°$) and the orbit $TTTV$ (which exists for $\phi > 60°$). As the wedge angle approaches 60° these two orbits become the same and describe this vertex orbit. We show the TVV, $TTTV$ and vertex orbits in Fig (5.16). It is interesting to note that u_γ, σ_γ and ν_γ are different

for the two orbits TVV and $TTTV$ as $o \to 60°$ as can be seen from Table (5.1). This means that the properties of trajectories deviating from the vertex orbit in one direction (positive δq_2 say) are different than those in the other direction (negative δq_2 say). The vertex orbit is in a sense an *average* of the properties of the two limiting orbits. The sense in which we mean *average* will become clearer in the chapter 6.

Chapter 6

Quantum Results

6.1 Numerical Solution of the Schrödinger equation: Results

We present here the results of the numerical calculations outlined in Sec. (4.2).

With the guidelines outlined in Sec. (4.2) we chose to use $l_{max} = m_{max} = 65$ and $\rho_o = 31.5$ for the diagonalization of a 45° wedge. Using the arguments given in Sec. (4.2) this should give us $N \approx 290$ eigenvalues accurately. We may analytically calculate the energy eigenvalues of the 45° wedge for small quantum numbers n_1, n_2 using Eqs. (2.20, 2.49), and in the limit of large n_1 and n_2 by using using Eq. (2.52). We then compare the analytical values with the eigenvalues from the matrix diagonalization. If E_i^{matrix} and E_i^{EBK} are the i^{th} energy eigenvalues from the matrix diagonalization and EBK solution respectively then the relative difference R_i

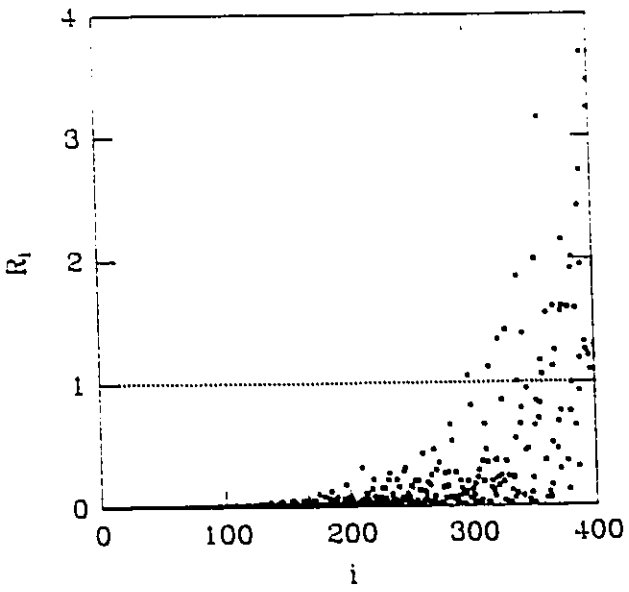

Figure 6.1: The relative difference between the i^{th} energy eigenvalue from the matrix diagonalization, E_i^{matrix}, and the i^{th} energy eigenvalue calculated analytically, E_i^{EBK}, normalized to the average level spacing (see text) plotted as a function of eigenvalue number i. The E_i^{EBK} were generated using the Airy zeroes and Eqs. (2.20, 2.49) for quantum number $n \leq 9$ and using Eq. (2.52) for $n > 9$.

is defined as

$$R_i = |E_i^{matrix} - E_i^{EBK}|d(E)$$

where $d(E) = dN(E)/dE$ is the density of states, $d(E_i) \approx E_i^2/(4\pi \cot \phi)$ (from Eq. (B.20). Fig (6.1) shows such a comparison. In this figure we have plotted the relative difference R_i vs. eigenvalue number i where the relative difference for each pair is drawn as a square. A horizontal dotted line is drawn at $R_i = 1$. When the relative difference approaches 1 the error in the eigenvalues computed from the matrix diagonalization becomes comparable to the level spacing and hence the eigenvalues

are inaccurate. The first time this occurs is near eigenvalue 300. Even before this however, the situation becomes quite unacceptable past about eigenvalue 250. Past eigenvalue 250 many of the computed eigenvalues have a relatively large error ($\approx 30\%$ of the average level spacing) compared to the exact eigenvalues. Hence our above estimate of finding $N \approx 290$ eigenvalues for $l_{max} = m_{max} = 65$ and $\rho_o = 31.5$ is quite reasonable. However we must keep in mind that the last 20% or so of the eigenvalues will not be very accurate, as can be seen from the steady rise of points in Fig (6.1) past eigenvalue 250.

Using the guidelines outlined in Sec. (4.2) we find that if we want to have $\approx$300 eigenvalues accurately calculated for a 49° wedge then $E_{300} \approx 21.43$ and $\rho_o \approx 32.65$. For $E_{300} \approx 21.43$ we find $l_{max} \approx 68$.

Similarly, for a 60° wedge we find that if we want $\approx$200 eigenvalues then $N \approx 200$, $E_{200} \approx 18.5$, $\rho_o \approx 37$ and $l_{max} \approx 72$.

For our numerical diagonalizations of both the 49° and 60° wedge we have chosen $\rho_o = 32.9$ and $l_{max} = m_{max} = 70$. The resulting 4900×4900 matrices were diagonalized on the Ontario Centre for Large Scale Computation Cray X-Mp. Each diagonalization took about 1.25 hours. In addition to the 4900 eigenvalues 300 eigenvectors were also obtained.

Another check (M. Sieber, 1991) on the accuracy of the eigenvalues is given by comparing the calculated quantum staircase to the smooth Thomas–Fermi approximation given by Eq. (3.32). Such a comparison is given in Figs. (6.2, 6.3) for the

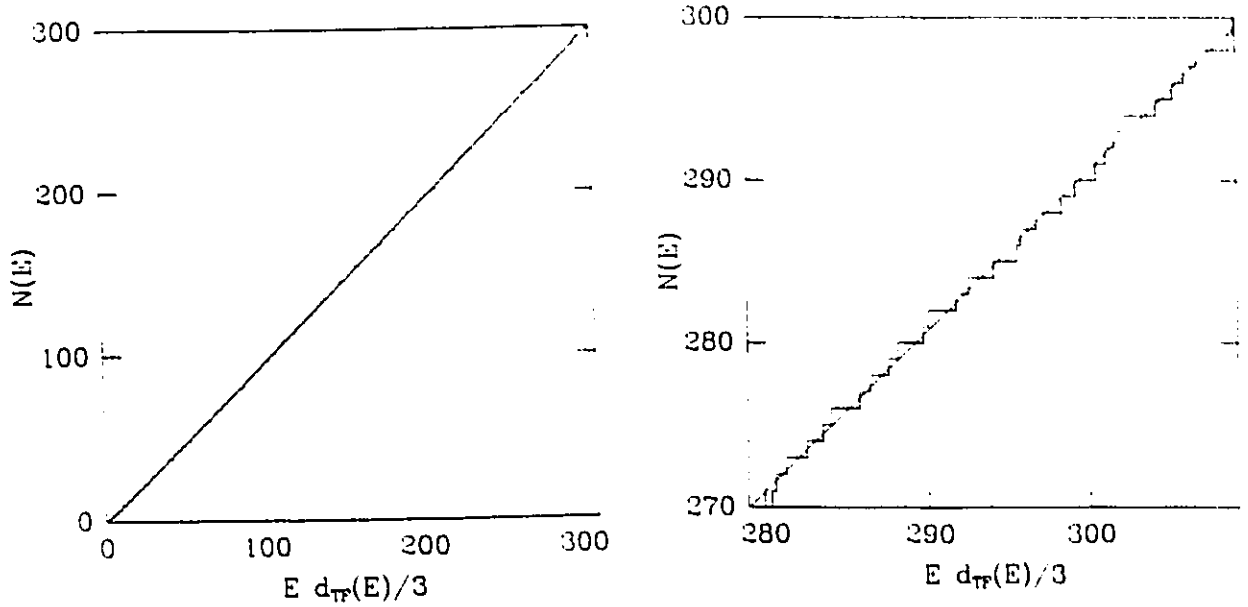

Figure 6.2: The Thomas–Fermi staircase (smooth curve) plotted along with the exact quantum staircase for the first 300 eigenvalues in the 49° wedge. On the scale shown in the left figure the two curves are virtually indistinguishable. An expanded scale plot of the region near $N(E) = 300$ is shown in the right figure.

49° and 60° wedge respectively. On average, the Thomas–Fermi curve cuts through the exact quantum staircase at half integral values of $N(E)$. The excellent agreement between the two curves shown in Figs. (6.2,6.3) is evidence that no eigenvalues have been missed by the numerical calculations among the first 200 eigenvalues in the 60° wedge and among the first 300 eigenvalues in the 49° wedge.

We will refer to these 200 (for $\phi = 60°$) and 300 (for $\phi = 49°$) numerically calculated eigenvalues as the 'exact' quantum eigenvalues from now on.

The horizontal axis in these plots has been scaled so that the average spacing between the eigenvalues is (in the limit of large E) equal to 1. This has been

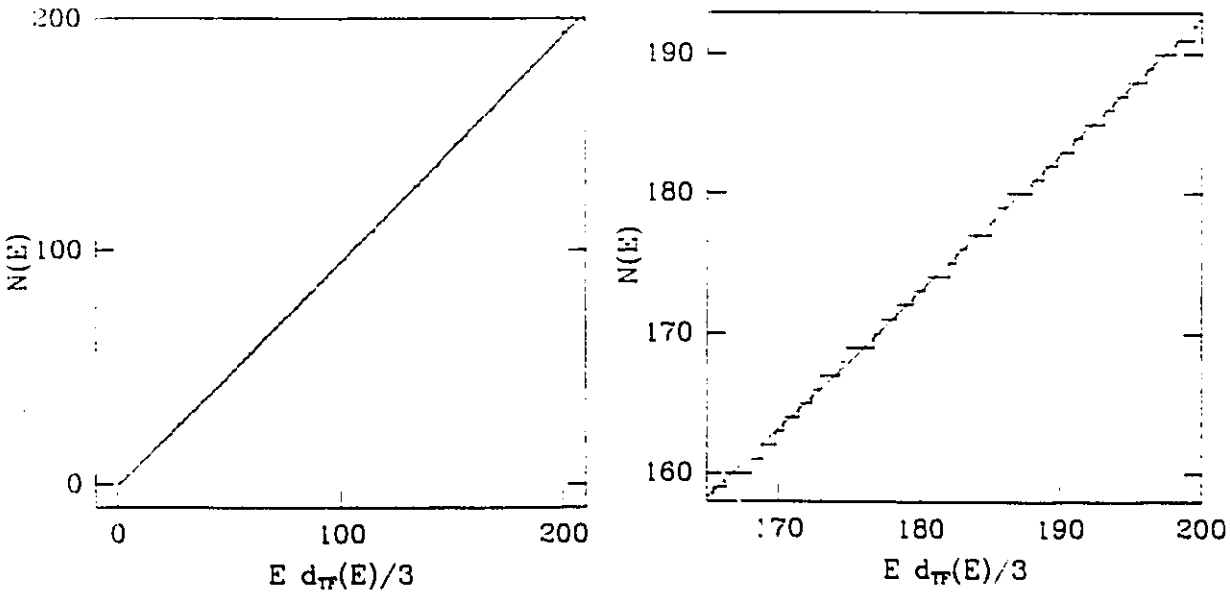

Figure 6.3: The Thomas–Fermi staircase (smooth curve) plotted along with the exact quantum staircase for the first 200 eigenvalues in the 60° wedge. On the scale shown in the left figure the two curves are virtually indistinguishable. An expanded scale plot of the region near $N(E) = 200$ is shown in the right figure.

accomplished as follows.

$$\begin{aligned}\lim_{i\to\infty} E_{i+1}d_{TF}(E_{i+1}) - E_i d_{TF}(E_i) &= \lim_{i\to\infty} E_{i+1}\left(d_{TF}(E_i) + \left.\frac{dd_{TF}(E)}{dE}\right|_{E_i}(E_{i+1}-E_i)\right) \\ &\quad -E_i d_{TF}(E_i) \\ &= \lim_{i\to\infty}(E_{i+1}-E_i)d_{TF}(E_i) + \\ &\quad \left.\frac{dd_{TF}(E)}{dE}\right|_{E_i}(E_{i+1}-E_i)E_{i+1} \end{aligned} \tag{6.1}$$

but

$$d_{TF}(E) = \frac{dN(E)}{dE} \approx \frac{(i+1)-(i)}{E_{i+1}-E_i} = \frac{1}{E_{i+1}-E_i} \tag{6.2}$$

and

$$\lim_{i\to\infty} E_{i+1} \approx E_i. \tag{6.3}$$

Using Eqs. (6.2, 6.3) in Eq. (6.1) gives

$$\lim_{i\to\infty} E_{i+1} d_{TF}(E_{i+1}) - E_i d_{TF}(E_i) = 1 + \lim_{i\to\infty} \left.\frac{d d_{TF}(E)}{dE}\right|_{E_i} \frac{E_i}{d_{TF}(E_i)}. \tag{6.4}$$

If the leading order dependence of the Thomas-Fermi density of states on energy behaves as

$$d_{TF}(E) \propto E^{\beta} \tag{6.5}$$

then from Eq. (6.4)

$$\lim_{i\to\infty} E_{i+1} d_{TF}(E_{i+1}) - E_i d_{TF}(E_i) = 1 + \beta. \tag{6.6}$$

For the wedge billiard, we have from Eq. (B.20) that $d_{TF}(E) \propto E^2$ so that

$$\lim_{i\to\infty} \frac{E_{i+1} d_{TF}(E_{i+1}) - E_i d_{TF}(E_i)}{3} = 1. \tag{6.7}$$

Hence, in the units $E d_{TF}(E)/3$ the spacing between successive eigenvalues is asymptotically equal to 1.

6.1.1 Energy Level Statistics

Energy level statistics (see Berry 1988, 1987, 1985, 1981, Sieber 1991, Sieber and Steiner 1990c and references therein) have been used to characterize the quantum analogs of classically integrable and chaotic systems for some time now.

Define the nearest neighbour spacings distribution $P(\tilde{E})$ as the probability that the spacings between a randomly chosen pair of neighbouring energy eigenvalues will be between $\tilde{E}$ and $\tilde{E}+d\tilde{E}$, where $\tilde{E}$ is the scaled energy defined by

$$\tilde{E} = \frac{d_{TF}(E)}{3}E. \tag{6.8}$$

From Eq. (6.7) the asymptotic spacing between neighbouring eigenvalues in units of $\tilde{E}$ will be equal to 1.

For classically integrable systems the nearest neighbour spacings distribution is given by a Poisson curve

$$P(\tilde{E}) = \exp(-\tilde{E}) \tag{6.9}$$

For classically chaotic systems with time reversal symmetry the nearest neighbour spacings distribution is often given by the so–called Wigner distribution

$$P(\tilde{E}) = \frac{\pi}{2}\tilde{E}\exp\left(-\frac{\pi}{4}\tilde{E}^2\right) \tag{6.10}$$

A quantum system with a Poisson nearest neighbour distribution is often called 'inte-

grable' and a quantum system with a Wigner nearest neighbour distribution is often call 'chaotic'. However, there exist quantum systems which have Poisson statistics and are also classically highly chaotic (Bolte et. al. 1992). Thus although Poisson statistics in a quantum system are often indicative of classically integrable behaviour, such is not always the case.

We give plots of the nearest neighbour spacings distribution in Fig. (6.4) for quantum analogs of the (integrable) 45° wedge, and the classically chaotic 49° and 60° wedges respectively.

The energy eigenvalues of the 45° wedge were computed using a combination of the EBK eigenvalues, Eq. (2.52), for $n_1 > n_2 > 10$ and the exact eigenvalues computed from the zeroes of the Airy function, Eq. (2.49), for $n_1, n_2 \leq 10$. The agreement between the theoretical curve and the calculated histogram is excellent over the entire range.

The calculated histogram for the 49° wedge also shows excellent agreement with the theoretical prediction. The discrepancies between the two curves are probably due to the small number of eigenvalues used in computing the histogram.

The calculated histogram for the 60° wedge shows fairly good agreement with the theoretical predictions. It must be kept in mind that only 200 eigenvalues were used in the computation of the histogram and much of the disagreement between the theory and calculated curves, as in the 49° wedge, may be due to using such a small number of eigenvalues in computing $P(\tilde{E})$.

The fits to the theoretical predictions for both the 49° and 60° wedge are similar in quality to those obtained by Sieber and Steiner 1990 for their system the 'hyperbola billiard'.

Perhaps the main thing to notice about the histograms is that the quantum analogs of classically integrable systems show 'level attraction' whereas the quantum analogs of classically chaotic systems show 'level repulsion'.

6.2 Convergence of the Gutzwiller Trace formula

In this section we examine the convergence properties of the Gutzwiller Trace formula, Eqs. (3.10, 3.11). There are two questions we will ask in relation to these formulas.

The first question is; 'Are the number of periodic orbits growing faster than they are being damped out in the Trace formula?' Even though the contribution of each periodic orbit is decreasing as $\exp(-\nu_\gamma/2)$ (see Eqs. (3.10,3.11)) the number of periodic orbits may be growing even faster and the sum may not converge. Is this the case in the wedge Billiard? We answer this question by following a procedure similar to that given by Eckhardt and Aurell 1989, and Sieber and Steiner 1990. We start with Eq. (3.10) which we reproduce here (recall, we've set $\hbar = 1$).

$$\sum_n \frac{1}{E - E_n} = g_{TF}(E) + \sum_{\gamma=P.P.O} \sum_{k=1}^{\infty} \frac{T_\gamma(E)}{i} \frac{\exp\left\{k\left[iS_\gamma(E) - i\frac{u_\gamma \pi}{2}\right]\right\}}{\left(e^{k\nu_\gamma/2} - \sigma_\gamma^k e^{-k\nu_\gamma/2}\right)} \tag{6.11}$$

It must be kept in mind that E may be complex in Eq. (6.11). Using $S_\gamma(E) =$

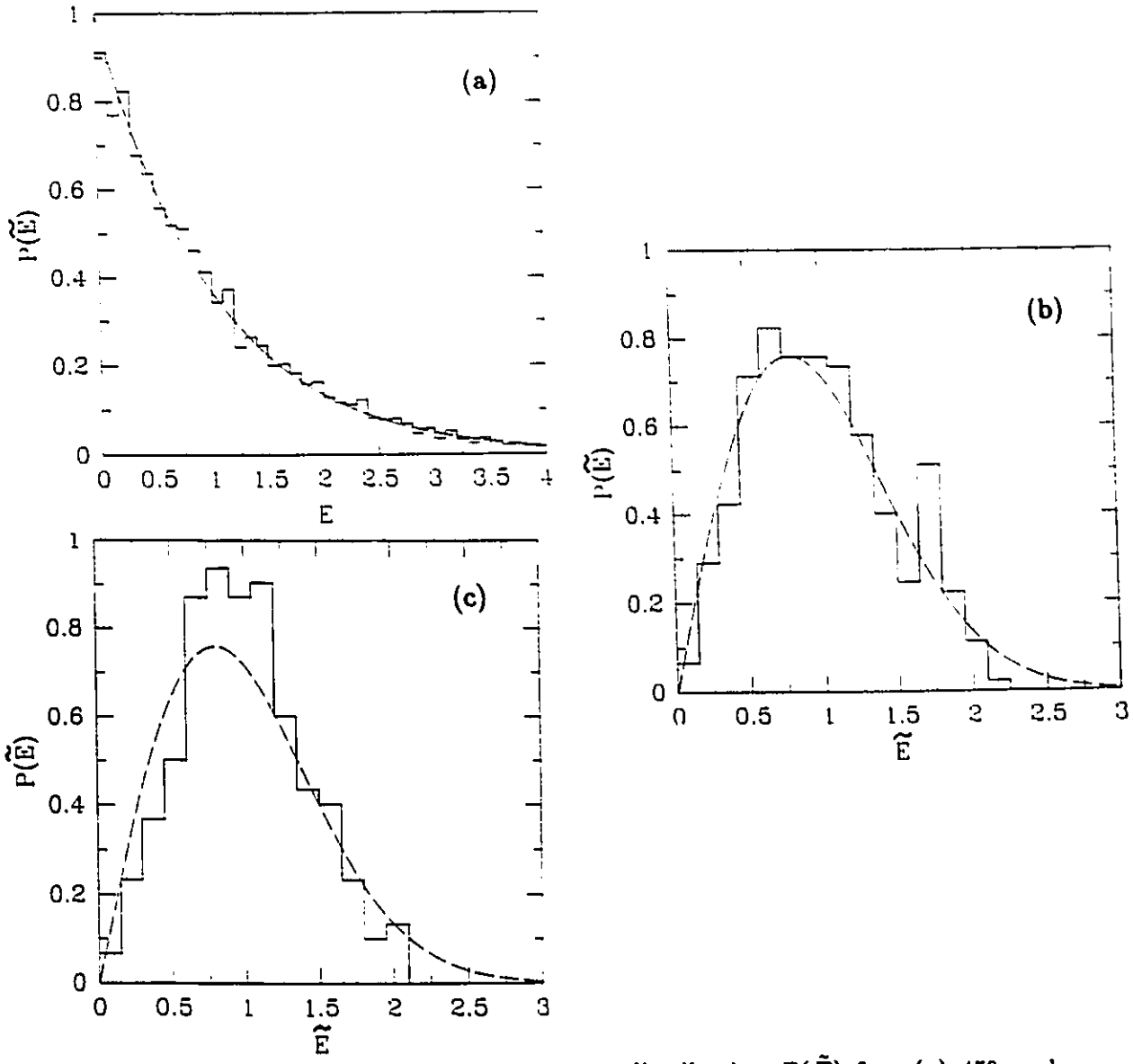

Figure 6.4: The nearest neighbour spacings distribution $P(\tilde{E})$ for: (a) 45° wedge, using the first 5000 energy eigenvalues. The histogram bin size is 0.1 and the dashed curve is the theoretical prediction of $P(\tilde{E}) = e^{-\tilde{E}}$. (b) 49° wedge, using the first 300 energy eigenvalues. The histogram bin size is 0.15 and the dashed curve is the theoretical prediction of $P(\tilde{E}) = \pi/2 \exp(-\pi\tilde{E}^2/4)$. (b) 60° wedge, using the first 200 energy eigenvalues. The histogram bin size is 0.15 and the dashed curve is the theoretical prediction of $P(\tilde{E}) = \pi/2 \exp(-\pi\tilde{E}^2/4)$.

$S_\gamma(1)E^{3/2}$, $T_\gamma(E) = 3S_\gamma(1)E^{1/2}/2$ and that for large word length (and hence from Fig. (5.9) large ν_γ) $(\exp(k\nu_\gamma/2) - \sigma_\gamma^k \exp(-k\nu_\gamma/2))^{-1} \approx \exp(-k\nu_\gamma/2)$ we get

$$\sum_n \frac{1}{E - E_n} = g_{TF}(E) + \sum_{\gamma=P.P.O} \sum_{k=1}^{\infty} \frac{3S_\gamma E^{1/2}}{2i} \exp\left\{k\left[iS_\gamma E^{3/2} - i\frac{u_\gamma \pi}{2} - \frac{\nu_\gamma}{2}\right]\right\} \quad (6.12)$$

Now, from Eq. (5.6), on average, the number of orbits increases with word length as

$$N(n) = N_\circ \exp \tau_w n \quad (6.13)$$

where τ_w is the word length entropy (given numerically for the wedge billiard by the slopes of the lines in Fig. (5.13)). Also, the average action $\bar{S}$, average stability exponent $\bar{\nu}$ and average Maslov index $\bar{u}$ increase linearly with word length as shown in Figs. (5.8, 5.9, 5.10). We write these linear relationships as

$$\bar{S}(n) = m_S n + b_s \qquad \bar{\nu}(n) = m_\nu n + b_\nu \qquad \bar{u}(n) = m_u n + b_u \quad (6.14)$$

where the slopes m and intercepts b may be read off Figs. (5.8, 5.9, 5.10). The sum over γ in Eq. (6.12) is now replaced by a sum over word length n

$$\begin{aligned}\sum_n \frac{1}{E - E_n} &= g_{TF}(E) + \sum_n \sum_{k=1}^{\infty} \frac{(m_S n + b_S) B E^{1/2} N_\circ}{2i} \\ &\quad \times \exp\left\{kn\left[im_S E^{3/2} - i\frac{m_u \pi}{2} - \frac{m_\nu}{2} + \tau_w n\right]\right\} \quad (6.15)\end{aligned}$$

where B is some finite constant. Writing $E^{3/2}$ as

$$E^{3/2} = \mathrm{Re}E^{3/2} + i\mathrm{Im}E^{3/2} \tag{6.16}$$

and using this in Eq. (6.15) we get

$$\sum_n \frac{1}{E-E_n} = g_{TF}(E) \;+\; \sum_n \sum_{k=1}^{\infty} \frac{(m_S n + b_S) B E^{1/2}}{2i} \exp\left\{kn\left[im_S \mathrm{Re}E^{3/2} - i\frac{m_u \pi}{2}\right]\right\} \times \exp\left\{kn\left[-m_S \mathrm{Im}E^{3/2} - \frac{m_\nu}{2} + \tau_w\right]\right\} \tag{6.17}$$

This sum will converge absolutely if

$$m_S \mathrm{Im}E^{3/2} + \frac{m_\nu}{2} - \tau_w > 0$$

or

$$\mathrm{Im}E^{3/2} > \frac{\tau_w}{m_S} - \frac{m_\nu}{2m_S} \tag{6.18}$$

For the 60° wedge we have from Figs. (5.8, 5.9, 5.10) that $m_S = 1.026$, $m_\nu = 0.635$, and $\tau_w = 0.496$, hence $\mathrm{Im}E^{3/2} > 0.174$. Similarly, for the 49° wedge, $m_S = 0.847$, $m_\nu = 0.474$, and $\tau_w = 0.341$ so that $\mathrm{Im}E^{3/2} > 0.123$. In neither case does the Gutzwiller Trace formula converge absolutely for real E. Hence the answer to the first question seems to be that the number of periodic orbits is growing faster than they are being damped out so that absolute convergence is not guaranteed. This is similar to the situation found by Sieber 1990, who found that in the case of the

'hyperbola billiard' $\mathrm{Im}E^{1/2} > 0.23$.

The second question is; 'Can the Gutzwiller sum still converge even though the number of periodic orbits is growing faster than they are being damped out? Can it still be conditionally convergent?' Since the sign of the Maslov index changes from orbit to orbit successive terms in the sum may enter with opposite signs and may cancel each other in the sum. If such a situation happens then the Gutzwiller sum may still converge. From our numerical investigations it seems that the Maslov index is equally likely to be any of 0,1,2,3 (mod(4)) and hence many terms have the opportunity to cancel others. However, without the details of the orbits themselves it is not possible to say whether the sum converges or not. Thus, there is still the possibility that the Gutzwiller trace formula converges for the 49° and 60° wedges but there is no guarantee.

Sieber 1990 presents evidence that even though in the case of the hyperbola billiard the condition for absolute convergence $\mathrm{Im}E^{1/2} > 0.23$ is not satisfied by real E, nonetheless, the Gutzwiller trace formula does conditionally converge for real E. A similar situation may occur in the wedge billiard for $\phi = 49°$ or $\phi = 60°$ or both.

6.3 Non–Isolated Families of Periodic Orbits: Quantum Consequences

In Sec. (5.2.1) we examined two families of non–isolated classical periodic orbits in the wedge billiard. The existence of such families has important consequences in the application of the Gutzwiller trace formula. Hence before examining any applications of the trace formula we turn to an analysis of these consequences.

In the derivation of the Gutzwiller trace formula (Gutzwiller 1971) the following integral arises

$$\sum_{\gamma} \int_{-\infty}^{\infty} \exp\left(\frac{i}{\hbar}\delta^2 S_\gamma q_2^2\right) dq_2 \tag{6.19}$$

where $\delta^2 S_\gamma$ is given from Eq. (5.3) as

$$\delta^2 S_\gamma = \frac{\partial^2 S_\gamma}{\partial q_2 \partial q_2} + 2\frac{\partial^2 S_\gamma}{\partial q_2 \partial q_2'} + \frac{\partial^2 S_\gamma}{\partial q_2' \partial q_2'}. \tag{6.20}$$

This integral is the result of expanding the action near the periodic orbit, in a direction perpendicular to the periodic orbit (δq_2), about the periodic orbit.

Two periodic orbits, labelled by m and $m-1$ are isolated if

$$\lim_{\hbar \to 0} \delta^2 S_m \Delta x_m^2 >> \hbar \tag{6.21}$$

where

$$\Delta x_m^2 = (q_{2,m-1} - q_{2,m})^2 \tag{6.22}$$

is the distance between the two periodic orbits evaluated at some point along the orbit m (typically, it is convenient to use a point of collision with the tilted wall), and $\delta^2 S_m$ is evaluated for one traversal of the periodic orbit starting at the same point along m.

If the condition given by Eq. (6.21) holds then the integrand in Eq. (6.19) for some m will not overlap the integrand from $m-1$. (I prefer to think of the integral for each m as a Gaussian integral of width $\sqrt{\hbar/\delta^2 S_m}$). Then the two integrals may be done separately (as Gaussian integrals) and the two periodic orbits end up contributing separately to the Gutzwiller trace formula.

However, if

$$\lim_{\hbar \to 0} \delta^2 S_m \Delta x_m^2 \approx \lim_{\hbar \to 0} \hbar = 0 \tag{6.23}$$

then the integrand from one m overlaps that of $m-1$ and the two Gaussian integrals may not be done separately. The Gutzwiller derivation cannot be carried through and hence the non–isolated (in the sense of Eq. (6.23)) periodic orbits do not contribute in the regular way to the Gutzwiller trace formula.

We show in Figs. (6.5,6.6) an evaluation of the product $\ln(\delta^2 S_m \Delta x_m^2)$ vs. $\ln(m)$ for the families $T^m VVV$ and $T^m VVTTVV$ in the 60° and 49° wedges respectively. The results clearly show that $\delta^2 S_m \Delta x_m^2 \propto m^{-0.926}$ for the family $T^m VVV$ and

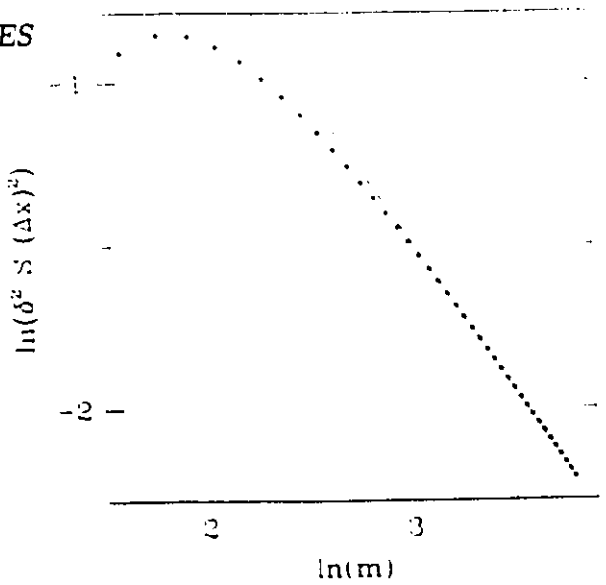

Figure 6.5: A plot of $\delta^2 S_m \Delta x_m^2$ for the family $T^m VVV$ in the 60° wedge. The perpendicular distance between the orbits Δx_m^2 is evaluated when both orbits are at the rightmost T collision on the tilted wall (near the point $x = y\cot\phi,\ \ y = 1$). The slope of the dashed line is -0.926

$\delta^2 S_m \Delta x_m^2 \propto m^{-2.094}$ for the family $T^m VVTTVV$. For both families $\lim_{m\to\infty} \delta^2 S_m \Delta x_m^2 = 0$ and hence these orbits are non–isolated in the sense of Eq. (6.23).

For integrable systems $\delta^2 S = 0$ and the condition expressed by Eq. (6.23) is fulfilled. All periodic orbits in integrable systems are non–isolated. In this case a parameter may be continuously varied to go from one periodic orbit to another. Then an analog of the Gutzwiller trace formula (Berry and Tabor 1977) may be derived and these non–isolated periodic orbits properly taken into account.

However, for the families we have encountered no such continuous parameter takes us from one periodic orbit to another and we cannot apply the method of Berry and Tabor. At some point (some m value, or wordlength) these periodic orbits should not be included in the Gutzwiller trace formula. At what point this occurs is unclear (as $\hbar$ is not really 0 in our semiclassical calculations, and hence the limit in Eq. (6.23)

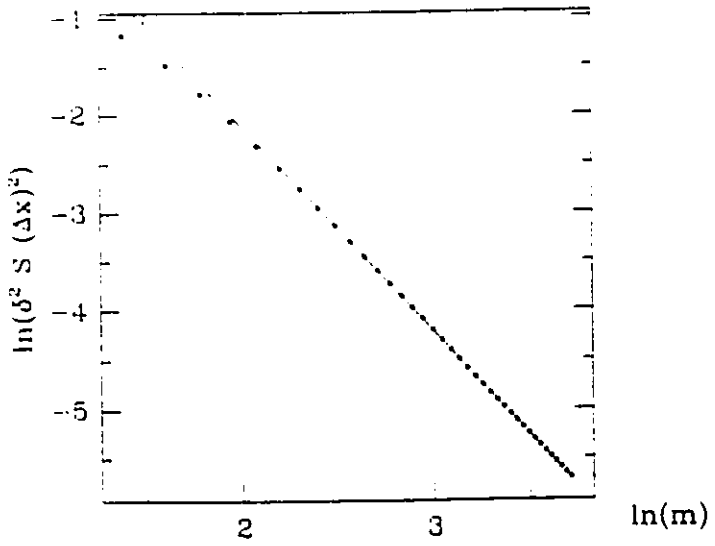

Figure 6.6: A plot of $\delta^2 S_m \Delta x_m^2$ for the family $T^m VVTTVV$ in the 49° wedge. The perpendicular distance between the orbits Δx_m^2 is evaluated when both orbits are at the rightmost T collision on the tilted wall (near the point $x = y\cot\phi,\ \ y = 1$). The slope of the dashed line is -2.094

is not really 0) but it seems safe to say that it is not necessary to include an infinity of orbits from any of these non–isolated families in the Gutzwiller trace formula.

We shall see in the results of Sec (6.4) that there are some discrepancies in our classically calculated curves near the actions of these infinite families. This is a hint that these families do indeed become non–isolated and should be removed from the Gutzwiller trace formula calculations.

6.4 Classical Mechanics from the Quantum Mechanics: Results

Using the exact quantum eigenvalues we may evaluate the expressions given in Sec. (3.2.1), Eqs. (3.23, 3.27), the so-called *damped sine* and *damped cosine* transforms

respectively. Such an evaluation is carried out in Figs. (6.7, 6.8). The parameter α allows us to cut off the contributions from the higher eigenvalues (which aren't known very accurately). Keeping in mind the discussion in Sec. (6.1) we chose α such that $\exp(-\alpha E_i) = 0.01$ where $i = 200$ for the 60° wedge and $i = 300$ for the 49° wedge respectively. These values of α mean that the inaccurate eigenvalues have negligible contributions to the transforms. We will focus initially on the contribution to the damped sine transform (the long dashed curve in the top figure in Fig. (6.7)). From Table (5.1) we see that $S_V = 1.33333$ and $u_V = 5$. This means that in evaluating the sum on the RHS of Eq. (3.23), for $k = 1$, $\sin(ku_V\pi/2) = \sin(5\pi/2) = 1$ whereas $\cos(ku_V\pi/2) = \cos(5\pi/2) = 0$. Thus the coefficient of the peak function is 1 and the coefficient of the crossing function is 0 for $k = 1$. Since $S_V = 1.33333$, there should be a positive peak (see Eq. (3.25)) at this value of ω and indeed, in the sine transforms there is a positive Lorentzian peak located at $\omega = 1.33$. For $k = 2$, $\sin(5\pi) = 0$ and $\cos(5\pi) = -1$. Thus the coefficient of the crossing function is -1 while the coefficient of the peak function is 0. Looking at Eq. (3.24) we see that this means we should have a crossing from positive to negative at $\omega = 2.666$. Indeed, this is exactly what happens. By setting $k = 3, 4, \ldots$ we obtain the sequences of crossings and peaks shown in the figure. The rate of decay of the amplitudes of the peaks and crossings is determined by the stability exponent of the periodic orbit (see Eq. (3.23)). The ratio of the amplitudes of successive peaks (k increases by 2) is approximately given by $|A_{k+2}/A_k| \approx \exp(-\nu_\gamma)$. This exponential decay is evident in Fig. (6.7).

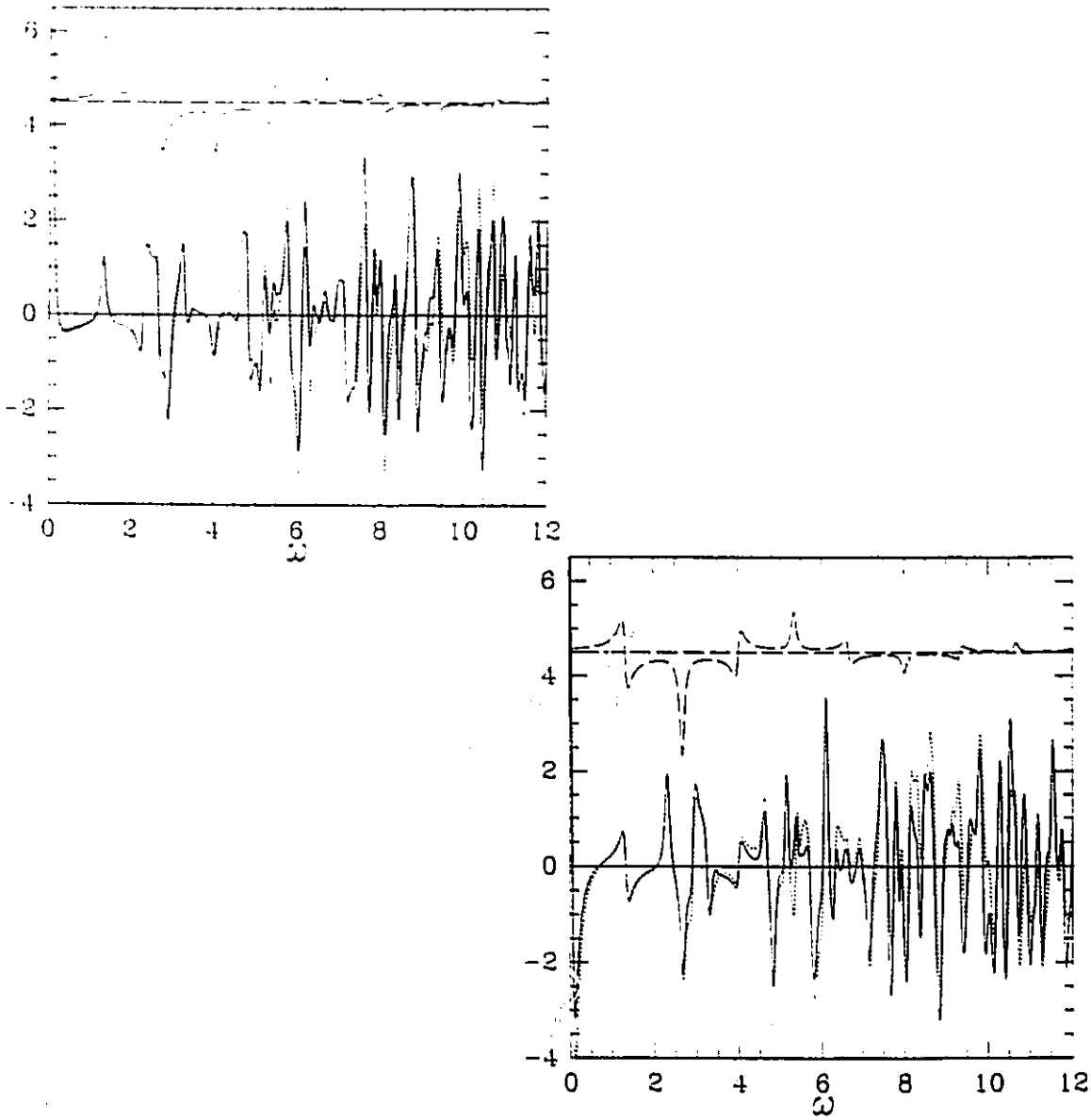

Figure 6.7: The damped sine transform (top figure) and damped cosine transform (bottom figure) evaluated for the 60° wedge with $\alpha = 0.069$. The solid curve shows the evaluation of the LHS of Eqs. (3.23, 3.27) using the exact quantum eigenvalues and the short dashed curve shows the evaluation of the RHS of Eqs. (3.23, 3.27) using 257 classical periodic orbits with $S_\gamma \leq 12$ and word length ≤ 16. The curve shown above (long dashed line) is the contribution to the RHS in Eqs. (3.23 , 3.27) due to the periodic orbit labelled by V

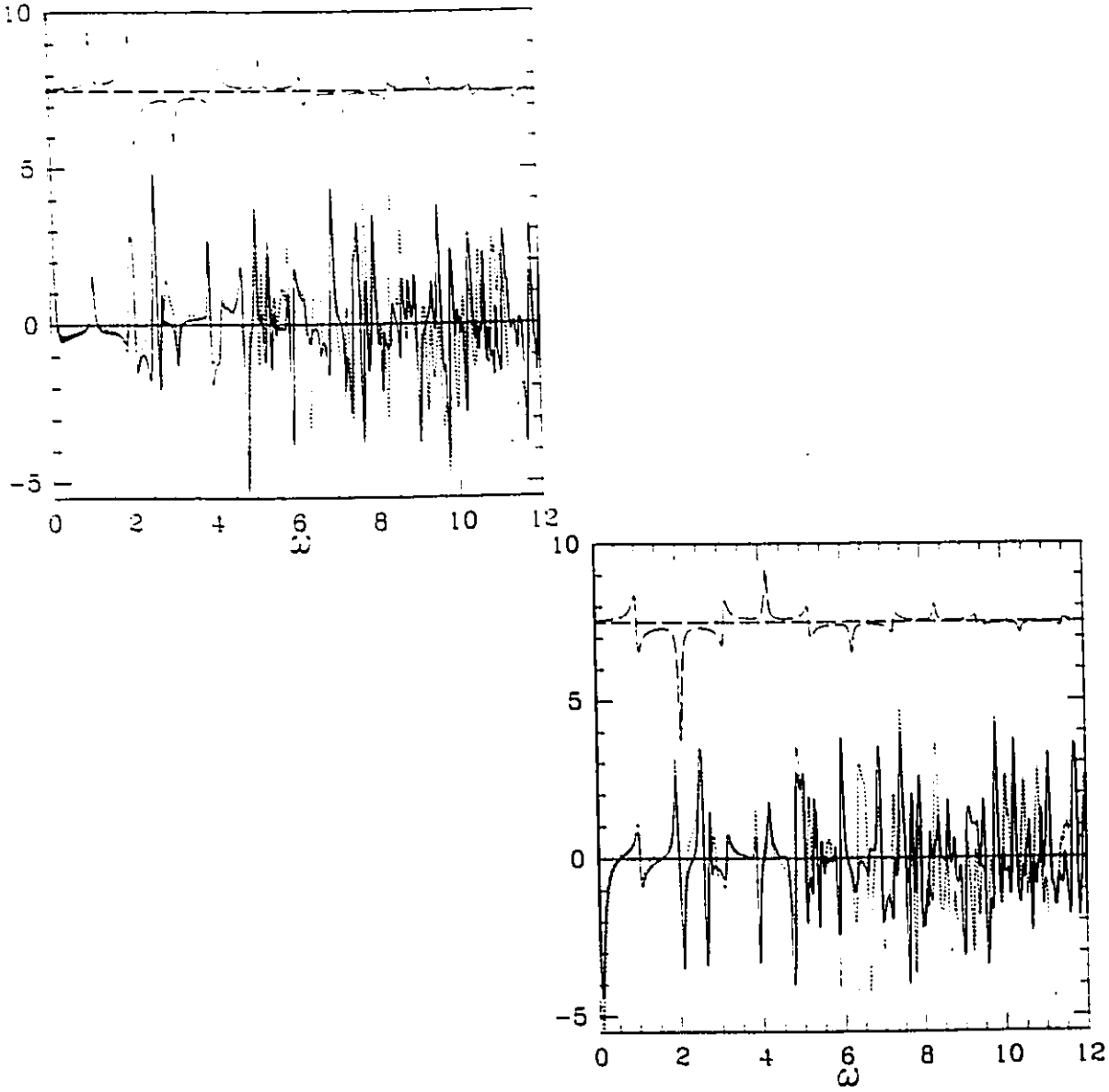

Figure 6.8: The damped sine transform (top figure) and damped cosine transform (bottom figure) evaluated for the 49° wedge with $\alpha = 0.045$. The solid curve shows the evaluation of the LHS of Eq. (3.23) using the exact quantum eigenvalues and the short dashed curve shows the evaluation of the RHS of Eqs. (3.23, 3.27) using 271 classical periodic orbits with $S_\gamma \leq 12$ and word length ≤ 19. The curve shown above (long dashed line) is the contribution to the RHS in Eqs. (3.23 , 3.27) due to the periodic orbit labelled by V

The short dotted curve in Fig (6.7) is obtained by adding together the contributions of all the periodic orbits with $S_\gamma \leq 12$ and also the contribution from the Thomas–Fermi term. The vertex orbit was included in the classical (RHS) sum by including the two orbits TVV and $TTTV$ in the limit $\phi \to 60°$, each with amplitude 1/2. There is good agreement between the solid (quantum) curve and the short dotted (classical) curve over almost the entire range. The large peak near $\omega = 0$ is due to the Thomas–Fermi term and the agreement between the two curves in this region is excellent. Note that the contribution due to the vertex orbit (at $\omega \approx 3.26$) is correctly reproduced. The first notable discrepancy occurs at $\omega \approx 5.5$ and may be due to the infinite family T^mVVV mentioned earlier and the inapplicability of the Gutzwiller sum to such non–isolated families. Other discrepancies occur for larger ω but the general agreement between the two curves is still excellent.

The damped cosine transform (bottom figure in Fig. (6.7)) shows remarkable agreement between the quantum and classical results, including the Thomas–Fermi peak near $\omega = 0$. Again, the first notable exception is near $\omega \approx 5.5$.

The good agreement between the classical and quantum curves is support for the validity of the Gutzwiller trace formula. It also shows that we have obtained all (or almost all) of the classical periodic orbits which have $S_\gamma \leq 12$ in the 60° wedge by the time the word length has reached 16, which is the limit of orbits included in Fig. (6.7).

For the 49° wedge, Fig. (6.8), the smaller value of α means that the am-

plitudes of the peaks and crossings are larger and the positions of the peaks and crossings more sharply resolved. However, the agreement between the classical and quantum curves is not as good as in the 60° wedge. Although many of the features of the quantum curve are correctly reproduced by the classical curve (such as the amplitudes and positions of the Thomas–Fermi peaks and the first few periodic orbit peaks and crossings) the agreement becomes quite questionable beyond the serious disagreement at $\omega \approx 6.6$. The first family of non–isolated orbits in the 49° wedge occurs at $\omega \approx 5.5$ and so the non–isolated family is not the source of the disagreement in this case.

The relatively poor agreement for the 49° could mean that either the Gutzwiller trace formula fails in this case (perhaps because the sum is not convergent) or that we have missed some periodic orbits with $S_\gamma \leq 12$.

The preceeding discussion suggests a way of recovering the actions, periods, stability exponents and Maslov indices of the classical periodic orbits if one is only given the quantum (solid) curve. First one identifies the first and second occurrences of a well defined peak believed to belong to a periodic orbit. The peaks with smallest ω should be chosen, corresponding to the shortest periodic orbit. By measuring the position of the first peak, ω_1, the action of the periodic orbit may be directly read off, $S_\gamma = k\omega_1$, $k = 1$. The ratio of the amplitudes of the first peak to the second peak will give the stability exponent $\nu_\gamma = ln(A_1/A_2)$. The sequence of crossings and peaks, along with whether they are positive or negative determines the Maslov index u_γ.

Once these quantities are known the contribution due to this orbit is subtracted off the quantum curve. This leaves a new curve with a new series of peaks and crossings. The entire procedure is repeated to give the next shortest periodic orbit and so on.

This procedure will break down once two or more periodic orbits with very similar actions are encountered. Then one is no longer able to distinguish the contributions from each orbit individually.

6.5 The Gutzwiller Trace Formula: Results

In this section we present the results of a numerical evaluation of the Gutzwiller trace formula, Eqs. (3.11,3.16).

We show in Figs. (6.9) an evaluation of Eq. (3.16) for the 60° wedge using 257 orbits with $S_\gamma \leq 12.0$, and word lengths $n \leq 15$, and some with $n = 16$. The vertex orbit was included in the sum in Eq. (3.16) by including the two orbits TVV and $TTTV$ in the limit $\phi \to 60°$, each with amplitude 1/2.

The peaks in Fig. (6.9) should correspond to the energy eigenvalues. One can see that there is excellent agreement between the locations of the peaks and the locations of the exact quantum energy eigenvalues. The first 21 peaks are in one–to–one correspondence with an eigenvalue and beyond that the peaks still describe the locations of clusters of eigenvalues. The first peak which does not resolved two individual eigenvalues is that at the 22^{nd} and 23^{rd} eigenvalues. Expressing Eq. (3.20)

in terms of scaled energy $\tilde{E}$ we find that using periodic orbits of action $S_\gamma \leq S_{max}$ we should be able to resolve energy eigenvalues up to

$$\tilde{E}_{max} = \frac{E d_{TF}(E)}{3} \approx \frac{3S_{max}^2}{4\pi \tan\phi}. \tag{6.24}$$

For the 60° wedge with $S_{max} = 12.0$ we find $\tilde{E}_{max} \approx 20$. Beyond about $\tilde{E}_{max}$ the energy eigenvalues may not be resolved. Indeed, E_{22} corresponds to $\tilde{E} \approx 26 > \tilde{E}_{max}$, and hence our estimate is correct.

A more quantitative comparison between the peaks and locations of the energy eigenvalues is given in Fig. (6.10). This figure shows the difference, in units of scaled energy, between the exact quantum eigenvalues and the locations of the maxima in Fig. (6.9). One can see that the first 20 eigenvalues are predicted to within ±20% of the average level spacing.

By increasing the number of periodic orbits included in the sum in Eq. (3.16) the peaks should become sharper and their amplitudes larger. Shown in Fig. (6.11) is an evaluation of Eq. (3.16) with 1621 periodic orbits with $S_{max} = 19.42$ in the 60° wedge. Indeed, the amplitudes of the peaks have grown in relation to Fig. (6.9) and they have become sharper. Note that the two eigenvalues which were not resolved for $S_{max} = 12.0$ are now resolved. In this case the first non–resolved eigenvalues are the 25^{th} and 26^{th} eigenvalues at $\tilde{E} \approx 26$. Our estimate of $\tilde{E}_{max}$ for $S_{max} = 19.42$ is $\tilde{E}_{max} \approx 50$. This is well beyond where we have lost resolution of eigenvalues.

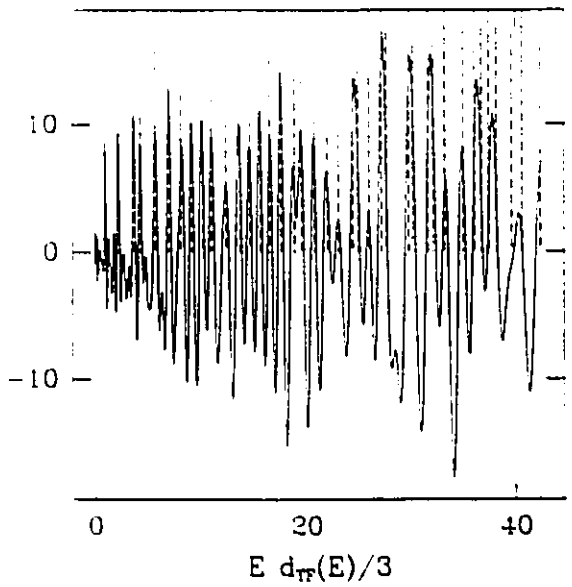

Figure 6.9: The solid curve shows an evaluation of Eq. (3.16) for the 60° wedge using 257 orbits with $S_\gamma \leq 12.0$, and word lengths $n \leq 15$, and some with $n = 16$. The vertical dashed lines show the positions of the exact quantum eigenvalues. The horizontal axis has been scaled so that the distance between the exact quantum eigenvalues is on average equal to 1.

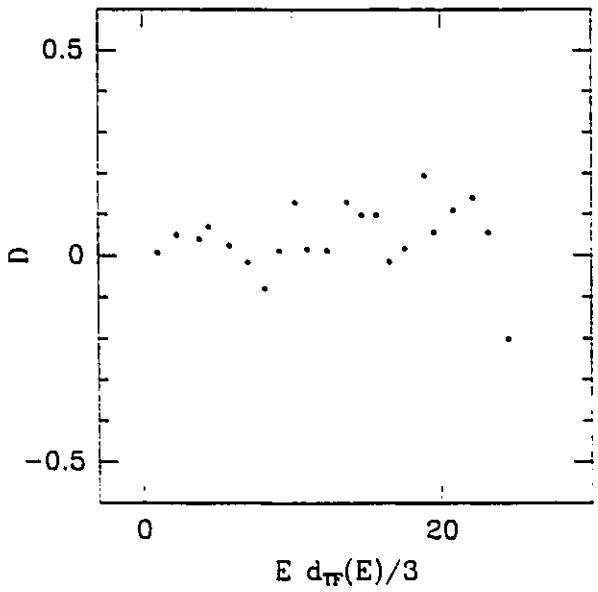

Figure 6.10: The difference between the exact scaled eigenvalue energy $\tilde{E}_i$ and the maxima of the peaks (with heights ≥ 2.0) in Fig. (6.9) for the first 21 eigenvalues plotted against $\tilde{E}_i$.

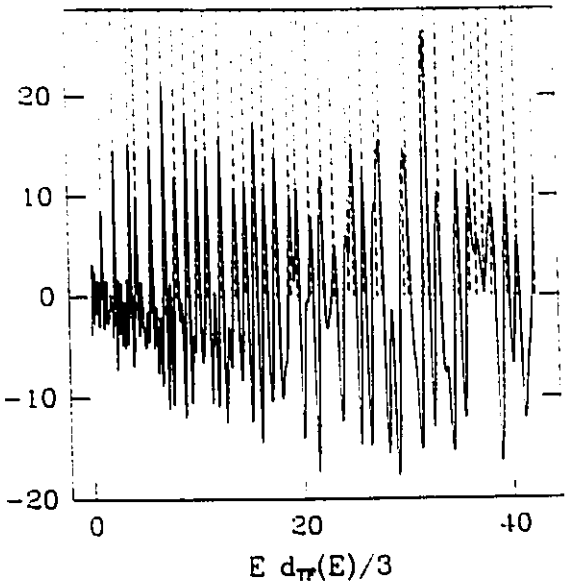

Figure 6.11: The solid curve shows an evaluation of Eq. (3.16) for the 60° wedge using 1621 orbits with $S_\gamma \leq 19.42$, and word lengths $n \leq 15$, and some with $n = 16$. The vertical dashed lines show the positions of the exact quantum eigenvalues. The horizontal axis has been scaled so that the distance between the exact quantum eigenvalues is on average equal to 1.

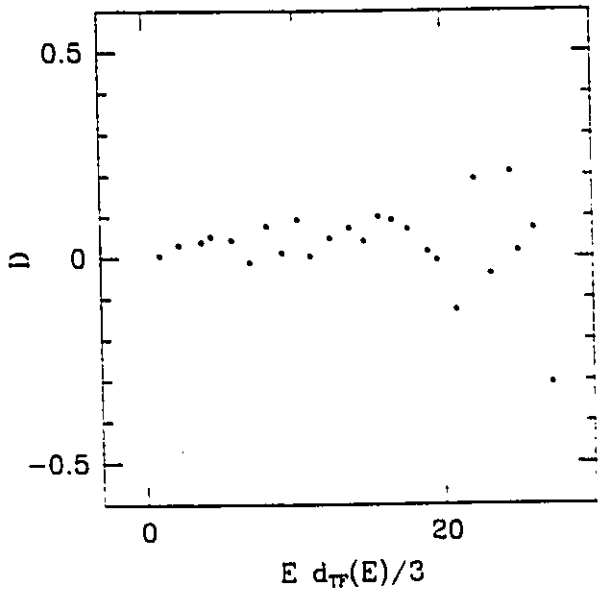

Figure 6.12: The difference between the exact scaled eigenvalue energy $\tilde{E}_i$ and the maxima of the peaks (with heights ≥ 4.0) in Fig. (6.11) for the first 25 eigenvalues plotted against $\tilde{E}_i$.

However, this is probably not due to a mistake in Eq. (6.24), rather to the fact that we do not know all the orbits with $S \leq S_{max}$. There are at least several hundred orbits we are missing below S_{max} which because of numerical limitations we were not able to find.

The quantitative agreement between the peaks and locations of the energy eigenvalues is examined in Fig. (6.12). There has been some improvement in relation to Fig. (6.10) but the improvement is not as large as one might expect from increasing the number of orbits in the sum by a factor of 6. This is one of the shortcomings of Eq. (3.16). Since the number of periodic orbits below word length n grows exponentially with n (see Sec. (5.4)) but the energy resolution depends on the square of S_{max} (which grows linearly with n), one has to put in exponentially more information to get quadratically more eigenvalues. At some point one must trade off the number of eigenvalues obtained because of computational limitations.

Overall, the agreement between the locations of the peaks in Figs. (6.9, 6.11) and the locations of the exact quantum energies is excellent, especially considering the small number of periodic orbits used. Sieber and Steiner (1990b) used 136,699 periodic orbits and could only resolve the first 7 energy eigenvalues in the hyperbola billiard. Aurich and Steiner (1992) used over 4 million periodic orbits (which correspond to about 1500 different actions) to determine the first 7 energy eigenvalues in the regular hyperbolic octagon. With only 257 periodic orbits we were able to resolve the first 20 energy eigenvalues quite accurately.

Figs. (6.13, 6.14) show the results of an evaluation of Eq. (3.16) for the 49° wedge. 271 orbits with $S_\gamma \leq 12.0$ and word length $n \leq 19$ were used in calculating the solid curve in Fig. (6.13). The results are disappointing when compared to the results for the 60° wedge. Although the positions of the peaks generally line up with the positions of the eigenvalues there are many spurious peaks and no one–to–one correspondence exists between the eigenvalues and peaks, even for the low lying eigenvalues. The situation does not improve much when more periodic orbits are added. In Fig. (6.14) 1048 periodic orbits with $S_\gamma \leq 19.48$, which corresponds to all periodic orbits with word length $n \leq 19$, were used to compute the solid curve. The peaks, as before, become more sharply defined and grow in height but the noise between the peaks does not shrink appreciably. Hence, if one just had access to the solid curve and was asked to pick out the peaks corresponding to the energy eigenvalues one could not do it in an unambiguous way. As an example, there are two peaks lying very close together near the 4^{th} energy eigenvalue. Which peak corresponds to this eigenvalue? Both peaks are greater in magnitude than the peak for the 3^{rd} eigenvalue, so both should presumably be eigenvalues. One is in a quandary; which peak to choose?

Because of such ambiguity the straightforward Gutzwiller trace formula, Eq. (3.16) is perhaps not the best function to use in evaluating quantum energies from classical periodic orbits.

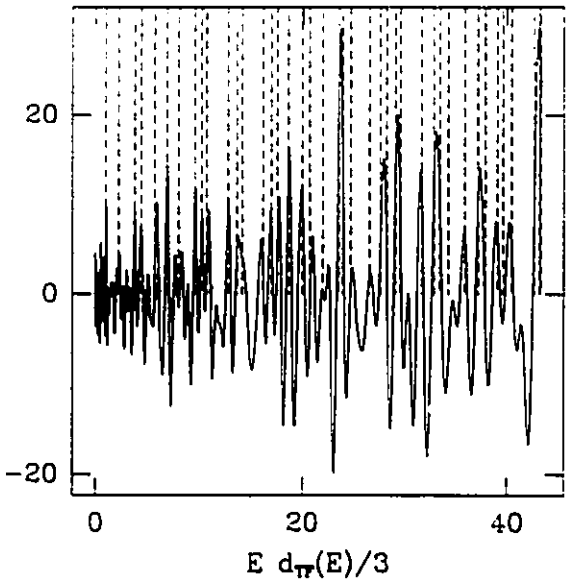

Figure 6.13: The solid curve shows an evaluation of Eq. (3.16) for the 49° wedge using 271 orbits with $S_\gamma \leq 12.0$ and with word length $n \leq 19$. The vertical dashed lines show the positions of the exact quantum eigenvalues. The horizontal axis has been scaled so that the distance between the exact quantum eigenvalues is on average equal to 1.

6.6 The quantum staircase $N(E)$: Results

In Sec. (3.2.2) we derived a formula, Eq. (3.31), which allowed the exact quantum staircase $N(E)$ to be approximated by a smoothly varying Thomas–Fermi term and oscillatory term containing information about the classical periodic orbits.

Fig. (6.15a) shows an evaluation of Eq. (3.31) for the 60° wedge using the Thomas–Fermi term from Eq. (3.32) and 257 periodic orbits with $S_\gamma \leq 12.0$ and word lengths $n \leq 16$. One can see that for the first few step at least, the semiclassical curve (the RHS of Eq. (3.31)) does a fairly good job of approximating the the exact quantum staircase. Adding more periodic orbits should make the approximation even

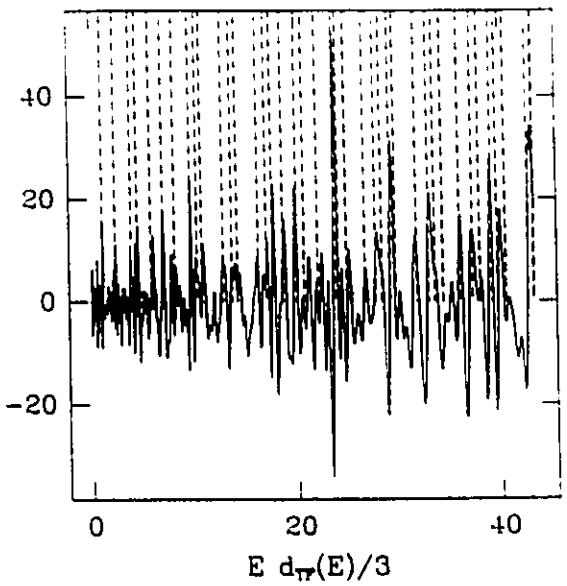

Figure 6.14: The solid curve shows an evaluation of Eq. (3.16) for the 49° wedge using 1048 orbits with $S_\gamma \leq 19.48$. This corresponds to all orbits with word length $n \leq 19$. The vertical dashed lines show the positions of the exact quantum eigenvalues. The horizontal axis has been scaled so that the distance between the exact quantum eigenvalues is on average equal to 1.

better. Fig. (6.15c) shows an evaluation of Eq. (3.31) for the 60° wedge using 1621 periodic orbits, which corresponds to all periodic orbits with word length $n \leq 15$ and several hundred with word length $n = 16$.

The novel quantization procedure, Eq. (3.33) recently proposed by Aurich et. al. may be interpreted quite easily once one examines Fig. (6.15a). The function $\cos(\pi\{N_{TF}(E) + N_{OSC}(E)\})$ has its zeroes precisely at the values where the semiclassical approximation crosses the half integral values of N

$$N_{SC}(E) = N_{TF}(E) + N_{OSC}(E) = i + 1/2 \qquad i = 0, 1, 2, \ldots \tag{6.25}$$

This quantization condition has to be modified somewhat in the case of the wedge billiard as we shall see.

Fig. (6.16a) shows an evaluation of Eq. (3.31) the 49° wedge using 271 periodic orbits with $S_\gamma \leq 12.0$ and having word length $n \leq 19$. Notice how the semiclassical curve often crosses the half integral values of N several times (such as at $N = 5.5$ where it crosses three times). If the quantization condition Eq. (3.33) were used then three eigenvalues would be predicted near $N = 5.5$ instead of one. To circumvent this difficulty we apply the following modification. We move to the point where the Thomas–Fermi curve crosses the half integral values of N and then horizontally across to the nearest point on the curve $N_{SC}(E)$. This gives us one unique point on $N_{SC}(E)$ for each half integer value of N.

Using this quantization procedure (which we will call *staircase quantization*) we may calculate the energies predicted by the curve $N_{SC}(E)$ and compare them with the exact quantum energies.

We may also analytically compute where the Thomas–Fermi curve $N_{TF}(E)$ crosses half integral values of N, $N = i + 1/2 \quad i = 0, 1, 2 \ldots$. From Eq. (3.32) with $\hbar = 1$, we must solve

$$N_{TF}(E) = \frac{1}{12\pi \cot\phi} E^3 - \frac{1}{6\pi}\sqrt{\frac{2}{m}}(1 + \sec\phi)E^{3/2} + 1/6 = i + 1/2 \qquad (6.26)$$

Eq. (6.26) is a quadratic equation on $E^{3/2}$ and is easily solved for $E(i)$. We call these

energies the 'Thomas–Fermi' energies.

One of the main advantages of using the staircase quantization procedure is that the addition of the Thomas–Fermi term allows an unambiguous identification of energy eigenvalues. This overcomes the greatest shortcoming of the Gutzwiller trace formula quantization (Sec. (6.5)) which was the ambiguity in identifying peaks with eigenvalues for the 49° wedge.

The Thomas–Fermi term also 'stretches out' the Gutzwiller trace formula in some sense and allows individual energies to be computed to arbitrary energy, whereas the Gutzwiller trace formula was limited by the energy resolution given by the width of the peaks to relatively low energies. Thus, even though the accuracy with which the first few energy eigenvalues are determined does not change much (see the first twenty or so eigenvalues in Figs. (6.10) and (6.15b) for example) the staircase quantization allows us to compute energies far beyond the point where the Gutzwiller trace formula no longer resolves individual individual eigenvalues as individual peaks. In Fig. (6.15b) we have computed over 100 eigenvalues, whereas in Fig. (6.10) only 22 eigenvalues were computable.

The energy eigenvalues computed for the 60° wedge (Figs. (6.15b,d)) show excellent agreement with the exact quantum eigenvalues. The first 40 eigenvalues are clustered between 0% and +20% of the mean level spacing. Even near eigenvalue 100 the spread is just ±20%.

The energy eigenvalues computed for the 49° wedge (Figs. (6.16b,c) show a

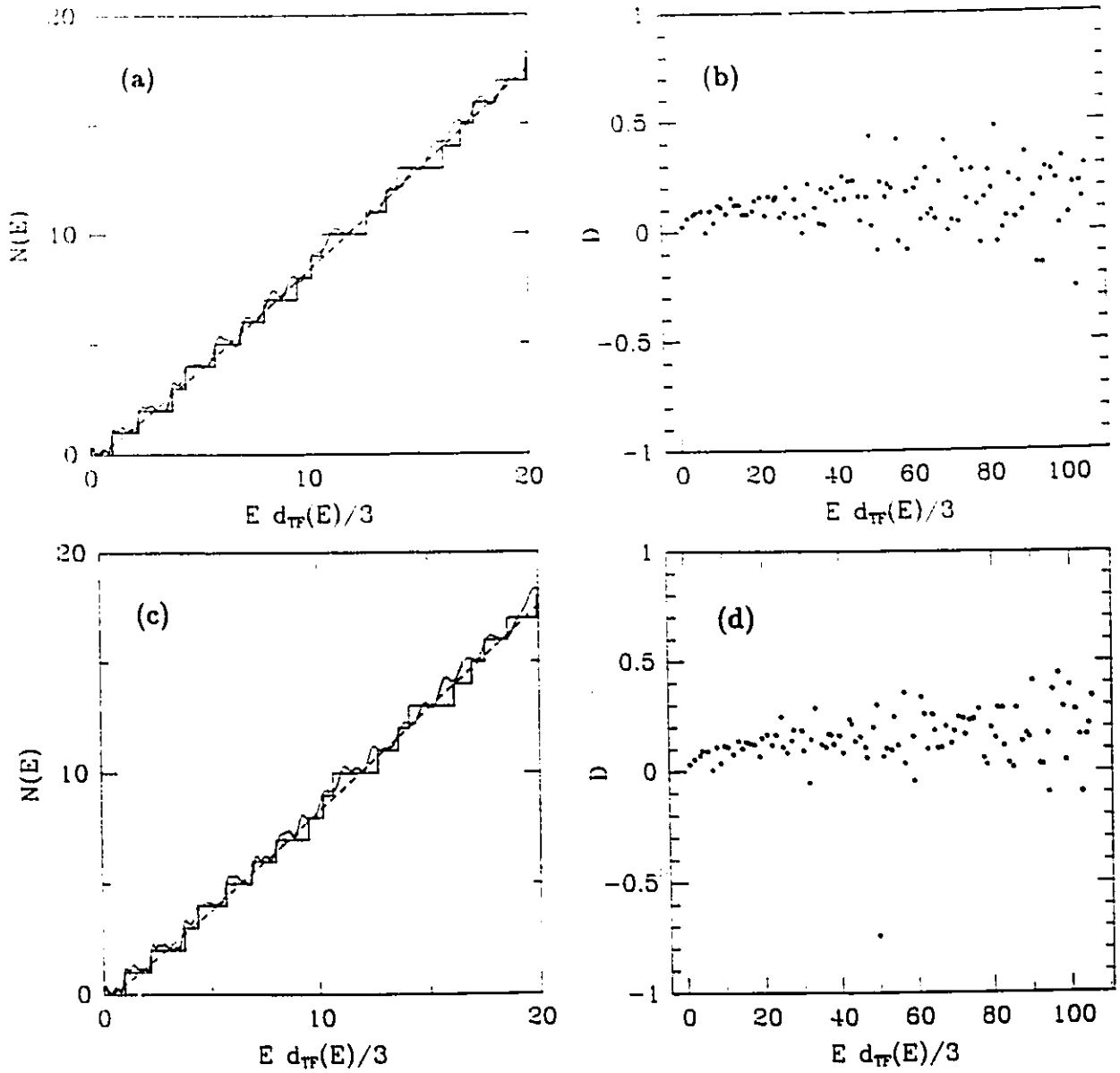

Figure 6.15: (a) The semiclassical staircase, $N_{SC}(E)$, smooth solid curve. The exact quantum staircase, stepped solid curve. The Thomas–Fermi curve, $N_{TF}(E)$, dashed curve. The horizontal axis has been scaled so that the asymptotic spacing between the eigenvalues is 1. The wedge angle is 60° and 257 periodic orbits with $S_\gamma \leq 12.0$ and word lengths $n \leq 16$ were used to generate $N_{SC}(E)$. (b) The difference between the exact quantum energies and the energies calculated from the quantization condition described in the text plotted against the exact quantum energy (in scaled units). (c) The legend for the curves is the same as in (a). 1621 periodic orbits with $S_\gamma \leq 19.42$, which corresponds to all periodic orbits with word lengths $n \leq 15$ and several hundred with word lengths of 16, were used to generate $N_{SC}(E)$. (d) The difference between the exact quantum energies and the energies calculated from the quantization condition described in the text plotted against the exact quantum energy (in scaled units).

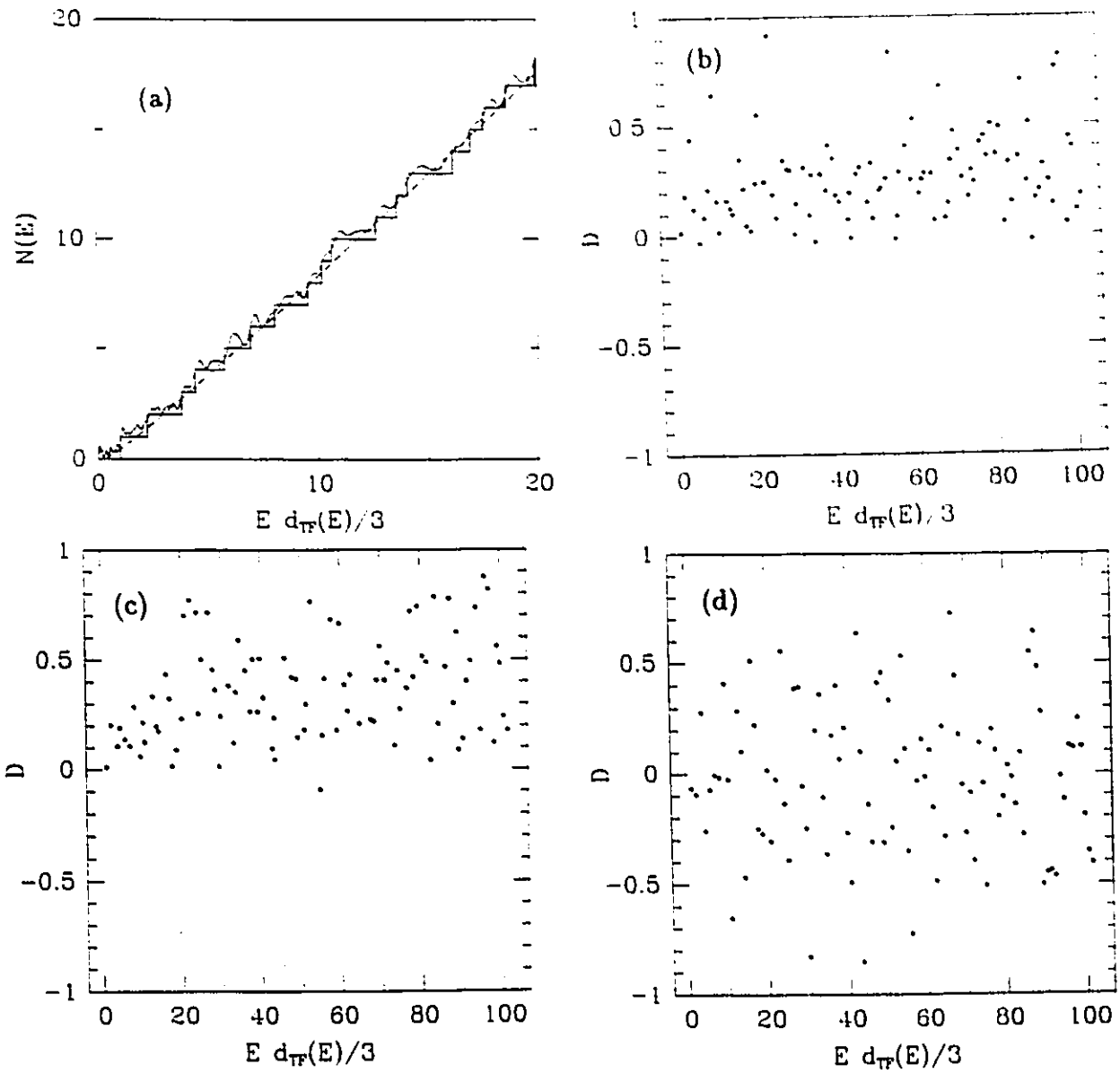

Figure 6.16: (a) The semiclassical staircase, $N_{SC}(E)$, smooth solid curve. The exact quantum staircase, stepped solid curve. The Thomas–Fermi curve, $N_{TF}(E)$ dashed curve. The horizontal axis has been scaled so that the asymptotic spacing between the eigenvalues is 1. The wedge angle is 49° and 271 periodic orbits with $S_\gamma \leq 12.0$ and word lengths $n \leq 19$ were used to generate $N_{SC}(E)$. (b) The difference between the exact quantum energies and the energies calculated using staircase quantization with 271 periodic orbits having $S_\gamma \leq 12.0$ and word lengths $n \leq 19$, (from (a)), plotted against the exact quantum energy (in scaled units). (c) Same as (b) except using 1048 orbits with $S_\gamma \leq 19.48$, which corresponds to all periodic orbits with word length $n \leq 19$. (d) The difference between the Thomas–Fermi energies and the exact quantum energies for the 49° wedge.

fair agreement with the exact quantum eigenvalues. The agreement is better for the low eigenvalues and deteriorates as one goes to higher energy. The first 20 eigenvalues are predicted in Fig. (6.16c) to between about 0% to 30%. To see how good these predictions are we compare Fig. (6.16c) with Fig. (6.16d). Fig. (6.16d) shows the difference between the Thomas–Fermi energies (for the 49° wedge) and the exact quantum energies. A very similar plot results for the 60° wedge. Note the large scatter, even for the low lying eigenvalues. In contrast, Figs. (6.16b,c) have much less scatter and it is obvious that the addition of the periodic orbits is greatly improving the prediction of the energies. Nonetheless, the results for the 49° wedge are rather disappointing when compared to those for the 60° wedge.

6.7 The dynamical zeta function

We here evaluate numerically the dynamical zeta function given in Sec. (3.2.3).

Figs. (6.17, 6.18) show evaluations of the magnitude of the product $Z(E)$ from Eq. (3.36) for the 60° and 49° wedges respectively. The semiclassical eigenvalues should correspond to the minima of the solid curve, as described in Sec. (3.2.3).

Upon comparison with Figs. (6.11, 6.14) one can see that the dynamical zeta function, expressed as a product, suffers from the same shortcomings as the Gutzwiller trace formula. Almost every minimum below $|Z(E)| < 1$ in the 60° wedge corresponds to an eigenvalue, however there are many spurious minima in the case

of the 49° wedge. Note that even the two very closely spaced peaks we pointed out near the 4^{th} eigenvalue in Fig. (6.14) reappear in Fig. (6.17) as two closely spaced minima.

The dynamical zeta function expressed as a Dirichlet series, Eq. (3.38) is plotted in Fig. (6.19).The pseudo orbits we have used in the Dirichlet series have been truncated by word length, rather than action. The truncation by action was used by Berry and Keating 1990, and Sieber and Steiner 1992. However, because of the infinity of periodic orbits below the accumulating action of the non–isolated families the truncation by action would have resulted in an arbitrary cutoff of the non–isolated families in the construction of the pseudo orbits. Such a problem does not arise when truncating pseudo orbits by word length and so this was the preferred method.

As one can see from Fig. (6.19) the Dirichlet series form of the dynamical zeta function gives results similar to the product form of the dynamical zeta function. The main differences are the sharper (and in many cases lower) minima produced by the Dirichlet series form, and the extra minima produced near eigenvalues 9, 13, and 17. Again, as with the product form of $Z(E)$ the minima are not in one–to–one correspondence with the eigenvalues. These results for the Dirichlet series form of the dynamical zeta function are similar to those obtained by Sieber (1991).

Finally, we examine the third form of the dynamical zeta function, the cycle expansion proposed in Eqs. (3.43-3.46). We have found that for the 49° wedge with

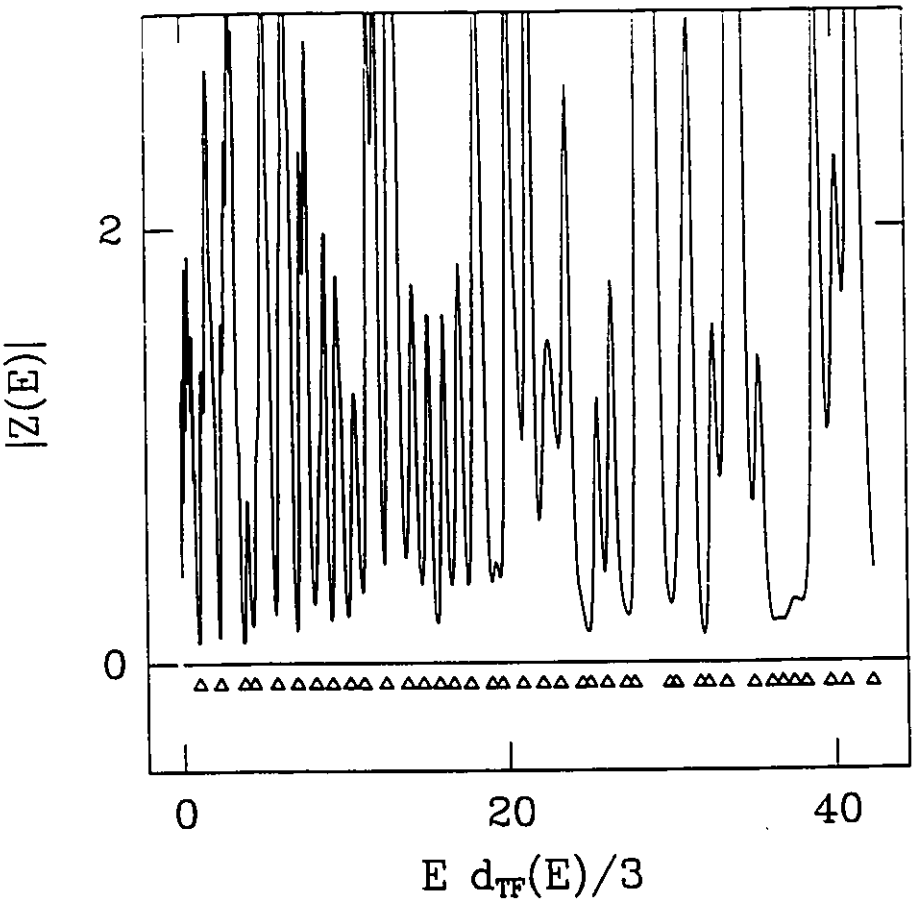

Figure 6.17: A plot of the magnitude of the dynamical zeta function (solid curve), expressed as a product, Eq. (3.36), with $k = 0, \ldots 9$. The upper vertices of the small triangles mark the positions of the exact quantum eigenvalues. The wedge angle is 60° and 1621 orbits, corresponding to a maximum action of $S_\gamma = 19.42$ and all words with $n \leq 15$ and several hundred with $n = 16$, were used in the product. The vertex orbit was taken into account in the product by including the limiting orbits TVV and $TTTV$; each contributing with a square root relative to all the other periodic orbits. The horizontal axis has been scaled to make the asymptotic spacing between energy eigenvalues equal to 1.

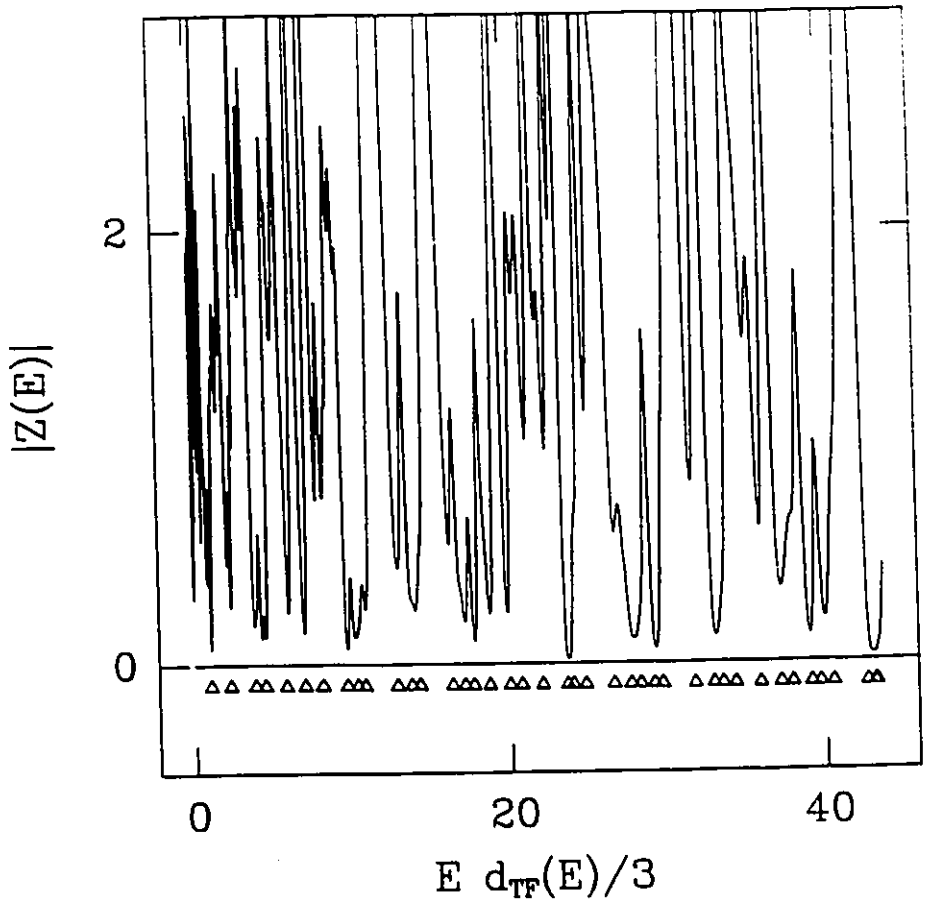

Figure 6.18: A plot of the magnitude of the dynamical zeta function (solid curve), expressed as an product, Eq. (3.36), with $k = 0, \ldots 9$. The upper vertices of the small triangles mark the positions of the exact quantum eigenvalues. The wedge angle is 49° and 1048 orbits, corresponding to a maximum action of $S_7 = 19.48$ and all words with $n \leq 19$ were used in the product. The horizontal axis has been scaled to make the asymptotic spacing between energy eigenvalues equal to 1.

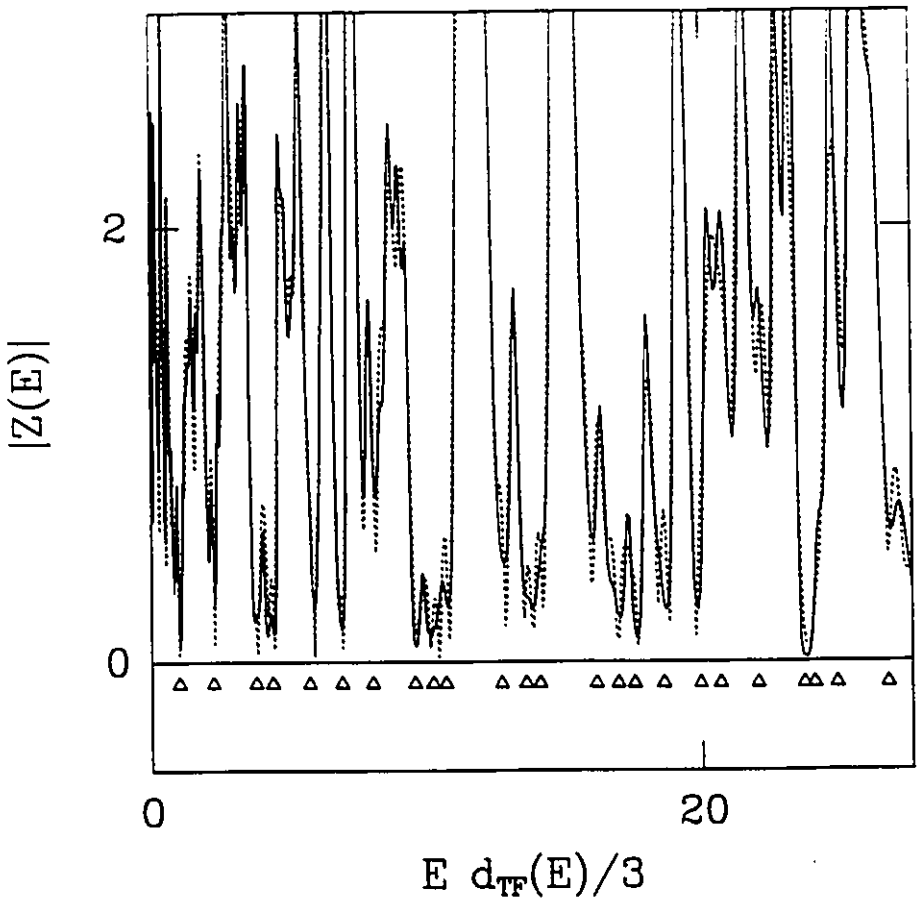

Figure 6.19: A plot of the magnitude of the dynamical zeta function expressed as a product (solid curve) and as a Dirichlet series (dotted curve). The upper vertices of the small triangles mark the positions of the exact quantum eigenvalues. The wedge angle is 49° and 1048 periodic orbits with word length $n \leq 19$ were used in computing the solid curve. The 1048 periodic orbits with $n \leq 19$ were used to construct 26706 pseudo orbits with $n \leq 19$. The result of evaluating the Dirichlet series using these 26707 pseudo orbits is shown by the dotted curve.

1048 periodic orbits with word length $n \leq 19$ there are 162 fundamental terms and 886 curvature terms. That is, 886 of the periodic orbits could be paired off with products of other orbits. This pairing off was not unique however, and could have been done in many ways. As an example, the orbit $TVVTVVVV$ could have been paired off with either the combination $TVVTVVV+V$ or $TVV+TVVVV$. Similarly, $TVTVTVVV$ could be paired off with $TVTVTVV+V$ or $TV+TVTVVV$. In our numerical work we arbitrarily choose one of these many possible pairings.

An evaluation of $Z(E)$ using the cycle expansion, Eqs. (3.43-3.46), in the 49° wedge is shown in Fig. (6.20). As with the Dirichlet series, the cycle expansion produces more numerous and sharper minima compared to the product form of $Z(E)$. Again, there is no one–to–one correspondence between minima and eigenvalues.

6.8 Functional Relations: Results

Here we examine the function derived in Sec. (3.2.5), namely Eq. (3.53). We reproduce Eq. (3.53) here for convenience.

$$f(E) = Z^*(0)Z(E)e^{-i\pi N_{TF}(E)} \tag{6.27}$$

The quantization condition for the semiclassical energies E_n is expressed by $f(E_n) = 0$.

Because of the semiclassical approximations used in deriving the Gutzwiller

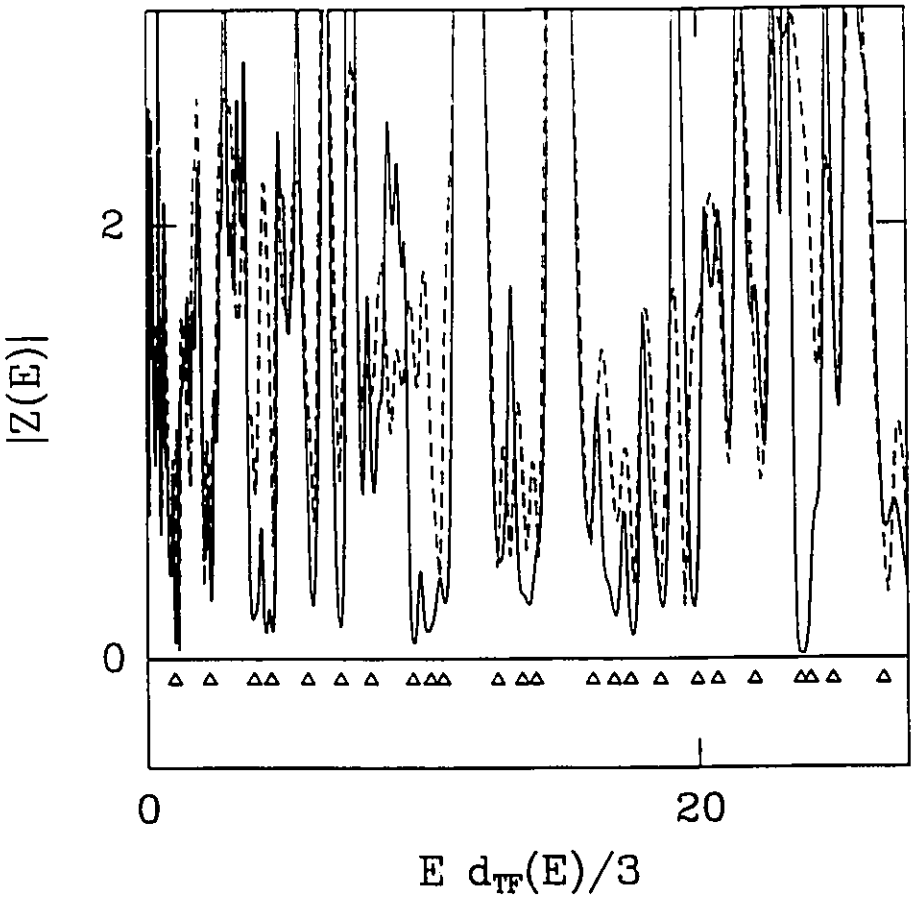

Figure 6.20: $Z(E)$ evaluated for the cycle expansion form, Eqs. (3.43-3.46), in the 49° wedge (dotted line) in comparison with $Z(E)$ evaluated as a product, Eq. (3.36) (solid line). 1048 periodic orbits were used in the product form of $Z(E)$, with $k = 0, \ldots 9$. The same 1048 periodic orbits were used in the curvature expansion which resulted in 162 fundamental terms and 886 curvature terms. $k = 0, \ldots 9$ was used in evaluating the curvature form of $Z(E)$.

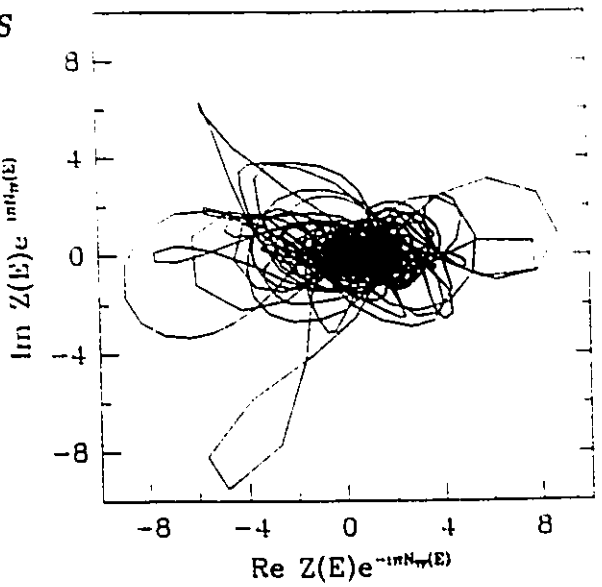

Figure 6.21: A plot of $\mathrm{Im}Z(E)\exp(-i\pi N_{TF}(E))$ vs $\mathrm{Re}Z(E)\exp(-i\pi N_{TF}(E))$ for the 49° wedge using 271 periodic orbits with $S_\gamma \leq 12.0$ and word length $n \leq 19$, over the energy range $0 \leq E \leq 15.55$ and the product form of $Z(E)$, Eq. (3.36), with $k = 0, \ldots 9$. This energy range corresponds to a range encompassing the first 103 energy eigenvalues.

trace formula we do not expect $f(E)$ to be exactly real for real E. Nonetheless, a plot of $\mathrm{Im}f(E)$ vs $\mathrm{Re}f(E)$ with E as a parameter should show that $f(E)$ has a small imaginary part relative to its real part.

A plot of $\mathrm{Im}Z(E)\exp(-i\pi N_{TF}(E))$ vs $\mathrm{Re}Z(E)\exp(-i\pi N_{TF}(E))$ is shown in Fig. (6.21) for the product form of $Z(E)$. Notice how the plot is much more concentrated along the real axis than the imaginary axis. This implies that $Z^*(0)$ is approximately real, and that the function $f(E)$ is indeed approximately real. Hence we can re-write our quantization condition as

$$f(E) = Z(E)\exp(-i\pi N_{TF}(E)) \qquad \mathrm{Re}f(E_n) = 0. \tag{6.28}$$

In Fig. (6.22a) we have plotted $\mathrm{Re}Z(E)\exp(-i\pi N_{TF}(E))$ vs $Ed_{TF}(E)/3$ for the 60° wedge and the product form of $Z(E)$, using only the 3 shortest periodic orbits, V, TV, and TTV. Fig. (6.22b) is a plot of the difference between exact quantum eigenvalues and the zeroes of $\mathrm{Re}Z(E)\exp(-i\pi N_{TF}(E))$. Upon comparison with Fig (6.10) we see that inputting only 3 periodic orbits we are able to obtain the same accuracy using the quantization condition Eq. (6.28) as we could with the Gutzwiller trace formula inputting 257 periodic orbits. This is a truly remarkable improvement. If we use 257 periodic orbits (the same number of periodic orbits as was used to generate Fig. (6.10)) then Figs. (6.22c,d) result. From (6.22d) we see that about 40 eigenvalues can be predicted to withing ±10% of the mean level spacing and that even near the 100^{th} eigenvalue the scatter is only about ±20% of the mean level spacing. Adding more periodic orbits, Figs. (6.22e,f) improves the predicted eigenvalues even more.

The results for the 49° wedge are also very good compared to the other quantization schemes. Using only the three shortest periodic orbits, V, TV, TVV and the product form of $Z(E)$, we find that the first 20 eigenvalues can be predicted to within ±20% of the mean level spacing (see Figs. (6.23a,b)). Figs. (6.23c,d) show the results of an evaluation using 271 periodic orbits and Figs. (6.23e,f) show the results of an evaluation using 1048 periodic orbits. The first 15 eigenvalues are predicted to within about ±15% of the mean level spacing and the first 100 to within about ±20% of the mean level spacing.

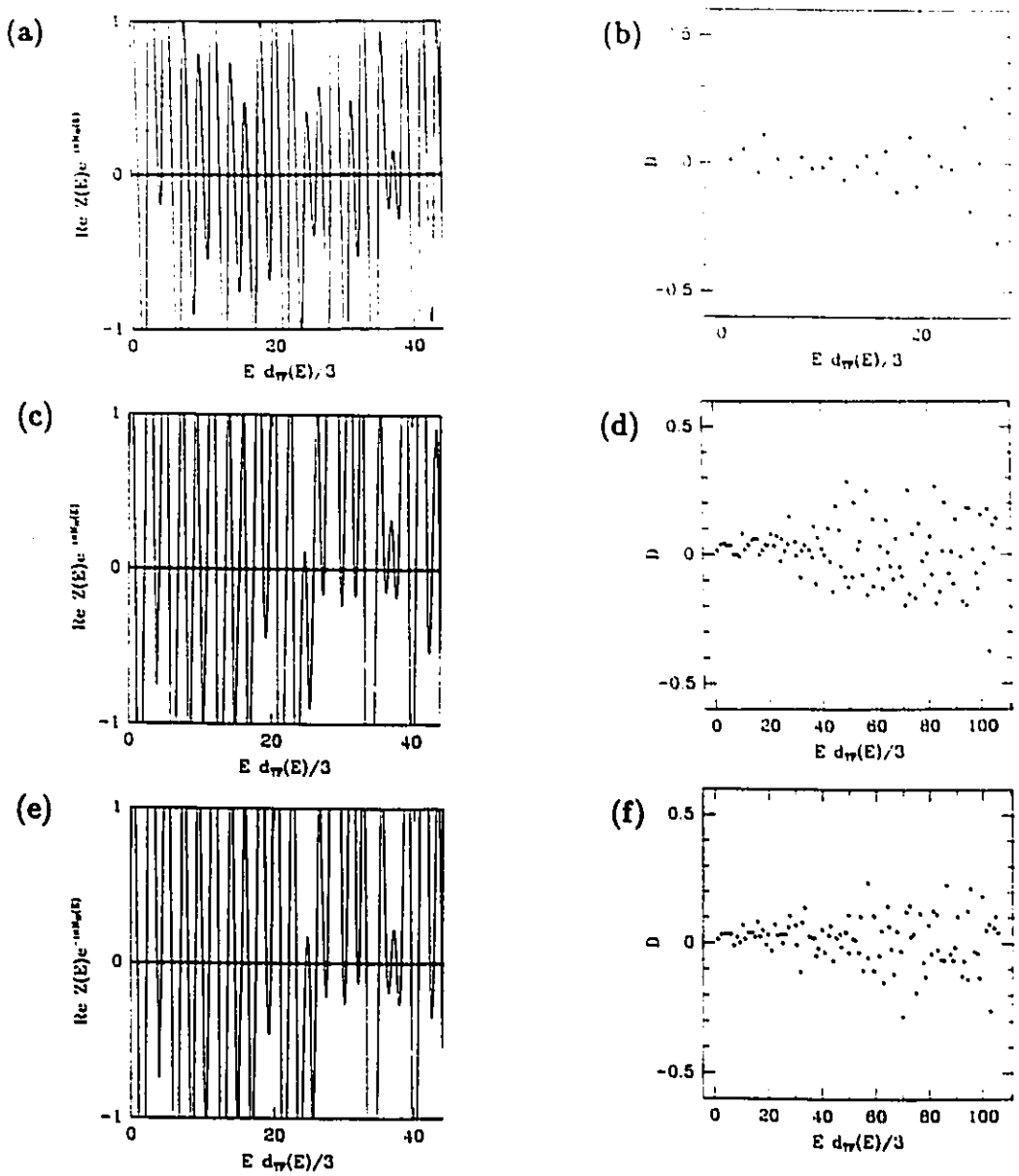

Figure 6.22: (a) An evaluation of $\mathrm{Re}Z(E)\exp(-i\pi N_{TF}(E))$ vs $Ed_{TF}(E)/3$ for the 60° wedge using the three shortest orbits V, TV, and TVV. $Z(E)$ is calculate using the product form Eq. (3.36) with $k = 0,\ldots 9$. The exact quantum energies are shown as solid dots. (b) The difference between the exact quantum eigenvalues and the eigenvalues computed from the zeroes of (a). (c) Same as (a) except using 257 periodic orbits with $S_\gamma \leq 12.0$ and word lengths $n \leq 16$. (d) The difference between the exact quantum eigenvalues and the eigenvalues computed from the zeroes of (c). (e) Same as (a) except using 1621 periodic orbits with $S_\gamma \leq 19.42$ which corresponds to all periodic orbits with word length $n \leq 15$ and several hundred with word length $n = 16$. (f) The difference between the exact quantum eigenvalues and the eigenvalues computed from the zeroes of (e).

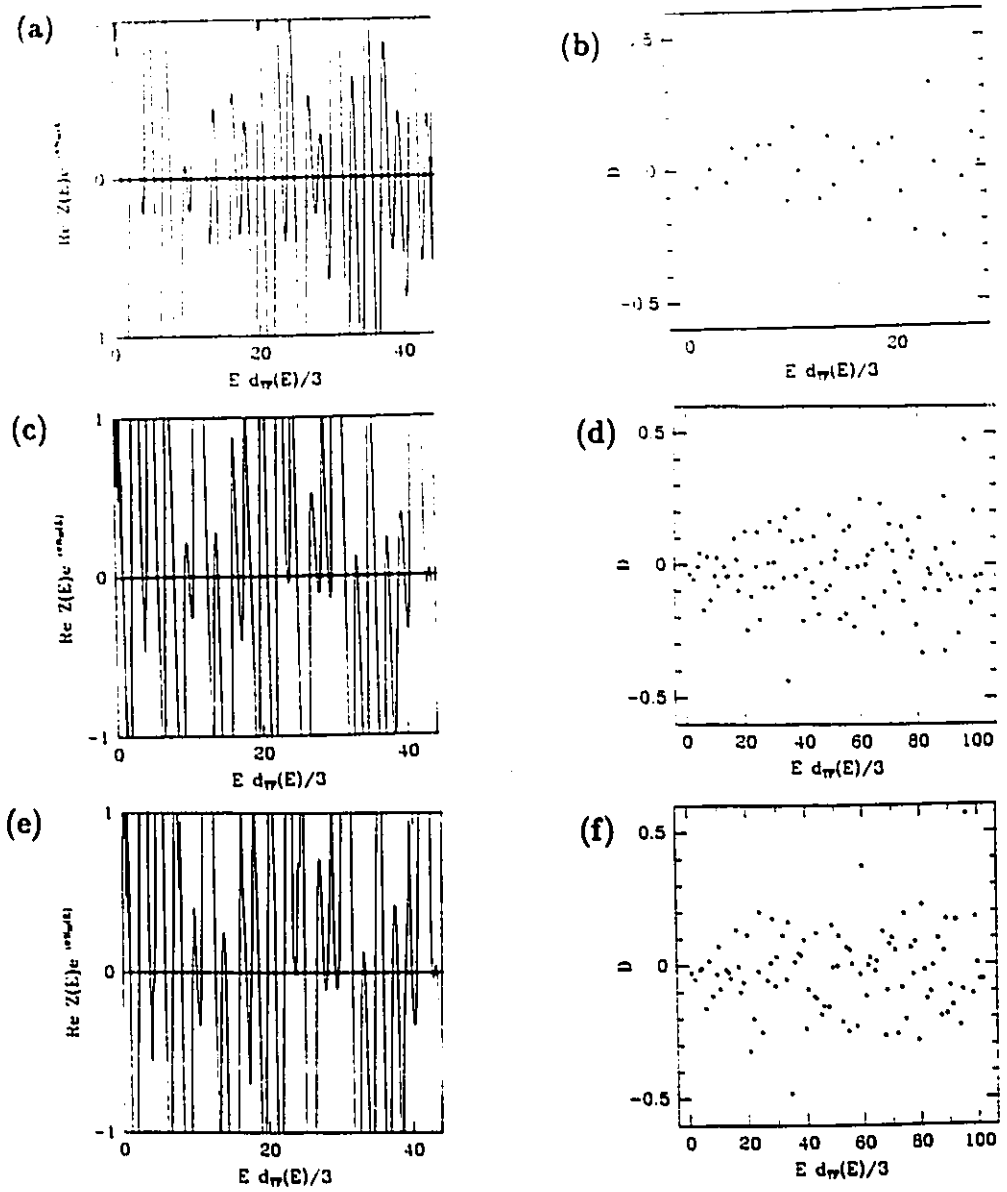

Figure 6.23: (a) An evaluation of $\mathrm{Re}Z(E)\exp(-i\pi N_{TF}(E))$ vs $Ed_{TF}(E)/3$ for the 49° wedge using the three shortest orbits V, TV, and TVV. $Z(E)$ is calculate using the product form of $Z(E)$, Eq. (3.36), with $k = 0, \ldots 9$. The exact quantum energies are shown as solid dots. (b) The difference between the exact quantum eigenvalues and the eigenvalues computed from the zeroes of (a). (c) Same as (a) except using 271 periodic orbits with $S_\gamma \leq 12.0$ and word lengths $n \leq 19$. (d) The difference between the exact quantum eigenvalues and the eigenvalues computed from the zeroes of (c). (e) Same as (a) except using 1048 periodic orbits with $S_\gamma \leq 19.48$ which corresponds to all periodic orbits with word length $n \leq 19$. (f) The difference between the exact quantum eigenvalues and the eigenvalues computed from the zeroes of (e).

The results of using the quantization condition, Eq. (6.28), and the Dirichlet series form of the dynamical zeta function, Eq. (3.38), are not as good as those obtained using the product form of the dynamical zeta function, Eq. (3.36). Fig. (6.24a,b) shows a comparison between the results obtained using the Dirichlet series form of $Z(E)$ and the product form of $Z(E)$. As one can see, the curve resulting from the Dirichlet series and the curve resulting from the product follow each other closely in many areas but the Dirichlet series form of $Z(E)$ has some spurious zero crossings which don't correspond to eigenvalues (such as near $Ed_{TF}(E)/3 = 4$ in Fig. (6.24b)). As well, the Dirichlet series form of $Z(E)$ misses some eigenvalues altogether (although not in the range shown on the plots). This behaviour of missing eigenvalues continues to higher energies. Because of these features of spurious and missing eigenvalues the Dirichlet series form of the dynamical zeta function does not offer good promise as a quantization tool for the wedge billiard.

The results of using the quantization condition, Eq. (6.28), and the cycle expanded form of the dynamical zeta function, Eqs. (3.43-3.46), are again not as good as those obtained using the product form of the dynamical zeta function, Eq. (3.36). Fig. (6.25a,b) shows a comparison between the results obtained using the cycle expanded form of $Z(E)$ and the product form of $Z(E)$. As before with the Dirichlet series, the curve resulting from the cycle expansion and the curve resulting from the product follow each other closely in many areas but the cycle expansion form of $\mathrm{Re}Z(E)\exp(-i\pi N_{TF}(E))$ has some missing zeroes, and hence fails to predict correctly

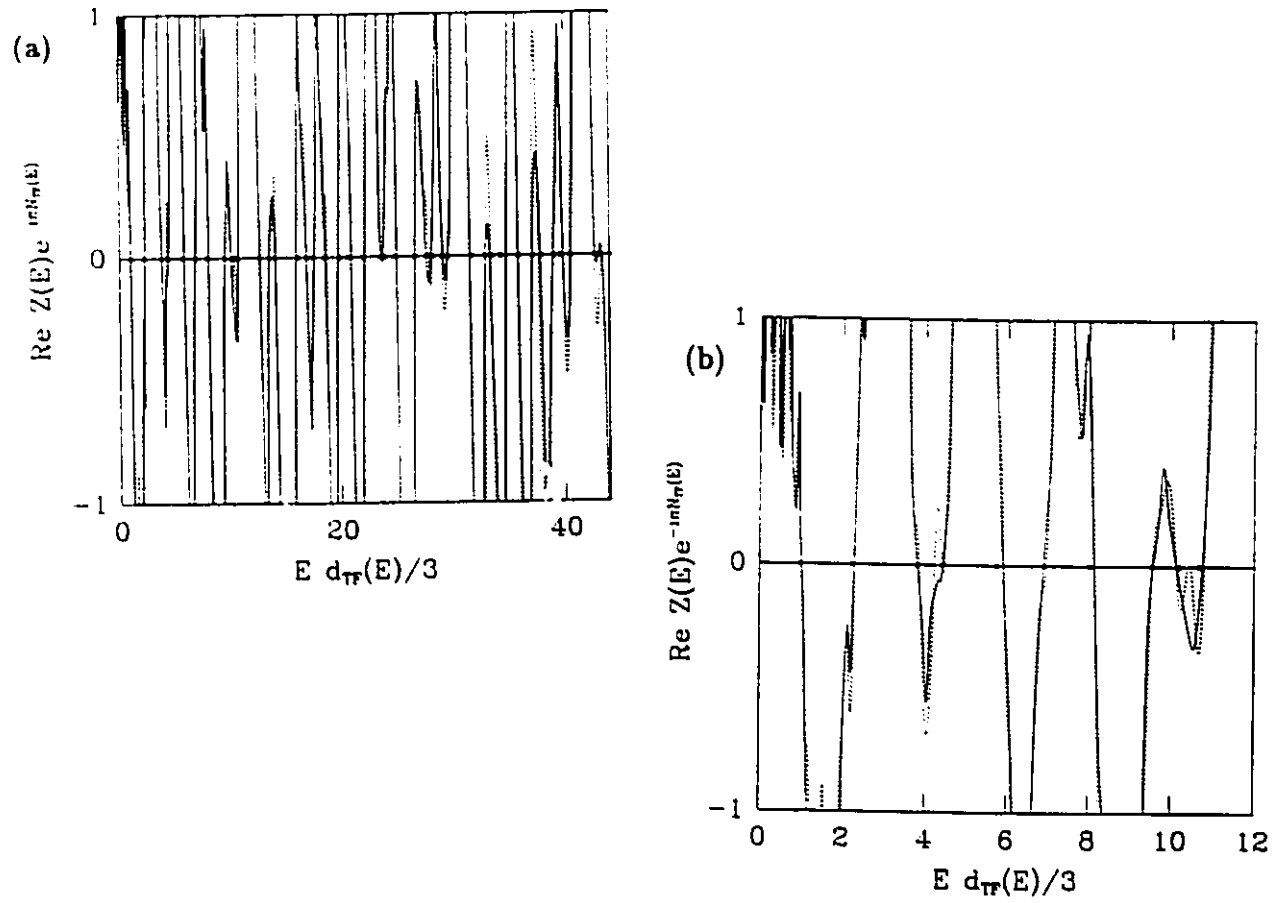

Figure 6.24: (a) An evaluation of $\mathrm{Re}Z(E)\exp(-i\pi N_{TF}(E))$ vs $Ed_{TF}(E)/3$ for the 49° wedge using the product form of $Z(E)$ in which all (1048) periodic orbits with word length $n \leq 19$ have been included (solid curve). The dotted curve is an evaluation using the Dirichlet series form of $Z(E)$ using all (26706) psuedo orbits with word length $n \leq 19$. The positions of the exact quantum energies are marked by solid dots. (b) An expanded horizontal scale version of (a) showing the spurious zero crossings of the Dirichlet series near $Ed_{TF}(E)/3 = 4$ and near $Ed_{TF}(E)/3 = 10$.

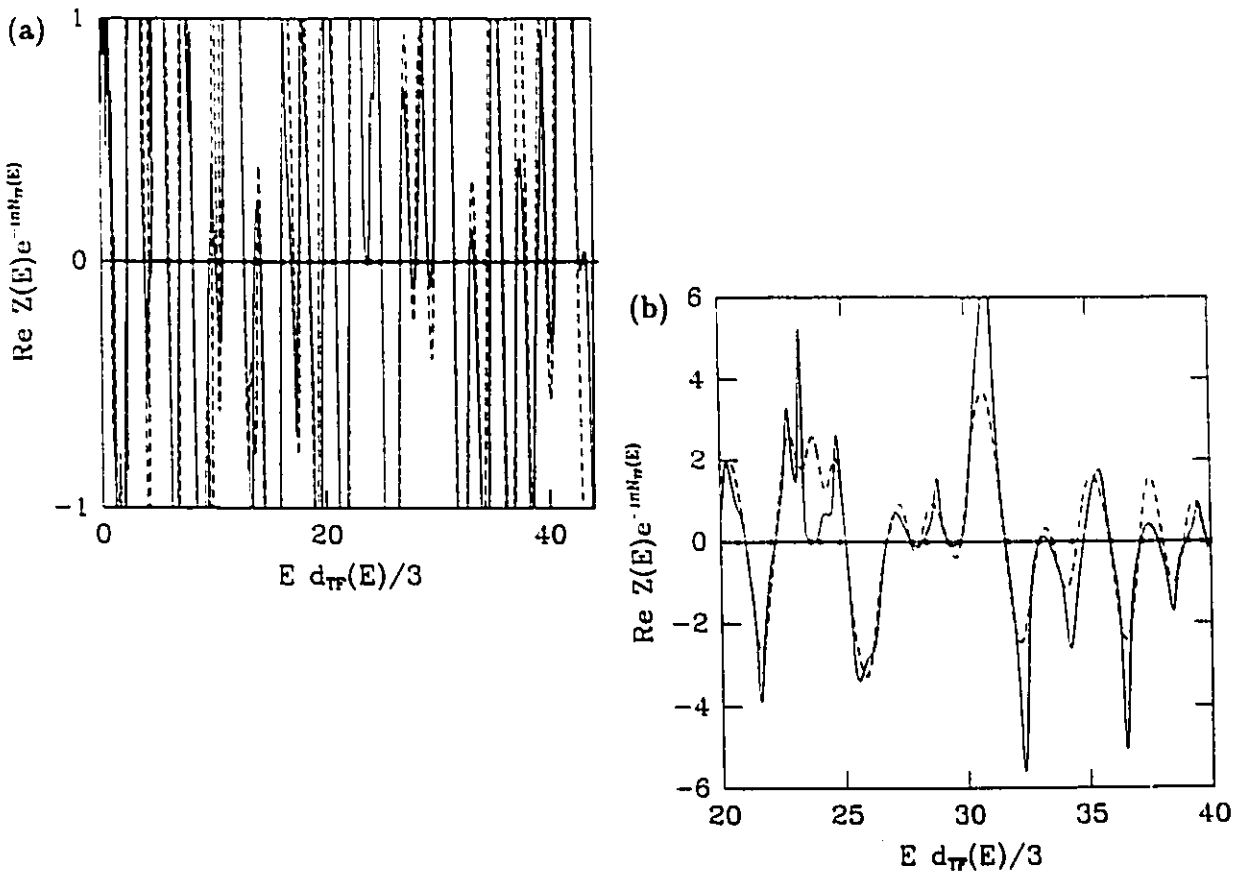

Figure 6.25: (a) An evaluation of $\mathrm{Re}Z(E)\exp(-i\pi N_{TF}(E))$ vs $Ed_{TF}(E)/3$ for the 49° wedge using the product form of $Z(E)$ in which all (1048) periodic orbits with word length $n \leq 19$ have been included (solid curve). The dotted curve is an evaluation using the cycle expansion form of $Z(E)$, Eqs. (3.43-3.46), using all (1048) periodic orbits with word length $n \leq 19$. This resulted in 162 fundamental terms, t_f, and 886 curvature terms t_c. The positions of the exact quantum energies are marked by solid dots. (b) An expanded horizontal and vertical scale version of (a) showing the missing zeroes of the cycle expansion form of $Z(E)$ near $Ed_{TF}(E)/3 = 23$.

the existence of some eigenvalues (such as near $Ed_{TF}(E)/3 = 23$ in Fig. (6.25b)). This behaviour of missing eigenvalues continues to higher energies. Because of this feature of missing eigenvalues the cycle expanded form of the dynamical zeta function (as we have used it in Eqs. (3.43-3.46)) does not offer good promise as a quantization tool for the wedge billiard. Perhaps a more sophisticated cycle expansion, carried to higher order, may do better. However, to implement such an expansion the pruning rules must be known, and at present they are not.

We note that it is not straightforward to implement the Dirichlet series and cycle expanded forms of the dynamical zeta function for the 60° wedge. The complications arise because of the existence of the vertex orbit. When one calculates the Dirichlet series co–efficients from Eq. (3.40) then one needs the u_γ and σ_γ of the orbits which contribute to the pseudo–orbit. From Tab. (5.1) one can see the problem. The vertex orbit is a combination of the limiting forms of the orbits TVV and $TTTV$. One has to assign a σ to the vertex orbit, but which value to choose? $\sigma_{TVV} = -1$ and $\sigma_{TTTV} = 1$. Does one use the average, namely 0? Similar problems arise with the Maslov index u_{vertex}. $u_{TVV} = 13$ and $u_{TTTV} = 14$, does one use the average? When one tries to construct pseudo orbits by word length one is also faced with the problem of assigning a word length to the vertex orbit. Is it of word length 3, as is TVV, or word length 4, as is $TTTV$? A similar problem arises when trying to pair off orbits in the cycle expansion. What is the word for the vertex orbit? Because of these ambiguities, we have chosen not to evaluate the Dirichlet series and cycle

expanded forms of the dynamical zeta function, and have chosen the 49° wedge as our testing ground instead.

In the practical computation of eigenvalues using the quantization condition Eq. (6.28) one would like to be sure that the function $\mathrm{Re}Z(E)\exp(-i\pi N_{TF}(E))$ does not change radically when more periodic orbits are added in the computation of $\mathrm{Re}Z(E)\exp(-i\pi N_{TF}(E))$. One would like 'smooth' convergence of the truncated forms of $\mathrm{Re}Z(E)\exp(-i\pi N_{TF}(E))$ to the asymptotic form of $\mathrm{Re}Z(E)\exp(-i\pi N_{TF}(E))$ which contains an infinity of periodic orbits. By looking at the three different forms of $Z(E)$ (product Eq. (3.36), Dirichlet series Eqs. (3.39,3.40), and cycle expansion Eqs. (3.43-3.46)) and using the fact that the average stability exponent increases linearly with word length (see Fig. (5.9)) we expect that the contributions of periodic orbits with longer word lengths, n, will be exponentially damped at a rate $\exp(-m_\nu n)$. However, as before when we discussed the convergence of the Gutzwiller trace formula in Sec. (6.2), the exponential proliferation of periodic orbits may overwhelm this exponential damping. Since all three forms of $Z(E)$ are derived from the Gutzwiller trace formula and we saw in Sec. (6.2) that the Gutzwiller trace formula is not absolutely convergent we have no a priori reason to believe that $\mathrm{Re}Z(E)\exp(-i\pi N_{TF}(E))$ converges smoothly to some limiting form. This could be especially true of the Dirichlet series form of $Z(E)$, where the word entropy of the pseudo orbits is $\tau_w = 0.475$ for the 49° wedge.

Fig. (6.26) shows an evaluation of $\mathrm{Re}Z(E)\exp(-i\pi N_{TF}(E))$ for the three

different forms of $Z(E)$ we have studied, as more periodic orbits are added. In all three cases the functions seem to be smoothly settling down to some asymptotic limit. While these results are suggestive, they are certainly not a proof that $\mathrm{Re}Z(E)\exp(-i\pi N_{TF}(E))$ exists when an infinity of periodic orbits is used. Nonetheless, in practical terms, the 'settling down' of the function is reassuring when one uses the quantization scheme Eq. (6.28) to compute eigenvalues.

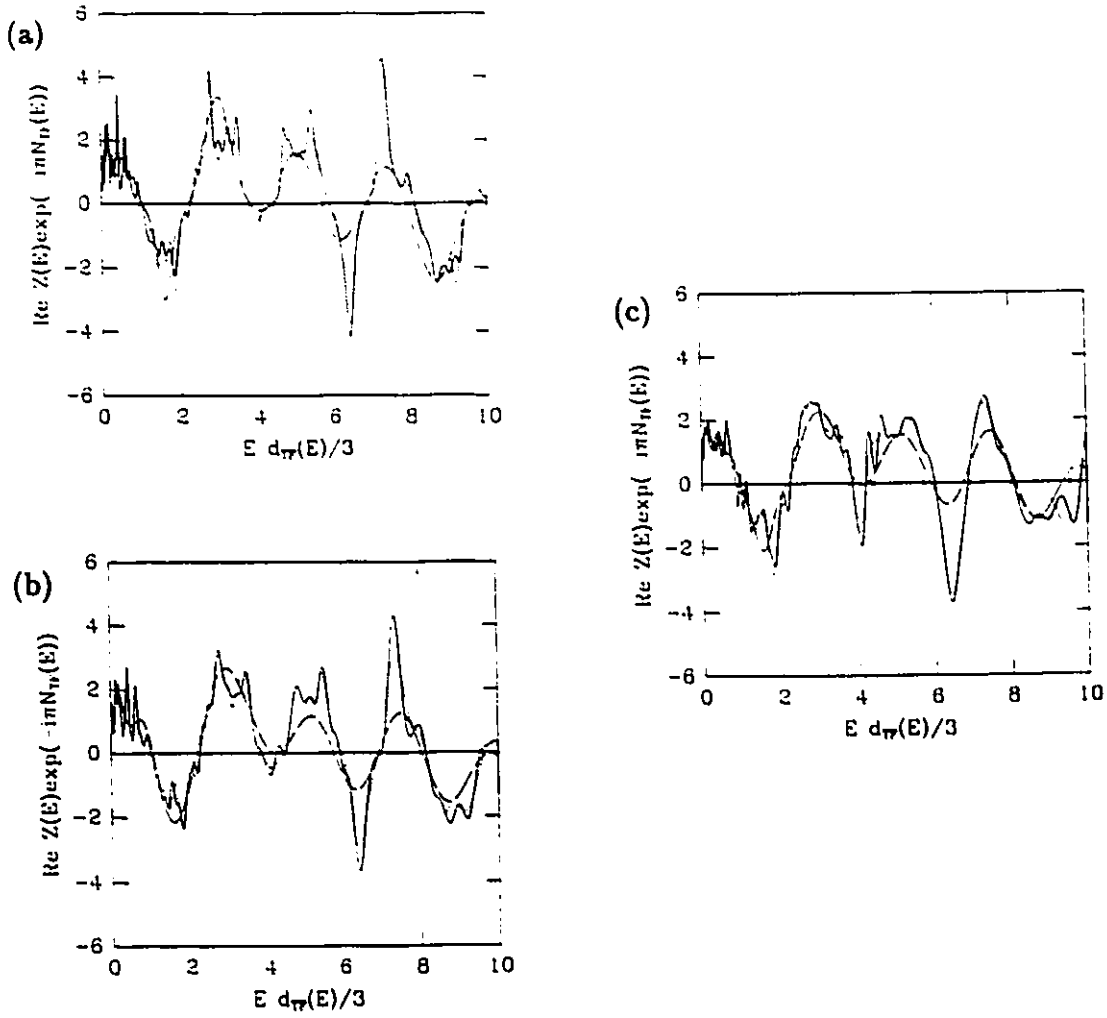

Figure 6.26: An evaluation of $\mathrm{Re}Z(E)\exp(-i\pi N_{TF}(E))$ for the three different forms of $Z(E)$ as more periodic orbits are added. (a) $Z(E)$ in product form Eq. (3.36). 1048 periodic orbits with $S_\gamma \leq 19.48$, which corresponds to all periodic orbits with word length $n \leq 19$ (solid line), 271 periodic orbits with $S_\gamma \leq 12.0$ (short dashed line), 3 periodic orbits with $S_\gamma \leq 2.6$ (long dashed line). (b) $Z(E)$ in Dirichlet series form Eqs. (3.39,3.40). 26706 pseudo orbits with word length $n \leq 19$ (solid line), 902 pseudo orbits with $n \leq 12$ (short dashed line), 6 pseudo orbits with $n \leq 3$ (long dashed line). (c) $Z(E)$ in cylce expanded form Eq. (3.43-3.46). 1048 periodic orbits with word length $n \leq 19$, which corresponds to 162 fundamental terms and 886 curvature terms (solid line), 92 periodic orbits with $n \leq 12$, which corresponds to 16 fundamental terms and 72 curvature terms (short dashed line), 3 periodic orbits with $n \leq 3$ which corresponds to 2 fundamental terms and 1 curvature term (long dashed line).

i	$\tilde{E}_i$	$\tilde{E}_i^{(a)}$	$\tilde{E}_i^{(b)}$	$\tilde{E}_i^{(c)}$	$\tilde{E}_i^{(d)}$	$\tilde{E}_i^{(e)}$
1	0.9512	0.95	0.94*	0.92	1.02	0.94
2	2.2365	2.21	2.20	2.18	2.27	2.20
3	3.7178	3.68	3.68	3.64	3.46	3.68
4	4.3183	4.27	4.25	4.22	4.61	4.28
5	5.7073	5.66	5.67	5.62	5.74	5.67
6	6.9338	6.94	6.94	6.93	6.85	6.94
7	8.0678	7.99	8.02	7.96	7.96	8.04
8	9.0658	9.05	9.05	9.03	9.06	9.06
9	10.1264	10.03	10.03	10.01	10.15	10.06
10	10.9532	10.95	10.92	10.84	11.24	10.94
11	12.2992	12.25	12.25	12.22	12.32	12.26
12	13.6340	13.56	13.58	13.49	13.40	13.59
13	14.6001	14.56	14.56	14.50	14.47	14.57
14	15.5918	15.49	15.49	15.46	15.55	15.51
15	16.4728	16.38	16.39	16.35	16.62	16.45
16	17.5404	17.47	17.46	17.42	17.68	17.49
17	18.8873	18.87	18.93	18.82	18.75	18.89
18	19.5368	19.54	19.46	19.38	19.81	19.50
19	20.8167	20.94		20.65	20.87	20.85
20	22.0833	21.89	21.93	21.96	21.93	22.01
21	23.1328	23.17	23.12	22.97	22.99	23.10
22	24.4708	24.26	24.89	24.22	24.05	24.43
23	24.9594	24.94		24.85	25.11	24.96
24	25.9993	25.93	25.91	25.92	26.16	25.96
25	27.1880	27.49	27.33	27.05	27.21	27.12
26	27.6792			27.49	28.27	27.57
27	29.8122	29.85	29.93	29.63	29.32	29.74
28	30.1879			30.09	30.24	30.19
29	31.6872	31.94	31.95	31.74	31.42	31.80
30	32.1754			32.05	32.47	32.11

Table 6.1: The exact scaled energy eigenvalues, $\tilde{E}_i$ (where $\tilde{E}_i = E_i d_{TF}(E_i)/3$), for the 60° wedge compared to the scaled eigenvalues calculated by the various quantization schemes. A '*' means that more than one eigenvalue is predicted by the quantization scheme whereas only one exact eigenvalue exists. In this case the eigenvalue from the quantization scheme closest to the exact eigenvalue is used in the table. $\tilde{E}_i^{(a)}$, the Gutzwiller trace formula, Eq. (3.16). All maxima above height 4.0 in Fig. (6.11). $\tilde{E}_i^{(b)}$), the dynamical zeta function expressed as a product, Eq. (3.36). All minima below 1.0 in Fig. (6.17). $\tilde{E}_i^{(c)}$, staircase quantization, Eq. (6.25), and explanation in Sec. (6.6). Energies calculated from Fig. (6.16c). $\tilde{E}_i^{(d)}$, Thomas–Fermi energies, Eq. (6.26). $\tilde{E}_i^{(e)}$, the functional relation, Eq. (6.28), along with the product form of the dynamical zeta function, Eq. (3.36). Energies calculated from zeroes of Fig. (6.22e).

6.9 Summary

Using a large matrix diagonalization we have accurately calculated the first 300 eigenvalues for the 49° wedge and 200 eigenvalues for the 60° wedge.

The nearest neighbour statistics for the 45°, 49°, and 60° wedges show Poisson, Wigner, and Wigner distributions respectively, in agreement with previous studies on other systems and theoretical predictions.

Using the scaling properties of the classical periodic orbits it was found that the Gutzwiller trace formula is not absolutely convergent for the 49° and 60° wedges. However, conditional convergence is still possible and the results from the quantization schemes seem to indicate that useful results can still be obtained.

The non–isolated families of orbits found in the wedge billiard manifest themselves as deviations between the classical and quantum curves (Figs. (6.7, 6.8)). near the accumulating actions of the families. We have shown that the Gutzwiller trace formula cannot be used for these families and hence that these discrepancies are expected.

Using damped sine and cosine transforms of the density of states we are able to infer the actions, periods, stability exponents and Maslov indices of at least the shortest periodic orbits using only the information contained in the quantum eigenvalues.

Finally, several quantization schemes are discussed. Each scheme uses as in-

put information about the classical periodic orbits to compute the energy eigenvalues. Of the quantization schemes considered the best results arose from the functional relation, Eq. (6.28), where $Z(E)$ is given by a product, Eq. (3.36). This conclusion was also reached by Siever 1992. Tanner and Wintgen 1992 also found that the functional relation, Eq. (6.28), gave the best results. However, in their case the pruning rules were known and a cycle expanded form of $Z(E)$ was used.

i	$\tilde{E}_i$	$\tilde{E}_i^{(a)}$	$\tilde{E}_i^{(b)}$	$\tilde{E}_i^{(c)}$	$\tilde{E}_i^{(d)}$	$\tilde{E}_i^{(e)}$	$\tilde{E}_i^{(f)}$	$\tilde{E}_i^{(g)}$
1	0.9896	1.02*	1.02*	0.98	1.05	1.02	1.01	1.00*
2	2.2240	2.29*	2.29*	2.02	2.32	2.27	2.28	2.27
3	3.7872	3.72*	3.76	3.68	3.51	3.80	3.85	3.88
4	4.4004	4.48*	4.45*	4.21	4.66	4.41	4.39*	4.22
5	5.7202	5.91	5.91	5.58	5.79	5.88	5.91	6.01
6	6.9076	6.92	6.91	6.80	6.91	6.89	6.96	6.88
7	8.0057	8.13*	8.13*	7.72	8.02	8.12	8.14	8.07
8	9.5352	9.56	9.58	9.47	9.12	9.57	9.55	9.84
9	10.1930	10.29*	10.07	9.98	10.22	10.12	10.11	10.27
10	10.6559	10.77	10.73	10.53	11.31	10.74	10.78*	10.52
11	12.6836	12.68	12.79	12.35	12.39	12.70	12.81	12.68
12	13.5809	13.51	13.84	13.38	13.48	13.61	13.54	13.87
13	14.0866	13.87*		13.91	14.55	14.14	14.20	14.18
14	16.1415	16.02*	16.03	15.71	15.63	16.01	15.99	16.02
15	16.9275	17.02	17.00	16.60	16.70	16.93	16.93	17.16
16	17.5214	17.63	17.62	17.50	17.77	17.62	17.68	17.70
17	18.5669	18.69	18.66	18.48	18.84	18.63	18.80	18.61
18	19.9222	19.81	19.81	19.69	19.90	19.81	19.74	19.46
19	20.6618	21.15		19.96	20.97	20.98	20.94	21.00
20	22.0040	22.39*	22.38	21.23	22.03	22.20	22.09	22.18
21	23.6459	23.70	23.72	22.93	23.09	23.67	23.69	
22	24.0121	24.34		23.75	24.15	23.81	23.83	
23	24.8151	25.05		24.31	25.21	25.07	25.09	25.06
24	26.6483	26.69	26.77	25.93	26.26	26.70	26.67	26.73
25	27.7123	27.89	27.92	27.26	27.32	27.70	27.94	27.68
26	28.3157	28.31		27.95	28.37	28.14	28.25	28.07
27	29.1766	29.27	29.28	29.16	29.42	29.25	29.16	29.21
28	29.6487			29.40	30.48	29.61	29.62	29.76
29	31.7285	31.59	31.62	31.34	31.53	31.61	31.57	31.57
30	32.9406	33.03	33.09	32.82	32.58	32.99	33.01	32.98

Table 6.2: The exact scaled energy eigenvalues, $\tilde{E}_i$ (where $\tilde{E}_i = E_i d_{TF}(E_i)/3$), for the 49° wedge compared to the scaled eigenvalues calculated by the various quantization schemes. A '*' means that more than one eigenvalue is predicted by the quantization scheme whereas only one exact eigenvalue exists. In this case the eigenvalue from the quantization scheme closest to the exact eigenvalue is used in the table. $\tilde{E}_i^{(a)}$, the Gutzwiller trace formula, Eq. (3.16). All maxima above height 2.0 in Fig. (6.14). $\tilde{E}_i^{(b)}$, the dynamical zeta function expressed as a product, Eq. (3.36). All minima below 1.0 in Fig. (6.18). $\tilde{E}_i^{(c)}$, staircase quantization, Eq. (6.25), and explanation in Sec. (6.6). $\tilde{E}_i^{(d)}$, Thomas–Fermi energies, Eq. (6.26). $\tilde{E}_i^{(e)}$, the functional relation, Eq. (6.28), along with the product form of the dynamical zeta function, Eq. (3.36). Energies calculated from zeroes of Fig. (6.23e). $\tilde{E}_i^{(f)}$, the functional relation, Eq. (6.28), along with the Dirichlet series form of the dynamical zeta function, Eqs. (3.38–3.40). The zeroes are calculated from Figs. (6.24a,b). $\tilde{E}_i^{(g)}$, the functional relation, Eq. (6.28), using the cycle expanded form of the dynamical zeta function.

Chapter 7

Overview and Conclusions

This thesis has been about the connections between classical and quantum mechanics in the wedge billiard (as $\hbar \to 0$) via the Gutzwiller formalism. Specifically, we have examined the connection between classical periodic orbits and the energy spectrum.

As a prelude to testing the Gutzwiller formalism one must know the classical periodic orbits (and their characteristic properties) and the quantum energy eigenvalues.

We have conjectured that words formed from the the two letter alphabet T, and V, uniquely label periodic orbits in the wedge billiard. This conjecture was substantiated by the numerical results. Once a unique label was found for a periodic orbit a novel method, using the two-dimensional mappings T and V and the two-dimensional Newton method, worked very well in finding them. A large number of periodic orbits (and their properties) were accurately found. This method may be

easily generalized to other billiard systems as well. It is shown that the classical periodic orbits are heavily pruned (with the pruning depending on the wedge angle) and that they exhibit interesting scaling properties (also dependent on the wedge angle). Interesting families of non–isolated periodic orbits appear in this problem, which have implications for the Gutzwiller formalism. We discuss these implications and show that some discrepancies in the calculated curves may be attributable to the non–isolated families we have found.

The quantum eigenvalues were obtained through large matrix diagonalizations. This method is straightforward to implement and gives good results for large numbers of eigenvalues.

A test of the Gutzwiller formalism, to see if the eigenvalues 'know' about the classical periodic orbits, or conversely, if the periodic orbits can be used to predict the eigenvalues, was undertaken. The results turned out to depend on the wedge angle. The Gutzwiller formalism was very effective for the 60° wedge, and showed that the eigenvalues could be used to predict the classical periodic orbits and that the classical periodic orbits could be used to predict the eigenvalues to relatively high accuracy. However, the results for the 49° wedge were not as good. The quantum eigenvalues could still be used to predict the classical periodic orbits (and vice versa) but with less accuracy than in the case of the 60° wedge.

In terms of finding a quantization condition for chaotic systems the best results were achieved by using a functional relation in conjunction with the product

form of the dynamical zeta function.

The studies undertaken in this thesis have been illuminating, but clearly there is much work which still needs to be done in understanding the connection between a classically chaotic system and its quantum analogue. Further study of the wedge billiard and other systems is encouraged in the hope of shedding light on this fascinating area.

Appendix A

Derivation of the T and V mappings and monodromy matrices

In this appendix we find mappings which take us from initial conditions (X_i, Y_i) just after a collision with the tilted wall to just after the next collision with the tilted wall (X_f, Y_f). The X and Y variables refer to those introduced in Eqs. (4.16, 4.17).

A.1 Derivation of the T and V mappings

The mappings are derived in a straightforward way from the equations of motion for the (x, y, p_x, p_y) variables. We can relate the positions and momenta just after a collision with the tilted wall $(x_i, y_i, p_{xi}, p_{yi})$ to the positions and momenta just before the next collision with the tilted wall $(x'_f, y'_f, p'_{xf}, p'_{yf})$ by

$$x'_f = x_i + p_{xi} t_f \tag{A.1}$$

$$y'_f = y_i + p_{yi}t_f - \frac{t_f^2}{2} \tag{A.2}$$

$$p'_{xf} = p_{xi} \tag{A.3}$$

$$p'_{yf} = p_{yi} - t_f \tag{A.4}$$

$$y_i = x_i \cot\phi_o \tag{A.5}$$

For a T bounce

$$y'_f = x'_f \cot\phi_o. \tag{A.6}$$

Eqns. (A.1–A.6) define a system of equations which may be solved for $(x'_f, y'_f, p'_{xf}, p'_{yf})$ in terms of $(x_i, y_i, p_{xi}, p_{yi})$. Also, the positions and momenta just before a collision with the tilted wall $(x'_f, y'_f, p'_{xf}, p'_{yf})$ may be related to the positions and momenta just after a collision with the tilted wall $(x_f, y_f, p_{xf}, p_{yf})$ via

$$\begin{pmatrix} p_{xf} \\ p_{yf} \end{pmatrix} = \begin{pmatrix} -\cos 2\phi_o & \sin 2\phi_o \\ \sin 2\phi_o & \cos 2\phi_o \end{pmatrix} \begin{pmatrix} p'_{xf} \\ p'_{yf} \end{pmatrix}. \tag{A.7}$$

The result is

$$x_f = x_i + 2p_{xi}p_{yi} - 2p_{xi}^2 \cot\phi_o \tag{A.8}$$

$$y'_f = x_i \cot\phi_o \tag{A.9}$$

$$p_{xf} = [-\cos 2\phi_o + 2\sin 2\phi_o \cot\phi_o]\, p_{xi} - [\sin 2\phi_o]\, p_{yi} \tag{A.10}$$

$$p_{yf} = [\sin 2\phi_o + 2\cos 2\phi_o \cot\phi_o]\, p_{xi} - [\cos 2\phi_o]\, p_{yi} \tag{A.11}$$

For a V bounce things are only slightly more complicated. The V bounce in the half wedge may be considered the reflection in the y-axis of the trajectory which passes from the right tilted wall to the left tilted wall in the full wedge. A trajectory starting out on the right tilted wall and ending up on the left tilted wall in the full wedge has final point given by

$$y_f = -x_f \cot\phi_o. \tag{A.12}$$

Eqns. (A.1–A.5, A.12) may again be solved for $(x'_f, y'_f, p'_{xf}, p'_{yf})$ in terms of $(x_i, y_i, p_{xi}, p_{yi})$. Then to get the half wedge solution we simply reflect the final point in the y-axis $x'_f = -x'_f$ and $p'_{xf} = -p'_{xf}$. Again, using Eq. (A.7) we get for the V bounce

$$x_f = (1/2)\left\{(b - 2p_{xi}^2\cot\phi_o) + \sqrt{(b - 2p_{xi}^2\cot\phi_o)^2 - 4c}\right\} \tag{A.13}$$

$$y_f = \cot\phi_o x_i \tag{A.14}$$

$$p_{xf} = \cos 2\phi_o p_{xi} + \sin 2\phi_o p_{yi} + \sin 2\phi_o \left(\frac{x_f + x_i}{p_{xi}}\right) \tag{A.15}$$

$$p_{yf} = -\sin 2\phi_o p_{xi} + \cos 2\phi_o p_{yi} + \cos 2\phi_o \left(\frac{x_f + x_i}{p_{xi}}\right) \tag{A.16}$$

where

$$b = -2(x_i + p_{xi}p_{yi}) \tag{A.17}$$

$$c = -2(p_{xi}^2 x_i \cot\phi_o - p_{xi}p_{yi}x_i - x_i^2/2) \tag{A.18}$$

Translated into the (X,Y) variables via Eqs. (4.16, 4.17) the T bounce mapping is

$$\begin{aligned} X_f &= X_i + 2Y_i \\ Y_f &= Y_i \end{aligned} \tag{A.19}$$

and the V bounce the mapping is

$$\begin{aligned} X_f &= - X_i - Y_i + Y_f \\ Y_f &= -\sqrt{4 + 2\xi[X_i + Y_i]^2 - Y_i^2}. \end{aligned} \tag{A.20}$$

where

$$\xi = \cos(2\phi_o)\cos^2(\phi_o) \tag{A.21}$$

A.2 Derivation of the 3x3 monodromy matrix

Once the T and V mappings are known it is straightforward to derive the 3x3 monodromy matrix from them. The definition of the 3x3 monodromy matrix M_{3x3} is

given by

$$\begin{pmatrix} \delta x_f \\ \delta p_{xf} \\ \delta p_{yf} \end{pmatrix} = \left(\begin{array}{ccc} \frac{\partial x_f}{\partial x_i} & \frac{\partial x_f}{\partial p_{xi}} & \frac{\partial x_f}{\partial p_{yi}} \\ \frac{\partial p_{xf}}{\partial x_i} & \frac{\partial p_{xf}}{\partial p_{xi}} & \frac{\partial p_{xf}}{\partial p_{yi}} \\ \frac{\partial p_{yf}}{\partial x_i} & \frac{\partial p_{yf}}{\partial p_{xi}} & \frac{\partial p_{yf}}{\partial p_{yi}} \end{array} \right) \Bigg|_{x_i, p_{xi}, p_{yi}} \begin{pmatrix} \delta x_i \\ \delta p_{xi} \\ \delta p_{yi} \end{pmatrix} = M_{3x3}|_{x_i, p_{xi}, p_{yi}} \begin{pmatrix} \delta x_i \\ \delta p_{xi} \\ \delta p_{yi} \end{pmatrix} \quad \text{(A.22)}$$

The 3x3 monodromy matrix relates initial deviations in phase space position away from the central periodic trajectory to final deviations in phase space position away from the central periodic trajectory with the added constraint that the deviations in phase space occur along the tilted wall. Since we are on the tilted wall, $y = (\cot \phi_o)x$ at both the beginning and end points of a bounce so $\delta y = (\cot \phi_o)\ \delta x$. Thus, the monodromy matrix is of dimension 3x3 rather than 4x4 along the tilted wall because if we included y then the row with δy in it would just be $\cot \phi_o$ times the row with δx and the matrix would be singular. Thus there are really only three independent deviations which are possible along the tilted wall and this is reflected in the fact that the monodromy matrix is non–singular when it is of dimension 3x3 rather than 4x4.

Since we know the $(x_f, y_f, p_{xf}, p_{yf})$ as a function of the $(x_i, y_i, p_{xi}, p_{yi})$ via Eqns. (A.7–A.10) for a T mapping and via Eqns. (A.12-A.15) for a V mapping we can calculate this monodromy matrix for a T of V bounce explicitly. Note that the monodromy matrix in Eq. (A.22) is a function of the initial position at which the bounce started (x_i, p_{xi}, p_{yi}). For a T bounce, using Eqns. (A.7–A.10) and Eq. (A.22)

we have

$$M_T = \begin{pmatrix} 1 & 2p_{yi} - 4p_{xi}\cot\phi_o & 2p_{xi} \\ 0 & -\cos 2\phi_o + 2\sin 2\phi_o \cot\phi_o & -\sin 2\phi_o \\ 0 & \sin 2\phi_o + 2\cos 2\phi_o \cot\phi_o & -\cos 2\phi_o \end{pmatrix}. \tag{A.23}$$

From this equation we may verify explicitly that $\det|M| = 1$ as required by a monodromy matrix.

The V monodromy matrix M_V has very complicated matrix elements (arising from the partial differentiations required in Eq. (A.21)) and so we will not display them here. Nonetheless, they are straightforward to program into a computer.

To calculate the 3x3 monodromy matrix for a segment of orbit containing several bounces we must know the sequence of bounces, γ, and where the trajectory strikes the tilted wall at each collision. Then the monodromy matrix for the segment of orbit is simply the product of the monodromy matrices for the individual bounces. As an example, suppose we have the sequence $\gamma = TV$, and the trajectory leaves the tilted wall at the point $(x_1, y_1, p_{x1}, p_{y1})$ before the first T bounce, and at $(x_2, y_2, p_{x2}, p_{y2})$ before the V bounce. Then the monodromy matrix for this sequence of bounces would be

$$M_{TV} = M_V|_{(x_2,y_2,p_{x2},p_{y2})} \cdot M_T|_{(x_1,y_1,p_{x1},p_{y1})}$$

Appendix B

B.1 The Thomas-Fermi Term in the Trace Formula

We will derive the form of the Thomas–Fermi term $d_{TF}(E)$ which appears in the Gutzwiller density of states formula Eq. (3.11).

$$d(E) \approx d_{TF}(E) + d_{OSC}(E) \tag{B.1}$$

One way to arrive at the Thomas–Fermi term for the wedge billiard is suggested by the very beautiful article of Mark Kac '*Can one hear the shape of a drum?*' (Kac, 1966). Kac's approach is quite general and gives the so–called area and perimeter terms for the Thomas–Fermi density of states in a straightforward way.

We start with an approach very similar to that used by Gutzwiller (Gutzwiller, 1971) except that we work with the propagator in the time domain $G(x_b, y_b, x_a, y_a; t)$ rather than its Fourier transformed version $G(x_b, y_b, x_a, y_a; E)$ used in Eq. (2.39).

It can be shown (Schiff, 1968) that the propagator in the time domain is given exactly by

$$\sum_n \psi_n^*(x_a, y_a)\psi_n(x_b, y_b)\exp\left(-\frac{iE_n}{\hbar}t\right) = G(x_b, y_b, x_a, y_a; t) \tag{B.2}$$

Setting $x_b \to x_a = x \quad y_b \to y_a = y$ and integrating over all space gives

$$\sum_n e^{-\frac{iE_n}{\hbar}t} = \int dxdyG(x_b, y_b, x_a, y_a; t)|_{\vec{x}_b \to \vec{x}_a = x}. \tag{B.3}$$

This equation is the time domain analogue of Eq. (3.2). Again, we use the semi-classical propagator on the right hand side of Eq. (B.3) and find that in the limit of $x_b \to x_a = x \quad y_b \to y_a = y$ it splits into two parts

$$\begin{aligned} G_{SC}(x_b, y_b, x_a, y_a; t)|_{\vec{x}_b \to \vec{x}_a = x} &= G_{SC,\, W<<\hbar}(x_b, y_b, x_a, y_a; t)|_{\vec{x}_b \to \vec{x}_a = x} \\ &\quad + G_{SC,\, W>>\hbar}(x_b, y_b, x_a, y_a; t)|_{\vec{x}_b \to \vec{x}_a = x} \end{aligned} \tag{B.4}$$

where (Schulman, 1981)

$$G_{SC}(x_b, y_b, x_a, y_a; t) = -\sum_j \left(\frac{i}{2\pi\hbar}\right)\sqrt{\det\left|\frac{\partial^2 W_j}{\partial \vec{x}_b \partial \vec{x}_a}\right|}\exp\left(i\left[\frac{W_j(x_b, y_b, x_a, y_a; t)}{\hbar} - u_j\frac{\pi}{2}\right]\right). \tag{B.5}$$

$W_j(x_b, y_b, x_a, y_a; t)$ is Hamilton's principal function, defined earlier in Eq. (2.38) and u_j is the phase index for the j^{th} trajectory connecting (x_a, y_a) and (x_b, y_b) in time

t. u_j is incremented by 1 for each focal point or caustic encountered along the path from (x_a, y_a) to (x_b, y_b) and incremented by 2 for each collision with a wall (infinite potential).

As in the derivation of the Gutzwiller trace formula, the term with $W << \hbar$ gives the Thomas–Fermi contribution and the term with $W >> \hbar$ gives the oscillatory contribution to the density of states. We can write Eq. (B.3) as

$$\sum_n e^{-\frac{iE_n}{\hbar}t} \approx d_{TF}(t) + d_{OSC}(t) \tag{B.6}$$

Since we are interested in the Thomas–Fermi term we will henceforth concentrate on it and drop the second term in Eq. (B.6).

$$\sum_n e^{-\frac{iE_n}{\hbar}t} \approx d_{TF}(t) \tag{B.7}$$

Setting

$$s = \frac{it}{\hbar} \tag{B.8}$$

in Eq. (B.7) gives

$$\sum_n e^{-E_n s} \approx d_{TF}(s) \tag{B.9}$$

The left hand side of Eq. (B.9) is just the Laplace transform of the density of states, where s and E are conjugate variables. Thus, the inverse Laplace transform of the right hand side (with respect to s) gives us the Thomas–Fermi contribution to the

density of states $d_{TF}(E)$.

$$d_{TF}(E) = L^{-1} d_{TF}(s) \tag{B.10}$$

We will now evaluate $d_{TF}(s)$ for the wedge billiard.

The limit $W_j << \hbar$ is the same as the limit $t \to 0$ and so we are justified (Schulman, 1981) in using the short time form of W_j given by

$$\begin{aligned} W_j = \int_o^t L dt &= \int_{(x_a,y_a;t_a)}^{(x_b,y_b;t_b)} \left[m\left(\frac{v_x^2 + v_y^2}{2}\right) - gy \right] dt \\ &= \frac{m(y_b - y_a)^2}{2t} - \frac{gt(y_b + y_a)}{2} - \frac{g^2 t^3}{24m} + \frac{m(x_b - x_a)^2}{2t} \end{aligned} \tag{B.11}$$

Then

$$\det \left| \frac{\partial^2 W_j}{\partial \vec{x}_b \partial \vec{x}_a} \right| = \frac{m^2}{t^2} \tag{B.12}$$

and so Eq. (B.5) becomes

$$\begin{aligned} &G_{SC}(x_b, y_b, x_a, y_a; t)|_{\vec{x}_b \to \vec{x}_a = x} = \\ &-\sum_j \left(\frac{i}{2\pi\hbar}\right)\left(\frac{m}{t}\right) \exp\left(\frac{i}{\hbar}\left[\frac{m(y_b - y_a)^2}{2t} - \frac{gt(y_b + y_a)}{2} - \frac{g^2 t^3}{24m} + \frac{m(x_b - x_a)^2}{2t} - iu_j\frac{\pi}{2}\right]\right) \end{aligned} \tag{B.13}$$

Now, for $\vec{x}_b \to \vec{x}_a = \vec{x}$, using the fact that to a first approximation there is only one path $j = 1$ from $\vec{x}_a$ to $\vec{x}_b$ (that of zero length) we get that $(x_b - x_a)^2 = 0$, $(y_b - y_a)^2 = 0$

and $(y_b + y_a) = 2y$ so that

$$G_{SC}(x_b, y_b, x_a, y_a; t)|_{\vec{x}_b \to \vec{x}_a = x} = -\frac{im}{2\pi\hbar t}\exp\left(\frac{-igt}{\hbar}y - \frac{g^2t^3}{24m}\right). \tag{B.14}$$

To leading order in t as $t \to 0$ we may set $\exp(g^2t^3/24m) = 1$. Using Eq. (B.14) in Eq. (B.7) gives

$$\sum_n e^{-\frac{iE_n}{\hbar}t} \approx -\frac{im}{2\pi\hbar t}\int_0^{\frac{y}{\cot\phi}} dx \int_0^\infty dy \exp\left(\frac{-igt}{\hbar}y\right)$$

and setting $s = it/\hbar$ gives

$$\begin{aligned}\sum_n e^{-E_n s} &\approx \frac{m}{2\pi\hbar^2}\frac{1}{s}\int_0^{y/\cot\phi} dx \int_0^\infty dy \exp(-sy) \\ \sum_n e^{-E_n s} &\approx \frac{m}{2\pi\hbar^2 g^2 \cot\phi}\frac{1}{s^3}\end{aligned} \tag{B.15}$$

The inverse Laplace transform of Eq. (B.15) (with respect to s) gives

$$d_{TF}(E) \approx \frac{m}{4\pi\hbar^2 g^2 \cot\phi}E^2 \tag{B.16}$$

Eq. (B.16) gives the so–called 'area' term in the Thomas–Fermi density of states since it was derived by integrating over the area of the wedge.

The next order (in E) approximation to d_{TF} is the so–called perimeter term and results from taking into account not only paths of zero length but those which are very close to a wall and have enough time (as t becomes very small) to bounce off the

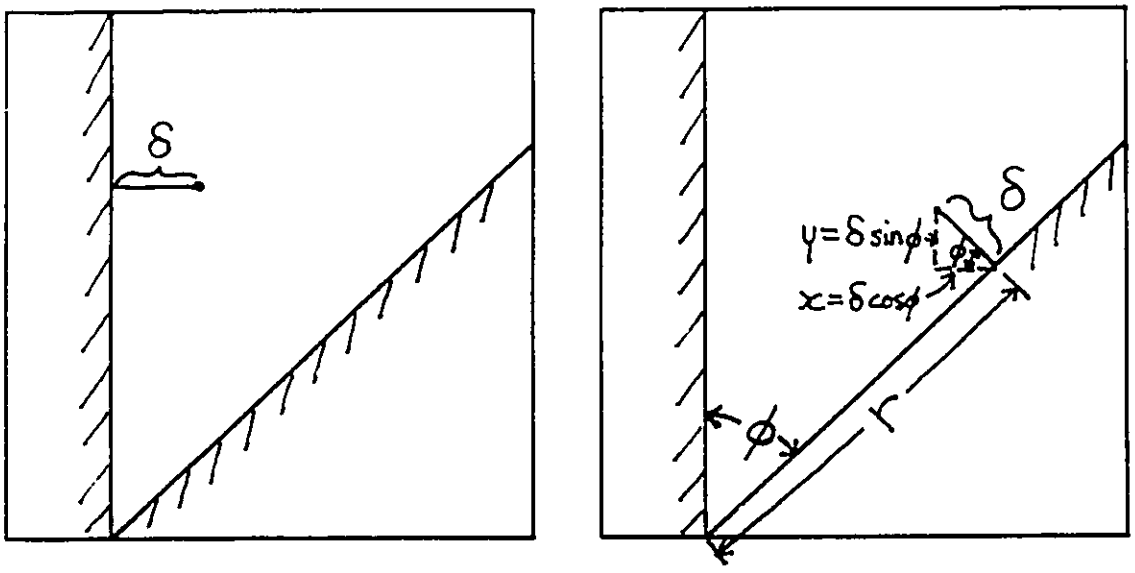

Figure B.1: The geometry of paths which are very close to a wall. In the left figure a path is shown which is close to the vertical wall, and in the right figure a path is shown which is close to the tilted wall. The right figure also shows the geometry of the coordinate system discussed in the text.

wall and come back to their starting position. So, if we want to include corrections due to these paths then we write the propagator as a sum of three paths. In the case of paths near the vertical wall (see Fig. (B.1)) $(x_b - x_a)^2 = (2x)^2$, $(y_b - y_a) = 0$, and $(y_b + y_a) = 2y$. In the case of paths near the tilted wall we introduce a polar coordinate system as shown in Fig (B.1). In this case $(x_b - x_a)^2 = (2\delta\cos\phi)^2$, $(y_b - y_a)^2 = (2\delta\sin\phi)^2$, and $(y_b + y_a) = 2r\cos\phi$. Also, the phase index u for paths which bounce off the boundaries must be 2 to ensure that the propagator goes to zero

along the boundary. This gives the semiclassical propagator as

$$
\begin{aligned}
&G_{SC}(x_b, y_b, x_a, y_a; t)|_{\vec{x}_b \to \vec{x}_a = x} = \\
&-\frac{im}{2\pi\hbar t}\exp\left(\frac{-igt}{\hbar}y - \frac{g^2t^3}{24m}\right) \\
&-\frac{im}{2\pi\hbar t}\exp\left(\frac{i}{\hbar}\left\{-\frac{mgt}{2}2y - \frac{g^2t^3}{24m} + \frac{m}{2t}(2x)^2\right\} - i\pi\right) \\
&-\frac{im}{2\pi\hbar t}\exp\left(\frac{i}{\hbar}\left\{\frac{m(2\delta\sin\phi)^2}{2t} - \frac{mgt2r\cos\phi}{2} + \frac{m(2\delta\cos\phi)^2}{2t}\right\} - i\pi\right).
\end{aligned}
\tag{B.17}
$$

and again, setting $s = it/\hbar$ we get

$$
\begin{aligned}
\sum_n e^{-E_n s} &\approx \frac{m}{2\pi\hbar^2 s}\int_0^{\frac{\pi}{\cot\phi}} dx \int_0^{\infty} dy \exp(-sgy) \\
&\quad -\frac{m}{2\pi\hbar^2 s}\int_0^{\infty} e^{-msgy}dy \int_0^{\infty} e^{-\frac{2m}{\hbar^2 s}x^2}dx \\
&\quad -\frac{m}{2\pi\hbar^2 s}\int_0^{\infty} e^{-\frac{2m}{s\hbar^2}\delta^2}d\delta \int_0^{\infty} e^{-(mgs\cos\phi)r}dr \\
\sum_n e^{-E_n s} &= \frac{m}{2\pi\hbar^2 g^2\cot\phi}\frac{1}{s^3} - \frac{1}{4\hbar g\sqrt{2\pi m}}(1+\sec\phi)\frac{1}{s^{3/2}}
\end{aligned}
\tag{B.18}
$$

Taking the inverse Laplace transform of this equation gives

$$
d_{TF}(E) \approx \frac{m}{4\pi\hbar^2 g^2\cot\phi}E^2 - \frac{1}{4\pi\hbar g}\sqrt{\frac{2}{m}}(1+\sec\phi)E^{1/2} \tag{B.19}
$$

The second term in this equation is the so-called perimeter term, and we see that it has resulted from integrations carried out for orbits very close to the perimeter,

hence the name. Higher order corrections may be carried out, namely the curvature and vertex corrections. Kac shows in his article that the curvature correction for a smooth boundary is $(1/6)\delta(E)$. While we have not re-derived his result for the wedge billiard it seems reasonable that a similar situation would occur in the wedge, which has a smooth boundary all around except at the vertex. Thus, we use Kacs' curvature term to arrive at our final result

$$d_{TF}(E) \approx \frac{m}{4\pi\hbar^2 g^2 \cot\phi} E^2 - \frac{1}{4\pi\hbar g}\sqrt{\frac{2}{m}}(1+\sec\phi)E^{1/2} + \frac{1}{6}\delta(E) \qquad \text{(B.20)}$$

References

Abramowitz M., and Stegun I.A., *Handbook of Mathematical Functions* (Dover, New York, 1965).

Arnold V.I., 1989, *Mathematical Methods of Classical Mechanics* (Springer–Verlag, New York).

Artuso R., Aurell E., Cvitanović P., 1990a, *Nonlinearity* **3**, 325.

Artuso R., Aurell E., Cvitanović P., 1990b, *Nonlinearity* **3**, 361.

Arfken G., 1985, *Mathematical Methods for Physicists*, 3rd edition (Academic Press, Orlando, 1985).

Aurich R. and Steiner F., 1988, *Physica D* **32**, 451.

Aurich R. and Steiner F., 1992, *Phys. Rev. A* **45**, 583.

Aurich R., Matthies C., Sieber M., and Steiner F., 1992, *Phys. Rev. Lett.* **68**, 1629.

Bennettin G., Galgani L., Giorgilli A., Strelcyn J–M., 1980, *Meccanica*, **15**, 21.

Berry M.V. and M. Tabor, 1977, *J. Phys. A* **10**, 371.

Berry M.V. 1981, "Semiclassical Mechanics of Regular and Irregular Motion" in *Chaotic Behaviour of Deterministic Systems, Les Houches Session XXXVI, 1981*, (North Holland, 1983).

Berry M.V. 1985, *Proc. R. Soc. Lond. A* **400**, 229.

Berry M.V. 1987, *Proc. R. Soc. Lond. A* **413**, 183.

Berry M.V. 1988, "Classical Chaos and Quantum Eigenvalues" in *Order and Chaos in Nonlinear Systems*, Edited by S. Lundqvist, N.H. March and M.P. Tosi, (Plenum,

New York, 1988).

Berry M.V. and Keating J.P., 1990, *J. Phys. A.* **23**, 4839.

Biswas D., Azam M., Lawande S.V., 1991, *Phys. Rev. A.* **44**, 4911.

Bolte J., Steil G., and Steiner F., 1992, DESY preprint 92-061.

Bountis T., Helleman R.H.G., 1978, "Periodic solutions of arbitrary period, variational methods" in *AIP Conference Proc. #46, Topics in Nonlinear Dynamics: A Tribute to Sir Edward Bullard*, Edited by S. Jorna, (AIP Press, New York, 1978).

Chernov N.I., 1991, *Physica D* **53**, 233.

Christiansen F. and Cvitanović P., 1992 *Chaos* 2, 61.

Cornfield I.P., Fomin S.V, Sinai Y.G., 1982, *Ergodic Theory* (Springer, Berlin, 1982) pp. 152.

Creagh S.C., Robbins J.M., Littlejohn R.G., 1990, *Phys. Rev. A* **42**, 1907.

Cvitanović P., 1988, *Phys. Rev. Lett.* **61**, 2729

Cvitanović P. and Eckhardt B., 1989, *Phys. Rev. Lett.* **63**, 823.

Cvitanović P., 1991, Physica D **51**, 138.

Delos J.B., 1968, *Adv. Chem. Phys.* **65**, 162.

Desko R.D and Bord D.J., 1983, *Am. J. Phys* **51**, 82-84

Eckhardt B., Aurell E., 1989 *Europhysics Lett.* **9**, 509.

Feynman R.P., 1948, *Rev. Mod. Phys.*, **20**, 367.

Feynman R.P. and Hibbs A.R., 1965, *Quantum Mechanics and Path Integrals* (McGraw-Hill, New York, 1965). See also Feynman R.P. 1948, *Rev. Mod. Phys* **20**, 367

Flügge, 1974, *Practical Quantum Mechanics* (Springer-Verlag, Berlin, 1974) pp. 101-105.

Geldart D.J.W. and Kiang D., 1986, *Am. J. Phys.* 54, 131.

Gibbs R.L., 1975, *Am. J. Phys.* **43**, 25

Goldstein H., 1980, *Classical Mechanics*, 2nd edition (Addison-Wesley, Reading, 1980)

Goodings D.A. and Szeredi T., 1991, *Am. J. Phys* **59**, 924.

Gordon R.G., 1969, *J. Chem. Phys* **51**, 22

Green J.M. and Kim J–S., 1987, *Physica D*, **24**, 213

Gutzwiller, 1967, *J. Math Phys.* **8**, 1979

Gutzwiller M., 1969, *J. Math Phys.* **10**, 1004

Gutzwiller M., 1970, *J. Math Phys.* **11**, 1791

Gutzwiller M., 1971, *J. Math Phys.* **12**, 343

Gutzwiller M., 1979, pg. 316, in *Stochastic Behaviour in Classical and Quantum Hamiltonian Systems* (Springer, Berlin, 1979), G. Casati and J. Ford (editors).

Gutzwiller, 1990 *Chaos in Classical and Quantum Mechanics* (Springer–Verlag, New York, 1990)

Henon M. and Heiles C., 1964, *Astron. J.*, **69**, 73.

Kac M, 1966 *Am. Math. Mon.* **73** 1.

Keating J., 1992a, *Proc. R. Soc. Lond. A* 436, 99.

Keating J., 1992b, *Chaos* **2**, 15.

Kleppner, 1991, *Phys. Today* **44**, 9.

Knudson S.K., Delos J.B., Noid D.W., 1986, *J. Chem. Phys.* **84**, 6886

Knudson S.K. and D.W.Noid, 1989, *J. Chem. Ed.* **66**, 133

Landau L.D. and Lifshitz E.M, 1958, *Quantum Mechanics— Non-Relativistic Theory*

(Pergamon, London, 1958), Sec.22.

Langhoff P.W., 1971, *Am. J. Phys.* **39**, 954.

Lehtihet H.E. and Miller B.N., 1986, *Physica D* **21**, 93.

Lorenz E.N., 1963, *J. Atmos. Sci.*, **20**, 130.

Lorenz E.N., 1984, *Physica D*, **13**, 90.

Mannheim P.D., 1983, *Am. J. Phys* **51**, 328

Marion J.B., 1970, *Classical Dynamics of Particles and Systems, Second Edition* (Academic Press, New York, 1970)

Maslov V.P. and Fedoriuk M.V. 1981 *Semi-classical approximations in Quantum Mechanics* (Reidel, Boston, 1981)

Merzbacher E., 1970 *Quantum Mechanics, Second Edition* (Wiley, New York, 1970)

Noid D.W. and Marcus R.A., 1975 *J. Chem. Phys.* **62**, 2119

Pars L.A. 1965, *A treatise on analytical dynamics, reprinted 1979* (Ox Bow Press, Woodbridge, Conn.)

Rasband S.N., 1991 *Dynamics* (Krieger, Malabar, Florida, 1991)

Schiff L.I., 1968, *Quantum Mechanics, Third Edition* (McGraw–Hill, New York, 1968)

Schulman L.S., 1981, *Techniques and Applications of Path Integration* (Wiley, New York, 1981)

Sieber M. and Steiner F., 1990a, *Phys. Lett. A* **144**, 159.

Sieber M. and Steiner F., 1990b, *Physica D* **44**, 248.

Sieber M. and Steiner F., 1990c, *Phys. Lett. A* **148**, 415.

Sieber M. 1991 *DESY preprint 91-030*

Sieber M. and Steiner F., 1991, *Phys. Rev. Lett.*, **67**, 1941

Sieber M., 1992, *Chaos*, **2**, 35.

Tanner G., Scherer P., Bogomolny E.B., Eckhardt B., and Wintgen D., 1991, *Phys. Rev. Lett.* **67**, 2410.

Tanner G. and Wintgen D., 1992 *Chaos* **2**, 53.

Van Vleck J.H., 1928, *Proc. Nat. Acad. Sci.* **14**, 178

Voros A., 1988, *J. Phys. A.* **21**, 685.

Watson G.N., 1966, *A Treatise on the Theory of Bessel Functions*, 2nd edition (Cambridge University Press, Cambridge, 1966)

Whelan N.D., Goodings D.A., Cannizzo J.K., 1990, *Phys. Rev. A* **42**, 742.

Wintgen D., 1987, *Phys. Rev. Lett.* **58**, 1589.

Wojtkowski M.P., 1990, *Comm. Math. Phys.* **126**, 507.